

**LOW CO₂ METHANOL BY METHANE PYROLYSIS IN CATALYTIC
LIQUID METAL BUBBLE REACTOR**

BY

BRAEDEN ROBERTS

THESIS

Submitted in partial fulfillment of the requirements
for the degree of Master of Science in Chemical Engineering
in the Faculty of Graduate Studies of
Lakehead University

September 2022

Thunder Bay, Ontario, Canada

Advisors:

Dr. Lionel Catalan, PhD, PEng

Dr. Ebrahim Rezaei, PhD, PEng

Abstract

Methanol production based on methane pyrolysis presents an opportunity for CO₂ utilization and lower CO₂ emissions than traditional methanol production processes that are based on methane reforming. This research employs a coupled hydrodynamic and kinetic pyrolysis reactor model in the design and simulation of a methanol plant that produces 2000 t/d of grade A methanol by direct hydrogenation of CO₂. The methane pyrolysis occurs in a catalytic liquid metal bubble reactor where natural gas is injected at the bottom of the liquid metal bath and forms bubbles that rise through the molten metal. Methane pyrolysis occurs non catalytically inside the bubbles and catalytically at the gas-liquid interface. Solid carbon separates from the molten metal and forms a layer on top of the molten salt cap that is on top of the molten metal and is used to limit molten metal losses. The solid carbon can be continuously removed via skimming. A fired heater and heat recovery section are used to satisfy the energy demands of the process. Because the advantage of methanol synthesis based on methane pyrolysis lies in its low CO₂ emissions, a comprehensive CO₂ accounting is performed which accounts for the plant direct CO₂ emissions as well as the indirect CO₂ emissions associated with the natural gas supply chain and the capture of the process CO₂ feed. The calculated CO₂ emissions are compared to literature values for other methanol production processes based on methane reforming or methane pyrolysis. The plant economics are assessed to determine the levelized cost of carbon and evaluate the economic viability of the novel process. The proposed process has cradle-to-gate and cradle-to-grave emissions of 0.074 and 1.448 t CO_{2-eq}/t MeOH, respectively, when a CH₄ conversion of 80% in the pyrolysis reactor is used and when the indirect CO₂ emissions are calculated at their base values. The corresponding volume of Cu_{0.45}Bi_{0.55} catalytic liquid metal is 98.0 m³. These operating conditions result in a levelized cost of carbon of \$270/t. It was found that the levelized cost of carbon is most sensitive to the fixed capital investment of the plant and the purchase price of CO₂. This work shows that the source of CO₂ is a critical variable for this process, as it affects both the purchase price and the emissions associated with its capture.

ACKNOWLEDGMENTS

Thank you to my supervisors Dr. Lionel Catalan and Dr. Ebrahim Rezaei for guiding me through the process and taking the time to review my progress and meet with me every week. Without your tireless efforts this project would not have been possible.

Thank you to the committee members Dr. Francisco Ramos-Pallares and Dr. Basel Ismail for taking the time to review my work, and for your helpful comments and suggestions.

Table of Contents

Abstract.....	ii
ACKNOWLEDGMENTS.....	iii
Table of Contents.....	iv
List of Tables.....	vii
List of Figures.....	viii
Chapter 1. Introduction.....	1
1.1 Methanol Synthesis.....	1
1.1.1 Renewable Methanol – Biomass Gasification & Electrolysis.....	2
1.1.2 Non-Renewable Methanol – Natural Gas Reforming & Coal Gasification.....	3
1.1.3 Non-Renewable Methanol – Methane Pyrolysis.....	5
1.2 Methane Decomposition.....	6
1.2.1 Reactor Configuration.....	6
1.2.2 Noncatalytic Liquid Metal Bath Reactors (LMBRs).....	8
1.2.3 Catalytic Liquid Metal Bath Reactors (CLMBRs).....	10
1.2.4 Molten Salts.....	11
1.3. Solid Carbon.....	12
1.3.1 Raman Spectroscopy.....	12
1.3.2 Carbon Product from Molten Media Reactors.....	14
1.3.3 Carbon Purity & Cleaning.....	24
1.4. Carbon Market.....	26
1.4.1 Graphitic Amorphous Carbon (Carbon Black).....	26
1.4.2 Graphite.....	27
1.4.3 Multi Walled Carbon Nanotubes.....	28
1.5. CO ₂ Accounting.....	29
1.5.1 Indirect Emissions – Natural Gas Supply Chain.....	30
1.5.2 Indirect Emissions – CO ₂ Capture.....	31
1.5.3 Indirect Emissions – Electricity Import.....	32
1.6 Knowledge Gaps & Objectives.....	32
Chapter 2. Overall Process Description.....	35

2.1 Block Flow Diagram	35
2.2 Process Flow Diagram	36
Chapter 3. Process Modelling and Simulation	51
3.1 Pyrolysis Reactor (PR).....	51
3.2 Methanol Synthesis Reactor (MSR).....	58
3.2.1 Kinetics & Model Validation	58
3.2.2 Modelling and Operating Conditions Selection.....	59
3.2.3 Heat Transfer	62
3.2.4 Shell Diameter	69
3.3 Fireside of the Fired Heater	70
3.4 Plate and Shell-and-Tube Heat Exchangers	71
3.5 Flash Tanks and Distillation Columns	73
3.6 Pressure Swing Adsorber	75
3.7 Compressors, Blowers, Turbines, and Expanders	76
3.8 Utilities	77
Chapter 4. Process Performance	80
4.1 Energy Conversion from Natural Gas to Methanol.....	80
4.2 CO ₂ accounting	85
4.3 CO ₂ Sensitivity Analysis	93
Chapter 5. Economics	97
5.1 Estimation of Capital Costs.....	97
5.1.1 Copper-Bismuth Alloy.....	99
5.1.2 Sodium Bromide Salt	100
5.1.3 Pressure Swing Adsorption (PSA)	100
5.1.4 Methanol Synthesis Reactor (MSR) and Catalyst	101
5.1.5 Plate Heat Exchanger for Solid Carbon.....	101
5.1.6 Total Module Cost	102
5.2 Estimation of Manufacturing Costs.....	107
5.2.1 Natural Gas	108
5.2.2 Carbon Dioxide	108
5.2.3 Methanol	108

5.2.4 Electricity	108
5.2.5 Makeup NaBr Salt and Replacement of Methanol Synthesis Catalyst.....	108
5.2.6 Cost of Operating Labour	109
5.2.7 Cost of Utilities	110
5.2.8 Cost of Waste Treatment	111
5.3 Cash Flow Analysis.....	113
5.4 Sensitivity Analysis	115
Chapter 6. Conclusions	118
References	121

List of Tables

Table 1. Stream summary	43
Table 2. Utilities summary	48
Table 3. Design parameters of the pyrolysis reactor for a 2000 t/d methanol plant.....	55
Table 4. Distillation tower T-102 sizing information.	75
Table 5. Compressor efficiencies.	76
Table 6. Turbine efficiencies.	77
Table 7. Breakdown of producers and consumers of electricity and steam.	78
Table 8. Breakdown of producers and consumers of boiler feed water and cooling water.	79
Table 9. Comparison of energy conversion to methanol for different methane pyrolysis and methane reforming processes.....	82
Table 10. Comparison of CO ₂ accounting for different methane decomposition and methane reforming processes.	90
Table 11. Capacity, materials of construction, and cost information for plant equipment.	104
Table 12. Breakdown of the grassroots cost of the CP-LMBR plant by equipment type.	107
Table 13. Data for estimation of manufacturing costs.	107
Table 14. Number of non-particulate equipment.	110
Table 15. Material flows and annual costs.	112
Table 16. Estimation of annual manufacturing cost by Equation (46).	112
Table 17. Cash flow analysis assumptions.	113

List of Figures

Figure 1. Methanol production Routes.....	1
Figure 2. Methanol synthesis pathway by methane pyrolysis vs. steam methane reforming.....	6
Figure 3. Schematic of Abánades et al., (2011) experimental setup.....	7
Figure 4. Simplified schematic of liquid metal bath reactor for methane pyrolysis.	9
Figure 5. Raman spectra of carbon-based materials excited at 633 nm (Bokobza et al., 2015). Graphite grades 3775, 4827 & 4124, multiwalled carbon nanotubes (MWCNTs), graphene oxide (GO) and carbon black (CB).	13
Figure 6. SEM micrographs of carbon obtained from 0.1 m (a) 100 wt% Sn, (b) 95 wt% Sn – 5 wt% Cu, (c) 95 wt% Sn – 5 wt% Ni & (d) 70 wt% Sn – 30 wt% Cu (Zaghloul et al., 2021).	15
Figure 7. SEM micrographs of carbon obtained from 0.18 m KCl bubble column at different temperatures: (a) 950 °C, (b) 1000 °C, (c) 1050 °C, (d) 1100 °C & (e) 1150 °C. All carbons have been washed in 70 °C water for two hours with constant stirring. Scale bars in all images are 50 µm (C. Palmer et al., 2021).	17
Figure 8. SEM micrographs of carbon samples obtained in 1000 °C NiBi (350 mm) single phase bubble column reactor at different magnifications. A & B indicate the presence of metal particles (Rahimi et al., 2019).....	18
Figure 9. SEM micrographs of carbon samples obtained from 1000 °C (a) & (b) NiBi/KBr (110 mm/240 mm), (c) & (d) NiBi/KBr (240 mm/110 mm) & (e) & (f) NiBi/NaBr (110 mm/240 mm) two phase bubble column reactors (Rahimi et al., 2019).	19
Figure 10. Raman spectra of carbon excited at 633 nm and produced in (a) NiBi, (b) NiBi/KBr (240 mm/110 mm), and (c) NiBi/KBr (110 mm/240 mm) from (Rahimi et al., 2019). 20	
Figure 11. Process block flow diagram.	36
Figure 12. Process flow diagram of the pyrolysis section; E: heat exchanger EX: gas expander, K: compressor, PU: PSA unit, R: reactor.	40
Figure 13. Process flow diagram of the MSR section; E: heat exchanger, R: reactor, T: tower, and V: vessel.	41

Figure 14. Process flow diagram of the fired heater and heat recovery section; B: blower, E: heat exchanger, P: pump, R: reactor, TU: steam turbine.	42
Figure 15. Pyrolysis reactor methane conversion and gas hold up profiles along the length of a single PR tube. Dimensions and operating conditions are those found in Table 1.	56
Figure 16. 100,000-h creep rupture stress versus temperature for Manaurite XM.	57
Figure 17. Experimental and Aspen Hysys™ simulated mole flows along MSR length using the Vanden Bussche & Froment (1996) kinetic model.	58
Figure 18. MSR reactor temperature profile simulated in Aspen Hysys™ using the Vanden Bussche and Froment (1996) kinetic model.	59
Figure 19. Methanol synthesis reactor inlet temperature and pressure selection with constant reactor volume (300 m ³), inlet flow rate and feed composition under isothermal and isobaric conditions.	61
Figure 20. Methanol synthesis reactor volume selection under isothermal and isobaric conditions with constant reactor inlet flowrate, composition, temperature (255 °C) and pressure (8000 kPa).	62
Figure 21. Temperature profiles of the process fluid (tubes) and the saturated steam (shell)...	67
Figure 22. Molar flow profiles along the tubes of the MSR.....	68
Figure 23. Schematic of Solex plate heat exchanger for cooling solid particles (<i>Cooling Heat Exchanger - Cool Bulk Solids Without Air Solex - Solex, n.d.</i>).....	72
Figure 24. Effect of pyrolysis reactor methane conversion on cradle-to-gate emissions, natural gas consumption, PSA H ₂ recovery and fuel H ₂ mol%.	85
Figure 25. Effect of methane conversion in the PR on TU-100 shaft power, exported electricity, molten metal alloy and inlet and outlet pressures.....	89
Figure 26. Effect of the CO ₂ emissions factors for (a) natural gas supply, (b) CO ₂ supply, and (c) electricity supply on the cradle-to-gate CO ₂ emissions of several natural gas pyrolysis and reforming processes. Data for SMR and GHR + ATR assume maximum electricity imports to emphasize the effect of <i>Felect. – supply</i> on the emissions of these processes.....	96

Figure 27. Discounted and non-discounted cash flow diagram when the cost of carbon is set to its levelized value of \$0.270/kg. 115

Figure 28. Correlation between yearly average methanol and industrial natural gas prices between 2012 and 2021. Historical natural gas prices are from EIA (U.S. Energy Information Administration) (EIA (U.S. Energy Information Administration), n.d.-c). Historical methanol prices are from Methanex (Methanex, n.d.). Normalized yearly average prices in the figure insert are calculated as ratios of yearly average prices to the overall average over the 2012-2021 period..... 116

Figure 29. Sensitivity of the levelized cost of carbon to variations in economic parameters.... 117

Chapter 1. Introduction & Literature Review

1.1 Methanol Synthesis

Figure 1 is a flow sheet taken from the International Renewable Energy Agency (IRENA), (2021) that has been adapted to include the process developed in this research (shown with red arrows and box outlines). The figure summarizes the various pathways by which methanol is produced, and their respective carbon intensities.

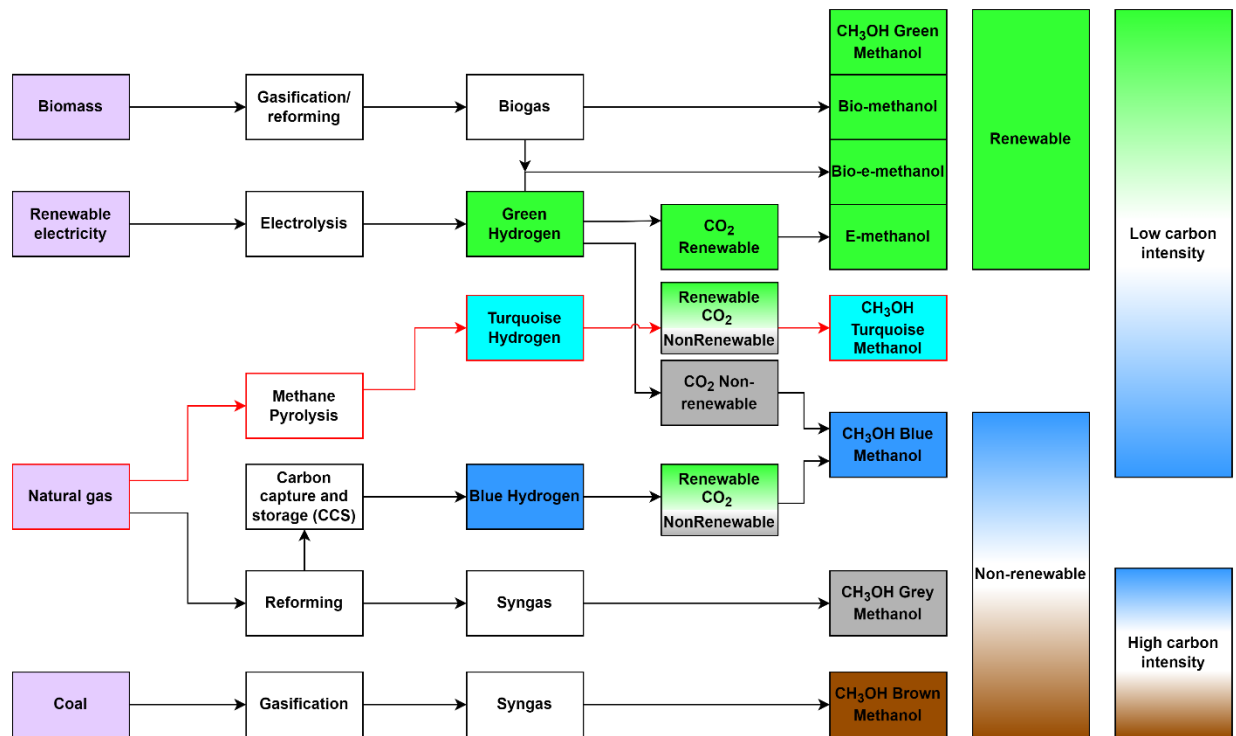


Figure 1. Methanol production Routes

In Figure 1, blue hydrogen is defined as hydrogen that is produced from a fossil fuel feedstock, such as natural gas or coal, in a process that incorporates carbon capture and storage. Green hydrogen, on the other hand, is hydrogen that is produced from renewable fuel/energy sources such as biogas, biomethane or biomass, examples of which include forestry and agricultural waste and by-products, biogas, sewage, municipal solid waste and black liquor from the pulp and paper industry. An additional renewable fuel/energy source is renewable electricity, which is electricity produced from solar, wind, hydro, or geothermal sources. Turquoise hydrogen is

the type of hydrogen that is produced by natural gas pyrolysis, and its name is selected based on the associated CO₂ emissions, which are presented in this study and found to be between those from green and blue hydrogen production. Renewable CO₂ is defined as CO₂ that is captured directly from the atmosphere or from a biogenic source, an example of which is the off gas of the combustion of biomass from distilleries, fermentation units, municipal solids waste or biogas to produce electricity. Non-renewable CO₂ is defined as CO₂ that is produced from the burning of fossil fuels. Green, blue, grey & brown methanol all refer to the carbon intensity of the process, which corresponds to the amount of CO₂ emitted in the production of the respective methanol, with green being the least amount of CO₂ and brown being the most.

1.1.1 Renewable Methanol – Biomass Gasification & Electrolysis

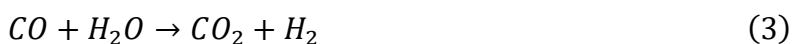
Figure 1 also shows three types of green methanol: bio-methanol, bio-e-methanol, and e-methanol. Bio-methanol is methanol that is produced using biomass, biogas or biomethane as a feedstock. The biomass used in this process can be any type of forestry and agricultural waste and by-products, biogas, sewage, municipal solid waste or black liquor from the pulp and paper industry. The gasification or reforming of this biomass produces a gaseous mixture of CO, CO₂ and H₂ commonly referred to as synthesis gas or syngas. The syngas is then converted into bio-methanol by Equation (1):



E-methanol is methanol produced from a combination of renewable electricity sources such as solar, hydro, geothermal or biomass, and CO₂ captured from renewable sources, such as direct air capture or from the off streams of renewable electricity production by biomass, biogas or biomethane combustion. This renewable electricity is used to electrochemically split water into hydrogen and oxygen in a process known as water electrolysis and produces green hydrogen so long as the electricity source is a renewable one. The green hydrogen is then reacted with green CO₂ to produce E-methanol by the direct hydrogenation of CO₂ using Equation (2).



The product is bio-e-methanol if the green hydrogen produced by water electrolysis is injected into the syngas stream produced in the bio-methanol pathway. This is done to adjust the H₂/CO ratio so that a value of 2 is obtained based on the stoichiometry of methanol synthesis from CO & H₂ (Equation 1). This step eliminates the need for the water gas shift reactor that otherwise would be required to achieve this ratio (Equation 3).



While green methanol production is an attractive option from an environmental standpoint, the use of biomass and renewable electricity for methanol production currently accounts for <1% of all methanol feed stocks used (International Renewable Energy Agency (IRENA), 2021).

1.1.2 Non-Renewable Methanol – Natural Gas Reforming & Coal Gasification

Non-renewable methanol involves the use of either hydrogen or CO₂ that is produced from non-renewable sources, or both. Coal and natural gas are the most prevalent feedstocks for methanol production, accounting for ~35% and ~65% of feedstocks used, respectively (International Renewable Energy Agency (IRENA), 2021).

Methanol synthesis based on coal gasification produces methanol with the highest carbon intensity, that is, methanol production that is associated with the most CO₂ emissions. In order to produce syngas from coal, a gasification step is required that involves 3 main reactions: the partial oxidation of coal (Equation 4) and high temperature (800-1800 °C) steam treatment (Equation 5) which includes the water gas shift reaction (Equation 3) (Bell & Towler, 2010)



The produced syngas requires several pretreatment, conditioning, and adjustment stages to remove impurities and achieve the appropriate hydrogen/carbon (H/C) ratio. This is because coal has a low H/C ratio, resulting in syngas containing a lot of CO & CO₂ but not enough hydrogen. As a result, some of the produced CO₂ must be separated from the mixture and simply vented to the atmosphere. The carbon intensity of coal gasification could therefore be reduced by implementing a carbon capture system. In addition, the syngas pretreatment steps are energy intensive, resulting in additional CO₂ emissions. After appropriate treatment, methanol is produced by Equation (1).

When natural gas is used as a feed stock, syngas is produced by some type of reforming, the most common type being steam methane reforming (SMR) which involves the water gas shift and steam reforming reactions (Equations 3 & 6):



The syngas mixture of H₂, CO & CO₂ is then used to produce methanol using Equation (1).

Compared to coal, natural gas has a higher H/C ratio, and the produced syngas has fewer impurities. These factors result in a reduction in CO₂ emissions of 2.1-3.3 kgCO₂-eq/kg MeOH (Kajaste et al., 2018) when choosing methanol synthesis based on natural gas reforming over methanol synthesis based on coal gasification.

As evident from Equations (1), (3) & (6), the typical reforming based methanol synthesis process uses non-renewable hydrogen, resulting in the production of grey methanol. The addition of CCS is one solution to minimizing the CO₂ emissions of a methanol production process based on

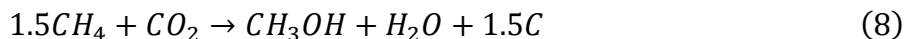
reforming by recycling captured CO₂ from the process flue gas to ultimately produce blue methanol by Equation (2), as shown in Figure 1.

1.1.3 Non-Renewable Methanol – Methane Pyrolysis

The Carnol process is a methanol production pathway that produces methanol via the direct hydrogenation of CO₂ with hydrogen that is produced from the thermal decomposition of methane, also known as methane pyrolysis. This methanol production process is the one that the present research focuses on and is highlighted in Figure 1 by red outlines and arrows. Equations (2), (7) & (8) summarize the Carnol process.



By adding Equations (2) & (7) the overall Carnol process stoichiometry becomes Equation (8):



The overall Carnol process stoichiometry (Equation 8) shows that 1 mole of CO₂ is consumed per mole of methanol produced with no greenhouse gas (GHG) by-products. In fact, the by-product of the Carnol process is solid carbon, which can be sold as a product. As such, the Carnol process presents the opportunity to design a turquoise methanol synthesis process that is NET neutral or a NET consumer of CO₂.

Figure 2 emphasizes the advantage that the Carnol process has over other non-renewable methanol synthesis processes, specifically steam methane reforming. This advantage is that the Carnol process uses CO₂ as a raw material and does not produce any CO₂ in its hydrogen production stage. A coal gasification or natural gas reforming-based process on the other hand does not use CO₂ as a raw material, and rather uses the CO that is produced in the gasification/reforming stage of the process, or requires the addition of a CCS unit to utilize/minimize the CO₂ emissions. This advantage presents an opportunity with the Carnol

process for CO₂ utilization and CO₂ emissions minimization with turquoise methanol production.

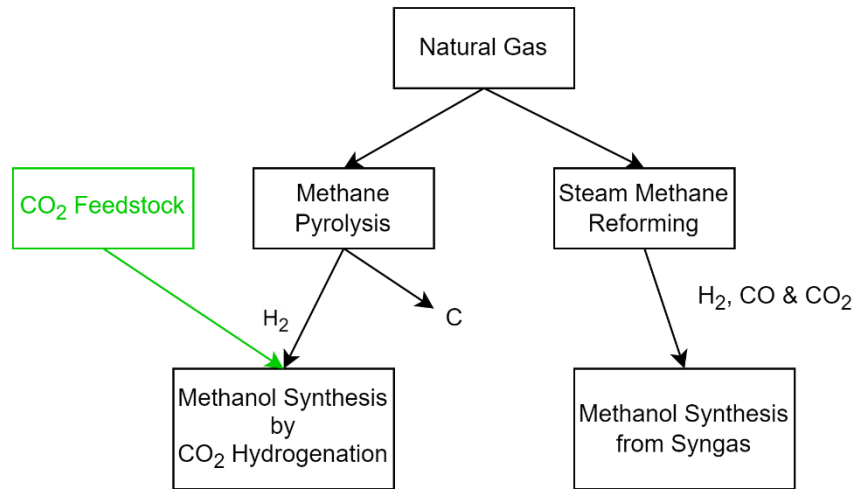


Figure 2. Methanol synthesis pathway by methane pyrolysis vs. steam methane reforming.

1.2 Methane Pyrolysis

1.2.1 Reactor Configuration

Methane pyrolysis is a unique characteristic of the Carnol process that may be carried out in various reactor configurations. Abánades et al. (2011) investigated direct thermal methane cracking in a double tube reactor where the inner tube was porous graphite. Sweeping gas (Argon, Helium or Hydrogen) was fed to the outer tube and transferred to the methane stream, which flowed through the inner tube, through the pores of the inner tube wall. This gas flow was intended to prevent carbon plug formation in the inner tube. A schematic of their experimental setup is shown in Figure 3.

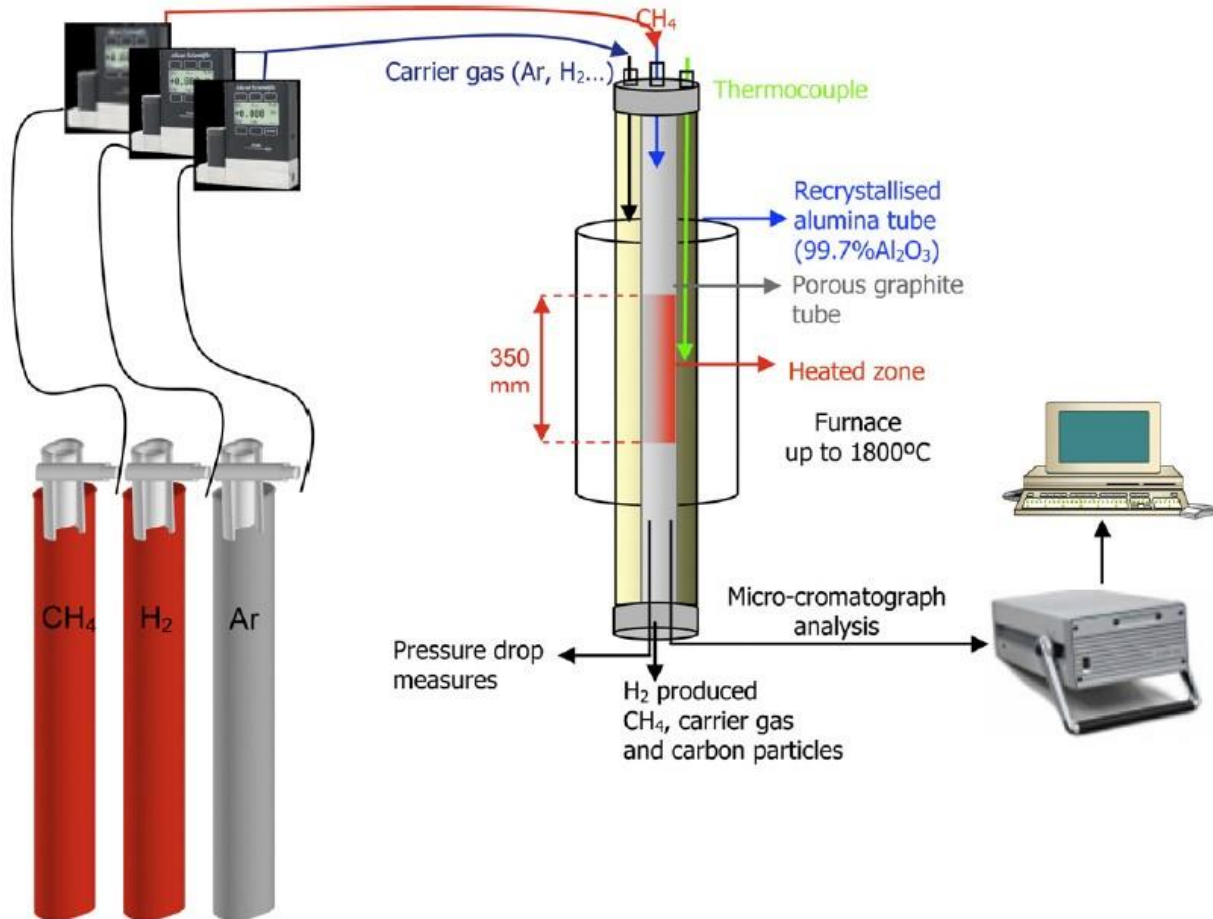


Figure 3. Schematic of Abánades et al., (2011) experimental setup.

Their results showed that regardless of tube porosity, a carbon plug would form in the inner tube, blocking the flow of gas. An alternative to tubular reactors is the use of catalytic fluidized beds. The downfall of this configuration is that solid carbon deposition often deactivates the catalyst and subsequent catalyst regeneration would result in CO₂ emissions (Muradov et al., 2005). This defeats the purpose of a process designed for low CO₂ emissions.

Plasma reactions are another method of decomposing natural gas into hydrogen and carbon. Monolith™ currently has a commercial plant in New England that utilizes 100% renewable electricity and produces 0.3 tonne of hydrogen per tonne of carbon black by thermal plasma methane pyrolysis (Monolith, n.d.; Monolith Carbon Black, n.d.). Plasma processes are typically split into two categories: thermal plasmas and non-equilibrium plasmas or cold plasmas. Thermal plasmas include direct current, arco torch, alternating current, radio frequency

inductively coupled torch, and high frequency capacitive torch while non-equilibrium plasmas include microwave, corona discharge plasma, dielectric barrier discharge plasma, atmospheric pressure glow discharge plasma and gliding arc discharge (Dagle et al., 2017b). Thermal plasmas require higher operating temperatures, between 1500-3500 °C for methane pyrolysis (Schwob et al., 2000), whereas cold plasmas work in the range of 850-900 °C (Muradov et al., 2009).

The plasma process possesses the advantage of producing high purity carbon and different grades of carbon depending on the process temperature (Fulcheri et al., 2002) as well as the opportunity for high yields of H₂ & carbon (100% carbon yield) (Dagle et al., 2017b).

Additionally, plasma reactors are an order of magnitude smaller than reactors used in steam methane reforming processes (Longmier et al., 2012; Vinokurov et al., 2005). However, these advantages are accompanied by an energy requirement per kg H₂ produced that is 37 times higher than that of steam methane reforming (Longmier et al., 2012) and that must be satisfied by electricity, which in many cases limits the maximum CH₄ conversion. There is also evidence that a relatively high fraction of methyl radical is produced during the methane pyrolysis and enables the formation of stable hydrocarbons and polymeric species, which reduces the solid carbon yield (Kim et al., 2005).

1.2.2 Noncatalytic Liquid Metal Bath Reactors (LMBRs)

A configuration that eliminates the complications of carbon deposition and catalyst deactivation is the liquid metal bath reactor (LMBR), first proposed by Steinberg, (1996). In this configuration, methane is sparged through the bottom of the reactor, forming bubbles as it rises through the liquid metal. The noncatalytic pyrolysis occurs inside the bubbles and, if a catalytic molten metal is used, the catalytic pyrolysis occurs at the interface between the bubble and the melt. The solid carbon forms a layer on top of the liquid metal based on the density difference between the two (2.11 g/cm³ for graphite at 1100 °C (Senchenko & Belikov, 2017) & 8.81 g/cm³ for molten 45 mol% - Cu 55 mol% - Bi (Catalan & Rezaei, 2022)). Solid carbon deposition on reactor walls was found to be thin (15 µm after 15 days of continuous operation (Geißler et al., 2016)) and the rate of deposition decreased with time (Upham et al.,

2017). A simplified schematic of a liquid metal bath reactor for methane pyrolysis is shown in Figure 4.

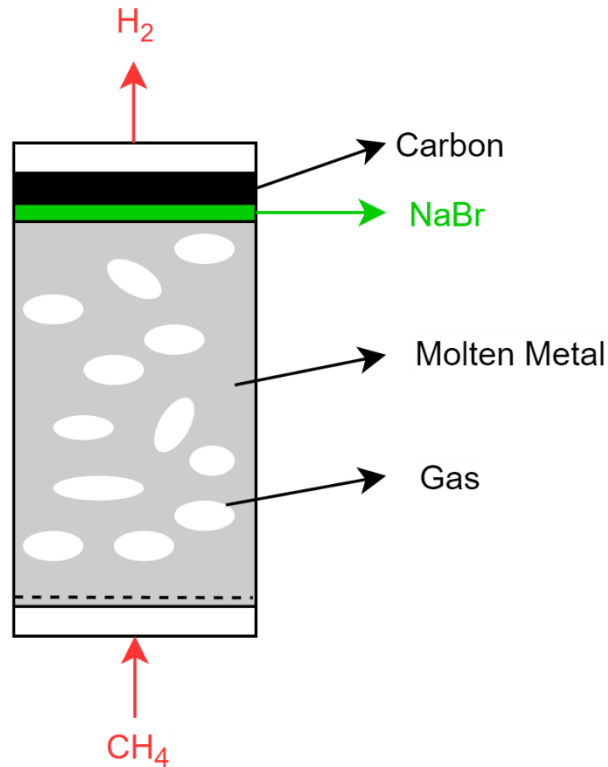


Figure 4. Simplified schematic of liquid metal bath reactor for methane pyrolysis.

Initial experimental investigation into LMBRs for methane pyrolysis was performed using noncatalytic metals such as molten tin. An issue with the use of a noncatalytic metal for methane pyrolysis is the requirement of impractically large reactor volumes. For example, Catalan & Rezaei, (2020) calculated the required reactor volumes for 200 kt/a of hydrogen production in noncatalytic tin at different temperatures and methane conversions, finding a liquid metal volume of 475 m³ at 1050 °C and a methane conversion of only 65%. At higher methane conversions the liquid metal volume would become even greater.

1.2.3 Catalytic Liquid Metal Bath Reactors (CLMBRs)

An alternative to noncatalytic LMBRs is the use of catalytic liquid metal bath reactors (CLMBR). Upham et al., (2017) experimentally investigated methane pyrolysis in 27 mol% - Ni 73 mol% - Bi catalytic molten metal and subsequently developed a model relating the methane conversion to the reactor bubble surface area. In their model, they considered only the forward catalyzed reaction and assumed a constant bubble diameter throughout the reactor length. In order to fit the model to their experimental data, they used the initial bubble diameter as a tuning parameter. Farmer et al., (2019) expanded on the model of Upham et al., (2017) by including both the forward and reverse catalyzed and uncatalyzed reaction rates, as well as the effect of pressure and methane conversion on the bubble diameter along the length of the reactor. The authors validated their model against the experimental data of Upham et al., (2017) by once again tuning the initial bubble diameter. While in both cases the models accurately represented the experimental data, they were not predictive models and required the tuning of the initial bubble diameter.

Catalan & Rezaei, (2022) improved further on the work of Upham et al., (2017) & Farmer et al., (2019) by developing a combined kinetic & hydrodynamic model that was able to accurately predict the experimental data of Upham et al., (2017) based on the superficial gas velocity, column diameter & physical properties of the melt. Additionally in their research, they investigated the proposition of Palmer et al., (2019) who suggested the use of 45 mol% - Cu 55 mol% - Bi as a catalytic molten metal because it exhibited more catalytic activity for methane pyrolysis than 27 mol% - Ni 73 mol% - Bi. The results showed that under the same operating conditions and for the same hydrogen production capacity, the use of 45 mol% - Cu 55 mol% - Bi molten metal resulted in smaller reactor volumes, which is beneficial from a practical and economical perspective. The study also displayed the advantage and effectiveness of a catalytic metal over a noncatalytic metal for reducing reactor volumes. At the same reactor height (1.15 m), diameter (0.03 m), operating conditions (1040 °C, 200 kPa), and feed flow rate (10 cm³ (std).min⁻¹ of 80 mol% CH₄ and 20 mol% Ar), a CLMBR using 27 mol% - Ni 73 mol% - Bi achieves a CH₄ conversion of 83%, while an LMBR filled with noncatalytic tin has a CH₄ conversion of only 35%.

One complication when it comes to the use of LMBRs is providing the necessary heat for the endothermic methane pyrolysis reaction. Different methods of providing heat to the reactor have been investigated, such as the study by Von Wald et al., (2020) where the LMBR is heated to 1100 °C using Si-C resistive heating elements. The study presented by Narine et al., (2021) assumes the pyrolysis reactor (PR) operates in a fluidized bed configuration at 1500 °C with natural gas combustion providing the necessary heat. The use of molten salts as a heat transfer medium has also been suggested by Parkinson et al., (2018) where the molten salt loop includes a carbon removal drum where the carbon is separated from the molten salt based on settling velocity differences, a molten salt pump, and a fired heater required to heat the molten salt to the desired temperature. The salt is then returned to the PR and sparged through the liquid metal where heat is transferred by direct contact. In the present study, it is assumed that the PR is a multi-tubular reactor inside a fired heater, as was proposed by Catalan & Rezaei, (2022), and that the combustion of fuel provides heat to the liquid metal to drive the pyrolysis reaction.

1.2.4 Molten Salts

While molten salts have been proposed as a heat transfer medium (Parkinson et al., 2018) and as a low cost molten media for the pyrolysis of natural gas (C. Palmer et al., 2021; Parkinson et al., 2021), they have also been investigated for use as a layer on top of a catalytic molten metal that aids in solid carbon separation and in minimizing molten metal losses, as shown in Figure 4 (Rahimi et al., 2019). The study showed that NaBr molten salt forms a layer between the molten alloy and the solid carbon (similarly shown by both Palmer et al., (2021) & Parkinson et al., (2021)) due to the fact that it is unlikely to wet the carbon surface. This minimizes the loss of liquid metal due to evaporation and contamination in the solid carbon product.

1.3. Solid Carbon By-Product

The solid carbon product from the PR in a methanol production process based on methane pyrolysis is a key economic variable, so the quality at which it is produced, and the subsequent costs and steps required to purify and upgrade the carbon are of great importance.

1.3.1 Raman Spectroscopy

One of the most common experimental techniques used to characterize solid carbon is Raman spectroscopy. This process involves the excitation of the sample from a ground electronic state subsequently resulting in the spontaneous emission of a photon, so that the sample may “relax” back down to a lower energy electronic state. The emission photon energy corresponds to the vibrational energy involved in the process and is usually expressed in inverse wavelength with the units of cm^{-1} . The spectra are plots of the intensity versus wavelength, and the location of the peaks provide information on the type of carbon. Raman spectroscopy and the ratio of the intensities of the D & G bands are used to classify amorphous carbon as either graphitic amorphous carbon (g-C), diamond-like amorphous carbon (d-C) or hydrogenated amorphous carbon (a-C:H) (Dennison et al., 1996).

First order Raman spectroscopy yields a high intensity peak at 1580 cm^{-1} (Tamor & Vassell, 1994) and represents the graphitic carbon present in the sample. This peak is known as the “G” band. The “D” band, also known as the “defect” or “disordered” band, refers to a high intensity peak at 1360 cm^{-1} and is attributed to disorder induced Raman activity of zone-boundary phonons (Tuinstra & Koenig, 1970) and represents structural defects in the network relating to the presence of amorphous carbon structures (Pimenta et al., 2007). The ratio of the intensity of the D band to that of the G band is used to characterize the degree of graphitization for a solid carbon sample, where a ratio of 0 would indicate ideal graphite with no defects. d-C exhibits an additional peak at 1332 cm^{-1} (Robertson, 1986) while the presence of hydrogen shows a broad tail centered around 600 cm^{-1} (Dennison et al., 1996). Second order Raman spectroscopy shows a peak at 2650 cm^{-1} , termed the 2D or G’ band, and is a signature of graphitic sp^2 materials (Rahimi et al., 2019) that indicates the presence of graphene (Parkinson

et al., 2021). If the 2D band is split into a doublet, this means that stacking layers of graphene are present (Bokobza et al., 2015). Figure 5 shows the Raman spectra of some carbon based materials analyzed by Bokobza et al., (2015). The presence of the 2D doublet is observed in the Raman spectra of graphite 3775.

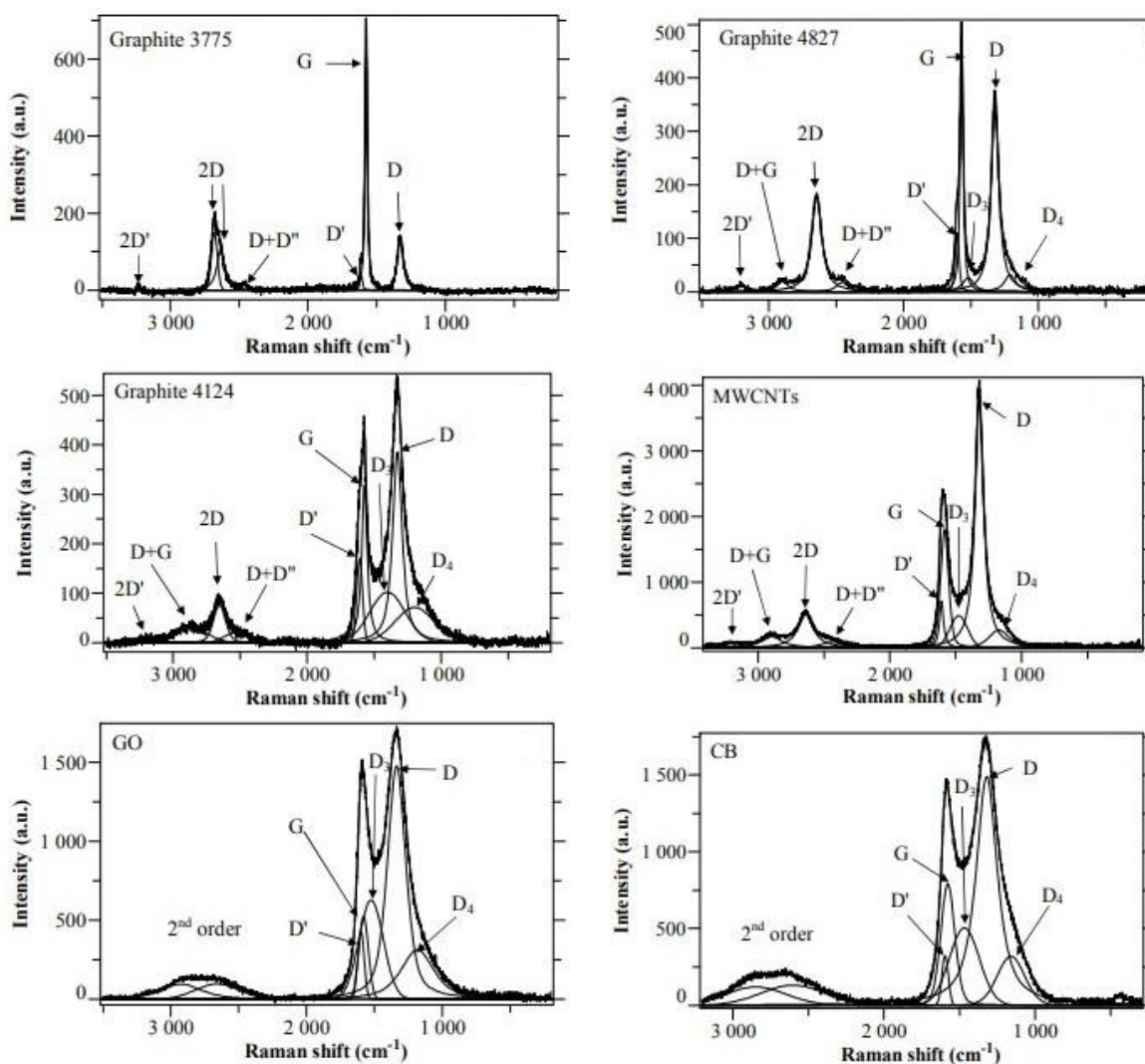


Figure 5. Raman spectra of carbon-based materials excited at 633 nm (Bokobza et al., 2015). Graphite grades 3775, 4827 & 4124, multiwalled carbon nanotubes (MWCNTs), graphene oxide (GO) and carbon black (CB).

The ASTM grade of carbon black, which is a mixture of graphitic and amorphous carbon and whose Raman spectra is shown in Figure 5 (CB), is specified based on the cetyltrimethylammonium bromide (CTAB) surface area, which measures the specific surface area of the carbon black independent of the internal area. The higher the grade number, the smaller the CTAB surface area, meaning the larger the particle size (Ex. N990 grade carbon black has a larger particle size than N220 grade carbon black). (*Carbon Black - Himadri*, n.d.) provide a summary of the different applications for the various ASTM grades of carbon black in tire production.

1.3.2 Carbon Product from Molten Media Reactors

In their research, Upham et al., (2017) assessed the quality of the carbon produced from methane pyrolysis in a 1.1 m length liquid metal bath of 27 mol% - Ni 73 mol% - Bi at 1000 °C using Raman spectroscopy as well as X-ray photoelectron spectroscopy. Raman spectroscopy of the recovered sample indicated that the graphitic amorphous carbon was highly graphitic, as the ratio of D/G bands was 0.594. The X-ray photoelectron spectroscopy of the sample exhibited a sharp peak at 285.4 eV, corresponding to C-C sp² bonds which also confirmed the sample was primarily graphitic.

Zaghloul et al., (2021) analyzed the morphology of solid carbon produced from methane pyrolysis in a 0.1 m long liquid metal bath of different tin alloys at temperatures between 950-1050 °C using scanning electron microscopy (SEM) with energy-dispersive X-ray spectroscopy, X-ray diffraction, and Raman spectroscopy. SEM analysis revealed the carbon structure consisted of stacked grains in most of the samples, however the carbon produced from a catalytic molten metal alloy of 70 wt% - Sn 30 wt% - Cu revealed tubular structures that were filled with the molten metal. Figure 6 shows the SEM micrographs of the carbon produced in the various liquid metals used in their study. The Raman spectroscopy showed that the carbon samples were more amorphous than that of Upham et al. (2017), having D/G band ratios between 1.03-1.26 depending on the molten media. This difference may be attributed to the difference in reactor height between the two studies (0.1 m vs 1.1 m), subsequently reducing

the carbon residence time which has been found to correlate to the degree of amorphization of the produced carbon (Rahimi et al., 2019). The trend in the D/G band ratio showed that as the metal became more catalytic, the graphitization of the carbon increased, as the highest D/G band ratio was exhibited in a molten bath of noncatalytic Sn (1.26) and the 2 lowest were in catalytic baths of 95 wt% - Sn 5 wt% - Ni (1.03) & 70 wt% - Sn 30 wt% - Cu (1.11).

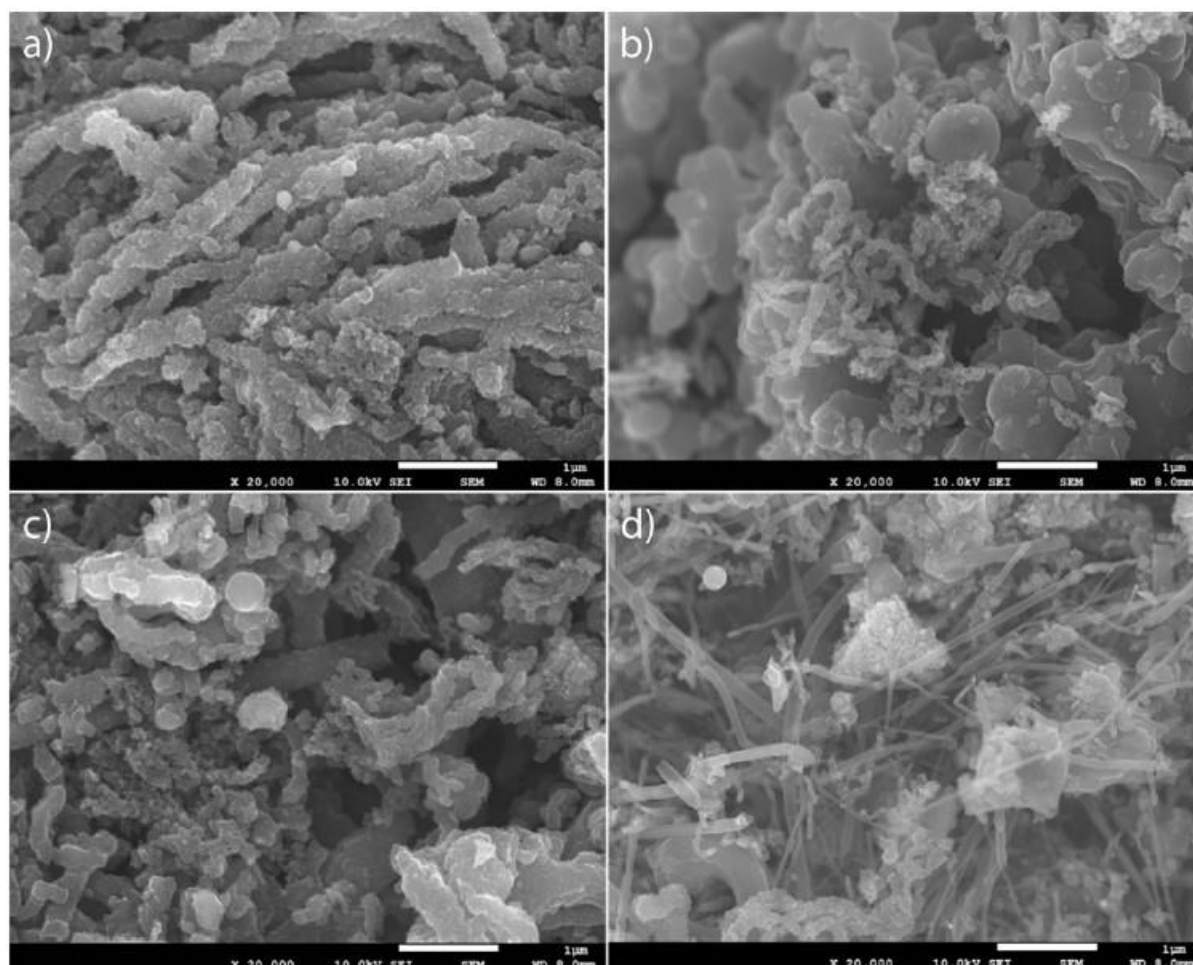


Figure 6. SEM micrographs of carbon obtained from 0.1 m (a) 100 wt% Sn, (b) 95 wt% Sn – 5 wt% Cu, (c) 95 wt% Sn – 5 wt% Ni & (d) 70 wt% Sn – 30 wt% Cu (Zaghloul et al., 2021).

Parkinson et al., (2021) experimentally determined the purity and structural order of carbon produced by the pyrolysis of methane in 0.19 m length monovalent alkali halide salt baths (NaBr, KBr, KCl, NaCl, (Na,K)Br) operating at 1000 °C. Raman spectroscopy revealed that the carbons produced all had D/G band ratios between 0.9-1.1, which is slightly lower than the results of Zaghloul et al., (2021) owing to the slight increase in reactor length between the two

(0.1 m vs. 0.19 m). By combining this information with the results of X-ray photoelectron spectroscopy, which revealed the presence of carbon atoms in the sp^3 configuration by a sharp peak at 284.9 eV, the authors concluded that the carbon is a mixture of nano-crystalline graphite and amorphous carbon. This conclusion was made based on the fact that a mixture of graphite and nano-crystalline graphite has 0% sp^3 carbon.

In a similar study, Palmer et al., (2021) experimentally assessed the quality of solid carbon produced by methane pyrolysis in the same alkali-halide molten salts (NaCl, KCl, NaBr, KBr) at temperatures of 950, 1000, 1050 and 1100°C and a molten salt length of 0.18 m. The Raman spectra of the solid carbon showed that the carbon is a graphitic and amorphous mixture based on the D/G band ratios which were not explicitly stated but appear to be slightly above 1, and that amorphous domains may be slightly more prevalent as the reaction temperature increases due to the widening of the bands at higher temperatures. Their Raman spectra analysis also showed the presence of a 2D peak at $\sim 2700\text{ cm}^{-1}$, which represents the degree of ordering between stacked carbon layers. SEM analysis of carbon samples recovered at different reaction temperatures showed that at temperatures above 1050 °C, the solid carbon grows in sheet-like structures as opposed to the spherical structures exhibited at temperatures below 950 °C. The SEM micrographs from their research are shown in Figure 7.

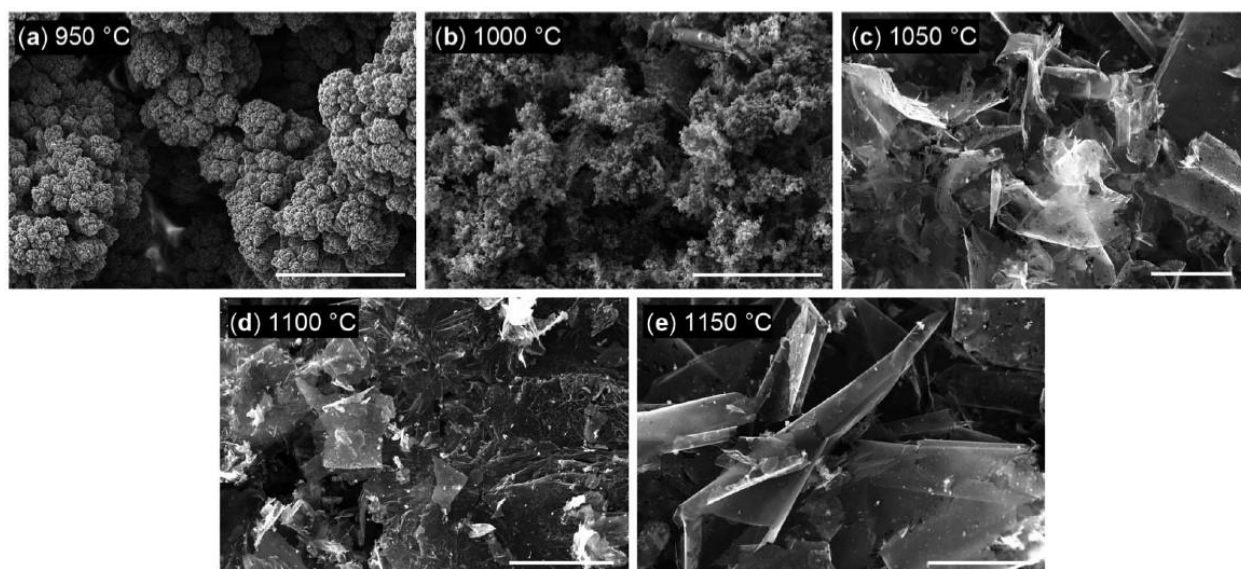


Figure 7. SEM micrographs of carbon obtained from 0.18 m KCl bubble column at different temperatures: (a) 950 °C, (b) 1000 °C, (c) 1050 °C, (d) 1100 °C & (e) 1150 °C. All carbons have been washed in 70 °C water for two hours with constant stirring. Scale bars in all images are 50 μm (C. Palmer et al., 2021).

Rahimi et al., (2019) expanded on the work of Upham et al., (2017) by experimentally studying the effect of adding a molten salt layer of either KBr or NaBr on top of the 27 mol% - Ni 73 mol% - Bi catalytic molten alloy that was at a temperature of 1000 °C. High resolution transmission electron microscopy analysis of the carbon after it was purified revealed that the carbon produced in a two phase reactor (metal and salt) contained carbon black aggregates and carbon nanotube structures, which is in agreement with the 70 wt% - Sn 30 wt% - Cu results of Zaghoul et al., (2021), while in a single phase reactor (metal only) only flakes of graphitic carbon were detected. The SEM micrographs of the produced carbon are shown in Figures 8 & 9 and show the differences in the morphology of the carbon between single and two phase reactor configurations. Raman spectra of carbon samples collected from single and two phase reactors of NiBi and NiBi/KBr showed D/G band ratios between 1.28 and 1.35 and is shown in Figure 10. By comparison with Figure 5, the spectra closely resembles that of graphite 4124 and multiwalled carbon nanotubes (MWCNTs), however due to the confirmation of tubular structures by both Zaghoul et al., (2021) & Rahimi et al., (2019) it is most likely that some of the carbon produced are MWCNTs.

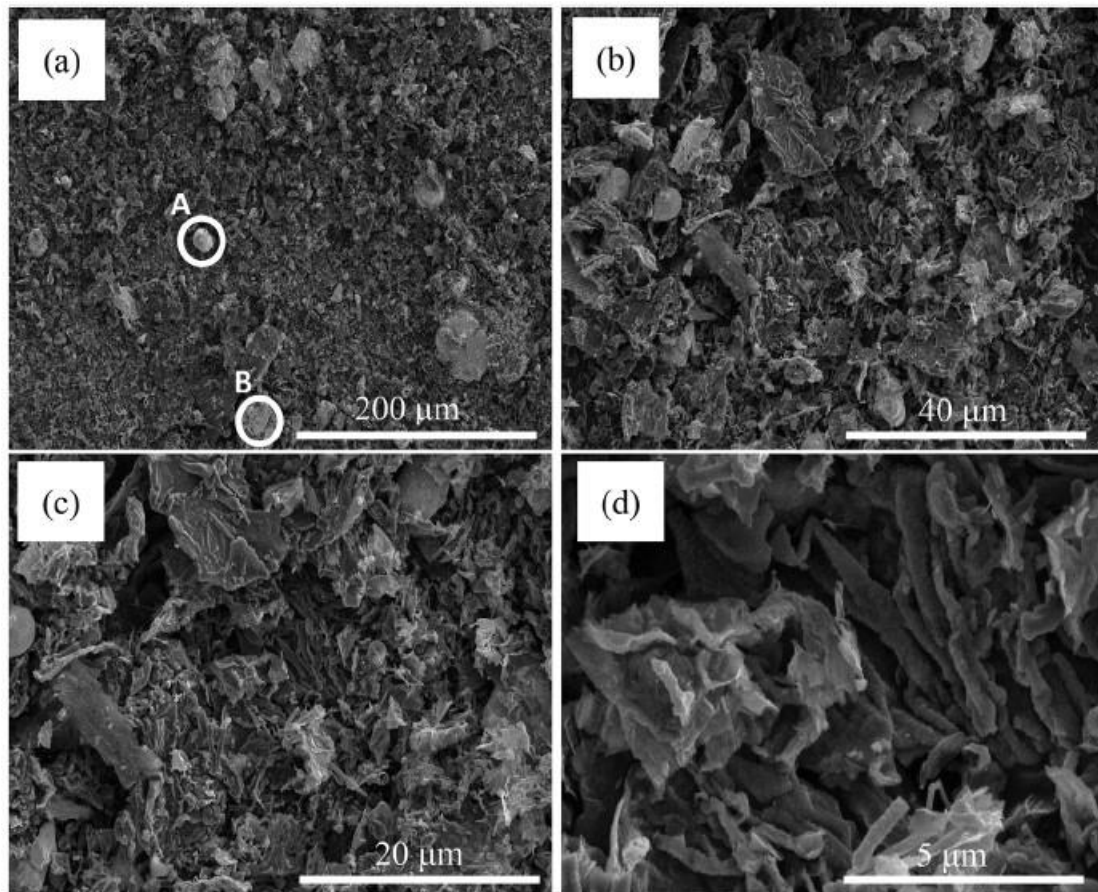


Figure 8. SEM micrographs of carbon samples obtained in 1000 °C NiBi (350 mm) single phase bubble column reactor at different magnifications. A & B indicate the presence of metal particles (Rahimi et al., 2019).

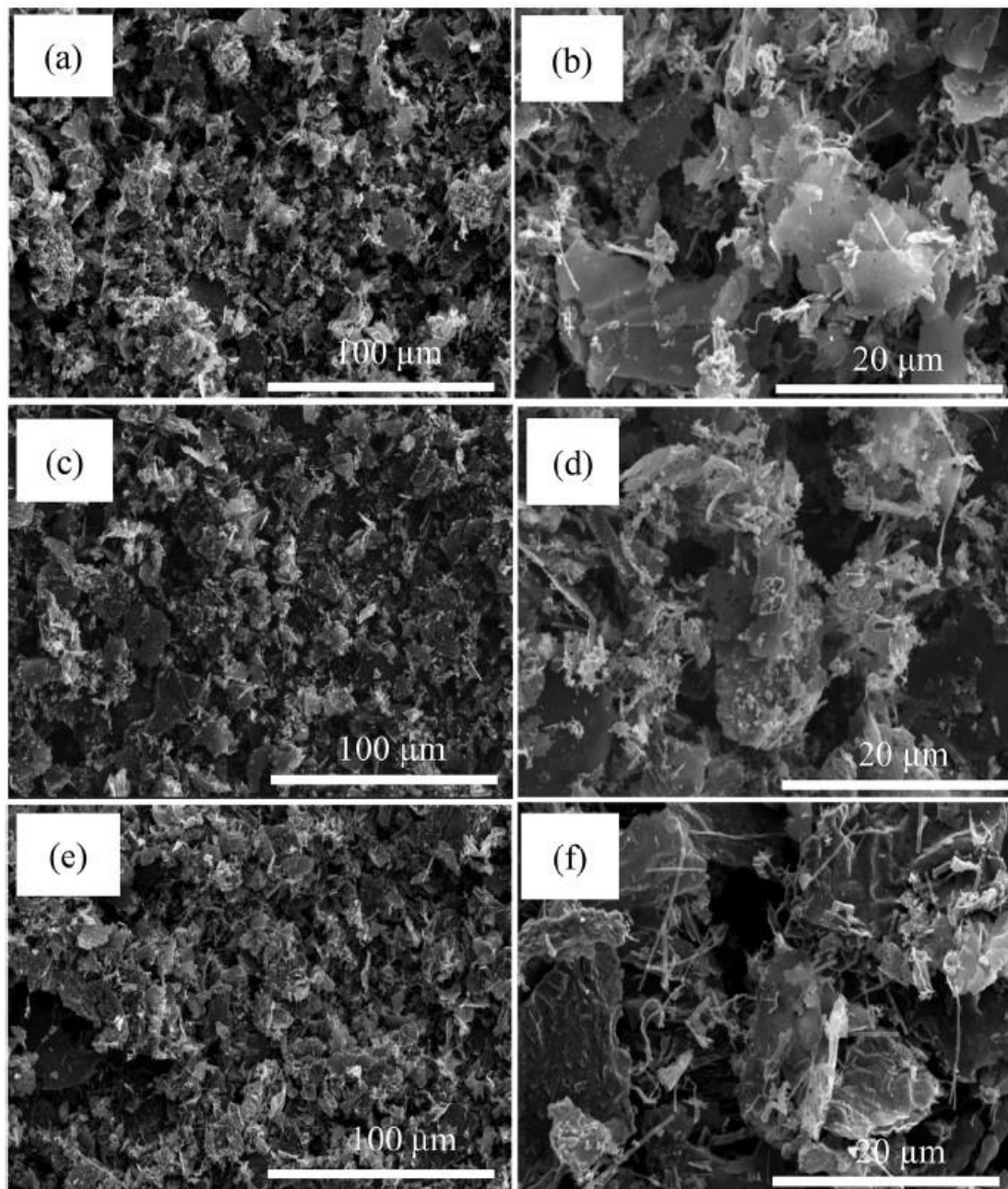


Figure 9. SEM micrographs of carbon samples obtained from 1000 °C (a) & (b) NiBi/KBr (110 mm/240 mm), (c) & (d) NiBi/KBr (240 mm/110 mm) & (e) & (f) NiBi/NaBr (110 mm/240 mm) two phase bubble column reactors (Rahimi et al., 2019).

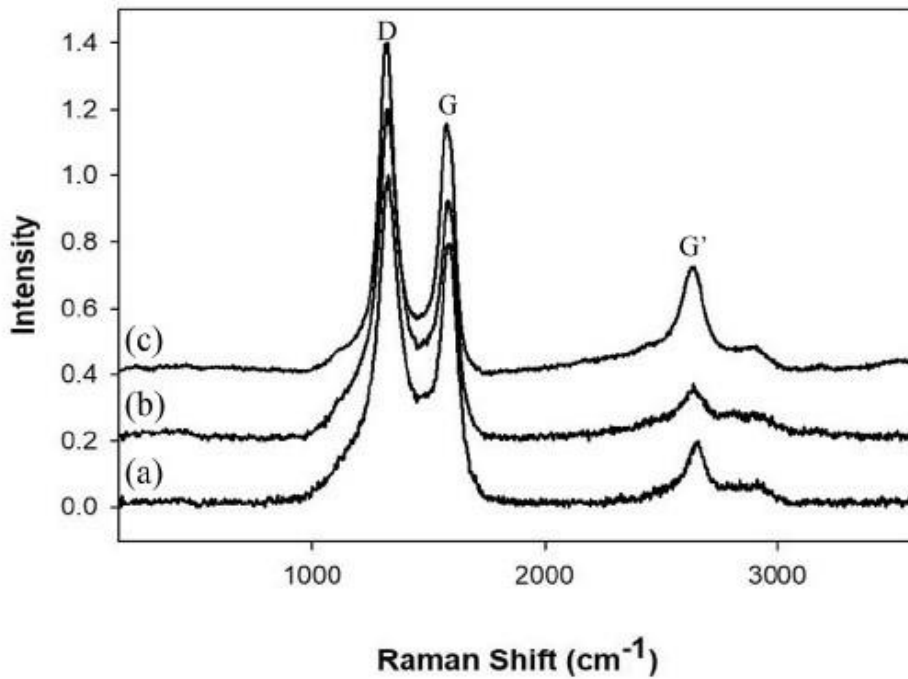


Figure 10. Raman spectra of carbon excited at 633 nm and produced in (a) NiBi, (b) NiBi/KBr (240 mm/110 mm), and (c) NiBi/KBr (110 mm/240 mm) from (Rahimi et al., 2019).

Figure 10 also shows that the resonance G' peak increases in intensity as the thickness of the molten salt layer increases, inferring that structural and microstructural changes could occur as the carbon rises through the salt phase to the liquid surface (Kamali & Fray, 2013). The D/G band intensity ratio also indicates that the degree of amorphization is highly dependent on the residence time of the bubble in the molten phase, as the highest degree of amorphization was observed in the 110 mm NiBi 240 mm KBr configuration, while the lowest was observed in the 240 mm NiBi 110 mm KBr configuration. This is also confirmed by comparison with the results of Upham et al., (2017) who used a 1.1 m LMBR of 27 mol% - Ni 73 mol% - Bi catalytic molten alloy and achieved a D/G band ratio of 0.594 versus the D/G band ratio of 1.30 that Rahimi et al., (2019) observed in a 0.35 m LMBR of the same catalytic metal without the presence of a molten salt layer (Figure 10 (a)).

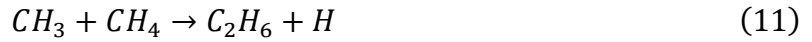
One issue with methane pyrolysis for hydrogen production is the potential interaction between the solid carbon and hydrogen. If the solid carbon were to act as a hydrogen scavenger, this would greatly affect the overall stoichiometry of the process. As was mentioned in the study of

Dennison et al., (1996), hydrogenated carbon with a hydrogen content of 20-50 atomic percent would show a broad tail in the Raman spectra centered around 600 cm^{-1} . This tail is not evident in Figure 10, suggesting that there is no more than 20 at% hydrogen present in the carbon product. Research on the reaction mechanism of coke formation in natural gas and methane pyrolysis is abundant, but primarily for fluidized bed reactors. Fau et al., (2014) perform a literature review on coke formation by pyrolysis of hydrocarbon feeds with a focus on coke produced from methane pyrolysis. In their review they reference the work of Guéret et al., (1995) who studied solid carbon production from methane pyrolysis. In their work the conclusion is drawn that the process of carbon formation begins with pyrolysis of hydrocarbon molecules to form radicals in the gas phase. These radicals participate in condensation and polymerization reactions that give rise to “complexes” that are intermediates in carbon formation. These complexes then produce pyrolytic carbon or carbon black depending on the surface area available. Palmer & Cullis, (1965) showed that the formation of pyrolytic carbon is favoured by deposition on the reactor walls whereas the formation of carbon black occurs in the gas phase. The latter is the faster of the two reactions. This explains the predominance of carbon black formation in CLMBRs compared to fluidized bed reactors, as the diffusion rate of the intermediate complexes through the liquid metal is slow and the diffusion distance may be long in many cases. Expanding on this work, Lucas & Marchand, (1990) proposed a four step mechanism for coke formation beginning with the pyrolysis of methane. They determined that C_2 hydrocarbons (acetylene and ethylene) and benzene were the most represented intermediate complexes while naphthalene, anthracene, phenanthrene, acenaphtylene, pyrene and fluoranthrene were the most common polycyclic aromatic hydrocarbons (PAH). The four-step mechanism they proposed is shown in Equation (9):



The authors noted that the C_2 hydrocarbons played an essential role in the formation of benzene which is the most important intermediate species. This was also confirmed by Benzinger et al., (1996) who presented a five-step mechanism for carbon formation starting with the cracking of methane and shown in Equations (10)-(20):

STEP 1: From methane to ethane:



STEP 2: From ethane to ethylene:



STEP 3: From ethylene to acetylene:



STEP 4: From acetylene to benzene:



STEP 5: Growth of solid carbon (C_∞)



The proposed mechanism shows that hydrogen interacts in the gas phase to ultimately produce benzene. This benzene is necessary to produce solid carbon as shown in step 5 by Equation (20). Additionally, step 5 shows that with the production of the solid carbon, hydrogen is released. As a result, if any hydrogen is scavenged during methane pyrolysis, it would be in the form of undecomposed benzene or other PAHs in the gas phase, and not in the carbon structure.

As well, much research has been performed on the adsorption and desorption of hydrogen by carbon materials for the purpose of hydrogen storage for use in fuel cell vehicles (Kojima et al.,

2006). This process is known as physisorption and is based on weak van der Waals forces between the adsorbate and adsorbent. At room temperature the magnitude of this interaction is of the same order as the thermal motion energy of the gas molecules (Panella et al., 2005). Therefore, lowering the system temperature results in the interaction between the surface and gas molecule becoming stronger than the thermal motion energy of the adsorbate, which is proportional to the temperature (Panella et al., 2005). For this reason, many studies investigate the adsorption of hydrogen by carbon based materials at cryogenic temperatures (usually 77 K) and high pressures (up to 20 MPa) (Kojima et al., 2006; Panella et al., 2005; Ströbel et al., 1999). The overarching problem in the studies surveyed is that the maximum amount of hydrogen that can be stored in carbon at 298 K and 20 MPa is 1.25 wt% when super activated carbon is used (Kojima et al., 2006). Ströbel et al., (1999) found a similar value of 1.5 wt% H₂ at 298 K and 12.5 MPa for activated carbon, while the work of Panella et al., (2005) found a maximum of 0.5 wt% H₂ at 6.5 MPa for activated carbon. The studies of Kojima et al., (2006) and Panella et al., (2005) also investigated the use of single walled carbon nanotubes for hydrogen storage, finding that the storage capacity was less than 1 wt% at room temperature, even at pressures up to 9 MPa. As a result, it can be concluded that the adsorption of hydrogen by carbon is unlikely to occur in a CLMBRs operating at 1100 °C; however, actual experimental data is needed to prove or disprove the adsorption of hydrogen by carbon at the operating conditions of the molten metal reactor.

In summary, carbon produced from methane pyrolysis in molten media reactors at temperatures of at least 950 °C is graphitic amorphous carbon, and when temperatures increase to 1050 °C there is evidence that some of the carbon grows in sheet like structures. When a catalytic molten metal is used with or without a salt cap, the carbon sheets may roll into a tubular structure, which is supported by a Raman spectra that closely resembles that of MWCNTs, as well as the SEM micrographs. As carbon residence time in the molten metal increases, it is apparent that the carbon becomes more graphitic, as evident by a decrease in the D/G band intensity ratio. The carbon may also become more amorphous as the reaction temperature increases due to the widening of both the D & G bands in the Raman spectra. In practicality, it would be nearly impossible to separate the tiny nanotube structures from the

carbon flakes and as a result, the produced carbon is most likely to be sold as graphitic amorphous carbon, also known as carbon black.

1.3.3 Carbon Purity & Cleaning

While classification of the type of carbon produced by the pyrolysis of natural gas in molten media reactors is important, of equal importance is the purity at which it can be obtained. Using x-ray photoelectron spectroscopy, Upham et al., (2017) found that the carbon recovered directly from the top of the 27 mol% - Ni 73 mol% - Bi molten alloy reactor operating at 1050°C had a purity of only 61 wt% carbon, with the main contaminant being Bi (32 wt%). It is therefore evident that some type of cleaning or purification steps must be undertaken to achieve the minimum purity for carbon black applications of 95 wt% (*Carbon Black Prices, News, Market & Analysis | ChemAnalyst*, n.d.).

Parkinson et al., (2021) performed a thermogravimetric analysis on the produced carbon in their alkali halide salt reactors operating at 1000 °C after washing with deionized water until the effluent conductivity reading fell below 5 µS. The results showed that the carbon produced in NaCl molten salt had the highest purity (90.1 wt% carbon) with NaBr producing the second most pure product (74.2 wt% carbon). The potassium based salts KBr, KCl and a eutectic mixture of (Na,K)Br produced solid carbon with purities of 60.9, 65.5 & 63.8 wt% carbon, respectively. These results for carbon purity showed that with a decrease in internuclear spacing in the molten salt, the carbon purity increased. These authors also state that the sodium based salts were the least likely to wet the carbon surfaces resulting in 2 distinct layers of carbon and salt, whereas the potassium based salts wetted the carbon surface resulting in the dispersion of the product carbon in the salt layer. This effect is reflected in the potassium based salts producing carbon with lower purities than the carbon produced in the sodium based salts. Palmer et al., (2021) also assessed the effectiveness of water washing for salt removal from the solid carbon produced in their alkali-halide molten salt reactors at 1000 °C. After washing the solid carbon in 70 °C water for 2 hours, the carbon product was ~35 wt% molten salt when produced in the KCl, KBr & NaBr molten salts, while the NaCl carbon product was only 15 wt%, which is relatively similar to the findings of Parkinson et al., (2021). The authors also attributed this difference to the smaller internuclear spacing that NaCl has

compared to the other salts. The results of both studies indicate that water washing alone cannot achieve the necessary carbon black purity.

Palmer et al., (2021) also assessed the effects of operating temperature as well as the addition of a heat treatment step after water washing on the solid carbon purity. The initial contamination of molten salt in the solid carbon was found to decrease significantly as the pyrolysis temperature increased. For the KCl molten salt, the product carbon contained 36.2 wt% at 950°C but only 8.1% at 1150°C. The study also found that the addition of heat treatment was more effective at cleaning the carbon, as water washing followed by heat treatment at 1100 °C for 12 hours reduced the molten salt contamination in the carbon by a greater margin than water washing alone. The heat treatment was found to be most effective at removing potassium-based salts, as the final molten salt contamination was less than 2 wt% for both KCl & KBr carbon products. It is therefore evident that higher reactor temperatures are advantageous, and that a combination of water washing and heat treatment is necessary to achieve adequate carbon black purity.

Using X-ray fluorescence, Rahimi et al., (2019) analyzed the metal and salt concentration in the carbon produced from 27 mol% - Ni 73 mol% - Bi reactors both with and without molten salt layers operating at 1000°C . Their most successful results revealed that when 240 mm of NaBr molten salt is used on 110 mm of 27 mol% - Ni 73 mol% - Bi, the liquid metal contamination in the solid carbon is only 0.18 ± 0.01 wt% Ni with no detectable Bi, and the molten salt contamination can be reduced to 0.59 ± 0.01 wt% Na and 1.83 ± 0.01 wt% Br after the mixture is washed with deionized water and heated under vacuum to 1000 °C for 12 hours. These results indicate that when using a catalytic liquid metal bath reactor with a layer of molten salt operating at a temperature of at least 1000 °C, a carbon black purity of ≥ 95 wt% is achievable when the product is water washed and heat treated.

1.4. Carbon Black Market

1.4.1 Graphitic Amorphous Carbon (Carbon Black)

Graphitic amorphous carbon, also known as carbon black, is the most commonly occurring end product in solid carbon producing processes and is used primarily as a filler and strengthening agent in tires and other rubber plastic products (Dagle et al., 2017b).

The global market for carbon black was estimated at \$USD 17.5 billion in 2018 and is projected to grow to \$USD 23.0 billion by 2026, growing at a compound annual growth rate of 3.5% (*Carbon Black Market Size, Share | Industry Growth & Forecast, 2026*, n.d.). Dagle et al., (2017) reviewed the US & global markets for amorphous carbon black, which they defined as 97 wt% carbon or higher, for application in tires, printing inks, and high performance coatings and plastics. They found that carbon black had a 2 million tonne (2017) market size in the US and a 12 million tonne (2014) global market size, which the authors projected to increase to 16.4 million tonne in 2022. A Carnol plant producing 2000 tMeOH/d stoichiometrically produces 0.39 million t/year of solid carbon (Equation 8) assuming 100% CH₄ conversion to methanol and carbon, and an onstream factor of 0.95, indicating that this process can easily fit within both markets. The expected carbon price for use in rubber application, which accounts for 90% of carbon black end use (Dagle et al., 2017b), ranges between \$USD 400-1000+/t for ASTM grade carbon black.

(*Carbon Black Prices, News, Market & Analysis | ChemAnalyst*, n.d.) indicated that the North American price of rubber grade carbon black (>=95 wt%) was between \$USD 2555-2645/t from January to March of 2022, and that the price of carbon black depends greatly on the tire industry, which they estimate accounts for more than 60% of the worlds carbon black consumption.

Alibaba has industry grade carbon black (N220, N330 & N660) with carbon purity of 95% for use in tires and has been produced in China for sale at a price between \$USD 898-1050/t (*Industrial Grade 95% Purity Powder Carbon Black N660 Price For Tyre - Buy Tyre Carbon Black,Pigment*

Carbon Black, Carbon Black For Tyre Product on Alibaba.Com, n.d.; Industry Grade 95% Purity Carbon Black N220 N330 For Tire Manufacturer Supplier - Buy Carbon Black Supplier, Carbon Black N330, Carbon Black N220 N330 For Tire Product on Alibaba.Com, n.d.). Additionally, 95% purity carbon black powder for use in rubber is listed at \$USD 1153/t on *(95% Purity Carbon Black, For Rubber, Powder, Rs 90/Kg S. M. Associates | ID: 25619457855, n.d.).*

1.4.2 Graphite

Graphitic carbon possesses a unique combination of physical properties due to its weak interplanar bonds and strong intraplanar bonds. The weak interplanar bonds allow adjacent carbon planes to slide over one another, making it useful as a lubricant or in pencils. The strong intraplanar bonds are covalent and result in a high melting point for the carbon, leading to its application in refractory brick. Additionally, graphite has a combination of high temperature stability, good electrical and thermal conductivity, and is chemically inert, meaning that it can be used in electrodes for spectrochemical analysis, electrochemistry, materials processing, electrical motors (Dennison et al., 1996) and in lithium-ion batteries (Dagle et al., 2017b).

The global market for graphitic carbon was estimated at \$USD 15.3 billion in 2020 and is projected to grow to \$USD 21.5 billion by 2026 (*Carbon and Graphite - Global Market Trajectory & Analytics, n.d.*). The two applications projected to see the most growth are carbon & graphite electrodes (projected 5% compound annual growth rate) and carbon & graphite fibres (projected 8.5% compound annual growth rate). Pruvost et al., (2022) assessed the global market size of carbon anodes, graphite and sorbents to be in the range of 20-50 million tonne/year. In their assessment, this market is also deemed to be the most lucrative, as the sale price can range between \$USD 440-1100/tonne. This price range is corroborated when looking at graphite powder prices on Alibaba.com, where prices range from \$USD 440-463/tonne on the lower end (*High Pure High Carbon 300 Mash Artificial Nano Graphite Powder Price - Buy High Pure Graphite Powder, Graphite Granules, Amorphous Graphite Powder Product on Alibaba.Com, n.d.; High Quality Factory Price Graphite Powder Carbon - Buy Graphite Powder Carbon, Graphite Powder Malaysia, Nickel Graphite Powder Product on Alibaba.Com, n.d.*) to

\$1630-2000/tonne for high purity (99-99.9%) powders (*99.9% Purity Fine Graphite Powder For Lubricant Graphite Price Ton Carbon Graphite Carbon - Buy Carbon Graphite Carbon, Fine Graphite Powder For Lubricant, 99.9% Purity Nano Graphite Powder Price Fine Graphite Powder For Lubricant Product on Alibaba.Com, n.d.*; *China Factory Expanded Graphite 99% Carbon Expanded Graphite Powder Price - Buy Expanded Graphite, Expanded Graphite Powder, High Carbon Graphite Powder For Sale Product on Alibaba.Com, n.d.*).

1.4.3 Multi Walled Carbon Nanotubes

Carbon nanotubes are sheets of graphite that have been rolled into a cylinder and have a very broad range of electronic, thermal and structural properties that change based on the tube diameter, length and chirality (*Applications-and-Benefits-of-Multi-Walled-Carbon, n.d.*).

MWCNTs consist of multiple cylinders inside of each other and are used in areas that include lithium-ion batteries, solar cells, transistors and energy storage (*Applications-and-Benefits-of-Multi-Walled-Carbon, n.d.*).

The global market for carbon nanotubes was assessed at \$USD 876 million in 2021 and is projected to grow to \$USD 1714 million by 2026 at a compound annual growth rate (CAGR) of 14.4% (*Global Carbon Nanotubes (CNT) Market by Type (Single Walled & Multi Walled), End-Use Industry (Electronics & Semiconductors, Chemical Materials & Polymers, Structural Composites, Energy & Storage, Medical), Method, and Region - Forecast to 2026, n.d.*).

(*Multi Walled Carbon Nanotubes Products, n.d.*) have multiwalled carbon nanotubes of various outer diameters (<8nm to 80 nm), all with >95wt% carbon purity that have been prepared using acid chemistry for sale in the price range of \$USD 700-1950/kg, with the most expensive product having the smallest outer diameter.

It is difficult to say where the MWCNT structures produced in CLMBRs fits into the global market as there is limited research in the literature regarding its formation. While both Zaghloul et al., (2021) & Rahimi et al., (2019) report the presence of tubular and “bamboo” like carbon structures as well as the fact that the Raman spectra closely resembles the Raman spectra of

MWCNTs, neither article explicitly states the tube outer diameters or lengths. Additionally, separating these very small structures from the carbon black flakes would be nearly impossible.

1.5. CO₂ Accounting

Because the use of CO₂ as a raw material is the main advantage that the Carnol process has from a CO₂ emissions perspective when compared to a methanol production process based on methane reforming, in order to accurately assess and compare the two processes a comprehensive CO₂ accounting must be performed. The total process CO₂ emissions must consider the indirect CO₂ emissions associated with the procurement of the raw materials (natural gas and CO₂) which are outside the bounds of the simulation, and the emissions associated with utility production (electricity) in addition to the direct plant CO₂ emissions. By doing so, the effectiveness of the Carnol process for CO₂ utilization & emissions minimization over a methanol production process based on methane reforming can be shown.

A downfall of many of the previous studies on CO₂ emissions associated with methanol production is the lack of inclusion of upstream and indirect CO₂ emissions, such as the emissions associated with the natural gas supply chain, electricity production when electricity is imported, or the emissions associated with CO₂ capture. The omission of these emissions results in the reporting of ambitious CO₂ emissions data that does not capture the total emissions of the process. For example, Acquarola et al., (2021) comment on the need for a comprehensive CO₂ accounting in order for the reported values to have meaning. However, the emissions value proposed for their bi-reforming process do not consider any of these upstream CO₂ emissions. Instead, they only consider emissions associated with electricity production, combustion in a fired heater, and high pressure and low pressure steam production. A similar issue is found in the report by Collodi et al., (2017) who present CO₂ emissions data for a combined reforming methanol production processes both with and without carbon capture. The emissions data does not include the CO₂ emissions associated with the natural gas supply chain or the CO₂ emissions associated with electricity import.

Some studies include a comprehensive CO₂ emissions accounting but the difference in the method by which the CO₂ emissions are determined can make comparing different processes

difficult and misleading. For example, Ingham, (2017) compares the plant performance of various methanol production processes based on methane reforming at minimum and maximum electricity import. The study uses the GREET model to estimate the CO₂ emissions in the natural gas supply chain however, when comparing the results of the GREET model to the calculated values determined using the natural gas supply chain emissions information presented by Balcombe et al., (2018), it is found that the GREET model significantly underestimates the CO₂ emissions in the natural gas supply chain.

Another example comes in the case of Narine et al., (2021) who also present comprehensive CO₂ emissions data for auto thermal reforming (ATR), pyrolysis, electrolysis, and SMR methanol production processes both with and without carbon capture. For their indirect CO₂ emissions, they use the values in the Ecoinvent v3.4 database to estimate the emissions from natural gas feedstock, water feedstock, electricity production, MDEA import, wastewater emissions, and process emissions. Their CO₂ emissions associated with carbon capture are broken into two parts. For CO₂ transport, the emissions are estimated using the equation presented by Gonzalez-Diaz et al., (2020) where an emission factor is applied to the total CO₂ captured per tonne of methanol produced. The emissions associated with CO₂ storage are estimated based on the power requirements for CO₂ compression while the fugitive emissions associated with both transport and storage are neglected.

1.5.1 Indirect Emissions – Natural Gas Supply Chain

While including the indirect emissions associated with the natural gas supply chain, CO₂ capture, and electricity import is crucial, the emissions are also associated with a large degree of variability. For example, Balcombe et al., (2018) performed a literature review on the reported CO₂ and methane emissions across the global natural gas supply chain and found a range of 3.6-42.4 g CO_{2e}/ MJ HHV natural gas delivered. The review found that the majority of the reported emissions values for each stage (pre-production, extraction, processing, and transmission, storage & distribution) were in the range of 0-6 g CO_{2e}/MJ HHV resulting in a total supply chain emissions median value of 10.6 g CO_{2e}/ MJ HHV. The authors attributed the large

range to the presence of “super emitters”, found primarily in the pre-production and extraction stages. Super emitters are defined as a piece of equipment or facility in the supply chain that emit disproportionately large quantities of CO₂ or CH₄, skewing the average emissions factors associated with their respective stage. The authors state that super emitters are likely due to the use of inefficient equipment as a result of insufficient maintenance and monitoring procedures, or the fact that the equipment is no longer the best available technique for the duty. Nevertheless, super emitters may present themselves in a supply chain at any moment, and for this reason it is important to evaluate the effectiveness of the process across the entire range of natural gas supply chain emissions factors.

1.5.2 Indirect Emissions – CO₂ Capture

The CO₂ emissions associated with CO₂ capture exhibit the same variability as the natural gas supply chain and electricity import emissions depending on the CO₂ source. Von der Assen et al., (2016) performed a literature review on the CO₂ emissions associated with CO₂ capture from various processes that accounts for the process specific energy demands of heat, electricity and fuel while considering the greenhouse gas emissions associated with the production of these energies. The research found a wide range of emissions factors, from as low as 0.06 tCO_{2e}/ tCO₂ captured when the CO₂ is captured from nearly pure CO₂ streams in hydrogen, ammonia and ethylene oxide production plants as well as in natural gas processing plants that use steam cracking, to values as high as 0.44 tCO₂/tCO₂ captured when CO₂ is captured directly from the atmosphere. The average value of 0.20 tCO₂/tCO₂ captured very closely represents the emissions when CO₂ is captured from natural gas combined cycle and integrated gas combined cycle power plants (0.21 & 0.17 tCO₂/tCO₂ captured, respectively). These emissions factors do not take into account the CO₂ emissions associated with the transport of the product CO₂ which is estimated by von der Assen et al., (2016) to be 0.002 tCO₂/tCO₂ per 100 km when the CO₂ is transported by pipeline. Von der Assen et al., (2016) also found that the emissions associated with CO₂ transport were mostly below 0.02 tCO₂/tCO₂ regardless of the transportation method, which is relatively small compared to the emissions associated with CO₂ capture.

The source of CO₂ capture not only influences the CO₂ emissions but also the price of the CO₂. The International Energy Agency (IEA) presents data on the cost of CO₂ capture in various sectors (IEA, *Levelised Cost of CO₂ Capture by Sector and Initial CO₂ Concentration, 2019*, IEA, Paris). The data shows that the cost of capture is directly related to the concentration of CO₂ in the stream that it is being captured from. High concentration streams from ethylene oxide, bioethanol, ammonia and natural gas processing plants all have cost between \$USD 15-35/tCO₂, while the high concentration stream from an SMR plant has a slightly higher cost of \$USD 50-80/tCO₂. Low concentration streams, such as those from cement and iron & steel plants have higher costs between \$USD 40-120/tCO₂, while CO₂ captured directly from the air has a wide range of prices between \$USD 134-342/tCO₂. Interestingly, the sources of CO₂ with the lowest CO₂ emissions per tonne of CO₂ captured, also have the lowest price per tonne of CO₂, that being the ammonia and ethylene oxide plants. On the other hand, direct air capture has the highest CO₂ emissions per tonne of CO₂ captured as well as the highest price.

1.5.3 Indirect Emissions – Electricity Import

The CO₂ emissions associated with electricity import also vary based on the production method. In this study the lower bound is taken to be 0 tCO_{2-e}/GJ for renewable electricity sources, while the upper bound is taken to be 0.273 tCO_{2-e}/GJ which is the 2019 average value for electricity produced by coal-fired power stations in the US (*Data Explorer | US EPA*, n.d.). The base value of 0.1203 tCO_{2-e}/GJ represents the average value for electricity consumed from the US grid in 2019 (*Greenhouse Gases Equivalencies Calculator - Calculations and References | Energy and the Environment | US EPA*, n.d.).

1.6 Knowledge Gaps & Objectives of this Research

Up to this point, there have been many studies on methane pyrolysis in LMBRs and CLMBRs for the purpose of hydrogen production, many of which were reviewed in Section 1.2. The pairing of hydrogen production by methane pyrolysis in LMBRs with methanol production (Carnol process) has previously been suggested by Steinberg, (1996). Steinberg's analysis is based on a

PR with 100% CH₄ conversion of a pure CH₄ feed where a portion of the produced hydrogen is used to satisfy the methane pyrolysis heat of reaction, and the rest is reacted with CO₂ to produce methanol and water. The simplified thermodynamic analysis does not account for pressure changes or heat losses in cooling water or stack gases. These factors contribute to an unrealistic thermal efficiency. The process developed in this work improves on these shortcomings by utilizing a combined kinetic and hydrodynamic catalytic PR model that accurately determines the reactor operating pressures, and liquid metal volume for the pyrolysis of a realistic natural gas feed at a set operating temperature, natural gas flow rate and CH₄ conversion. By simulating the entire process in Aspen Hysys™, it is possible to perform a detailed mass & energy balance and calculate a more realistic process thermal efficiency.

In recent years, there have been studies on the coupling of methane pyrolysis with methanol synthesis such as the one presented by Narine et al., (2021). In their process, which was simulated in Aspen Plus, natural gas is pyrolyzed in a non-catalytic fluidized bed reactor with a CH₄ conversion of 95% that operates at 1500 °C and 30 bar to produce hydrogen. The hydrogen is then reacted with CO₂ at 240 °C & 50 bar to produce methanol, which is further purified to grade AA (>99.85 wt%) quality. The process energy demands are satisfied by combustion of natural gas and process off-gas. A mass & energy balance is performed but stream specific information is not provided, making it difficult to compare processes on the same basis. As well, the reactor operating conditions are based on the 2018 pilot moving bed reactor of BASF, who confirmed successful lab scale operation in their 2021 annual program review meeting (Bode & Flick, 2021) but also stated that the reactor was ruined during sample production and that there is still need for basic R&D and a new reactor design. The present research uses the combined kinetic & hydrodynamic catalytic PR model that is based on a technology that has been proven successful for methane pyrolysis by various researchers, many of which were covered in Section 1.2. This research also provides a detailed mass and energy balance where the details are provided regarding the determination of the CO₂ emissions at all sources.

To summarize, the present study involves the design and simulation of a novel Carnol process that is based on a combined kinetic & hydrodynamic catalytic PR model where the assessment of the process performance includes an accurate and comprehensive CO₂ accounting. The

process flow sheet is described in detail in Chapter 2 of this work and the modelling and simulation methodology of key process units is subsequently explained in Chapter 3. Chapter 4 presents the process performance from an energetic and CO₂ emissions perspective, the results of which are then compared to the performance of traditional methanol synthesis processes based on methane reforming as well as methanol synthesis processes based on methane pyrolysis. Chapter 4 also includes a sensitivity analysis on the indirect CO₂ emissions factors in order to observe the “best” and “worst” case CO₂ emissions for all processes. The economics of the process is presented in Chapter 5 where the levelized cost of carbon (LCOC) is determined and a sensitivity analysis on key economic parameters is performed to determine the economic viability of the process.

Chapter 2. Overall Methanol Production Process Description

2.1 Block Flow Diagram

A block flow diagram of the process with a production capacity of 2000 t/d of grade AA methanol (99.85 wt% pure) is shown in Figure 11. The first stage is the pyrolysis reactor (PR) which converts the hydrocarbons present in the natural gas feed to hydrogen and solid carbon. The solid carbon is removed as a by-product after cooling, while the hydrogen-rich product gas is fed to a pressure swing adsorber (PSA) which separates most of the hydrogen from the unconverted hydrocarbons and inerts (e.g., N₂) originally present in the natural gas. The pure hydrogen leaving the PSA mixes with the process CO₂ feed and internal CO₂ recycle stream and enters the methanol synthesis reactor (MSR). The crude methanol leaving the MSR contains unreacted H₂ and CO₂, as well as CO produced by the reverse water gas shift reaction. These gases are separated from methanol and water in the separation & distillation section and recycled to the MSR inlet. A small purge is necessary to prevent the accumulation of CO in the recycle loop. The methane-rich purge from the PSA and the recycle loop purge are combined and fed as fuel in the fired heater. The fired heater is used to heat the PR tubes containing liquid metal catalyst, preheat several streams, and superheat utility steam for the process.

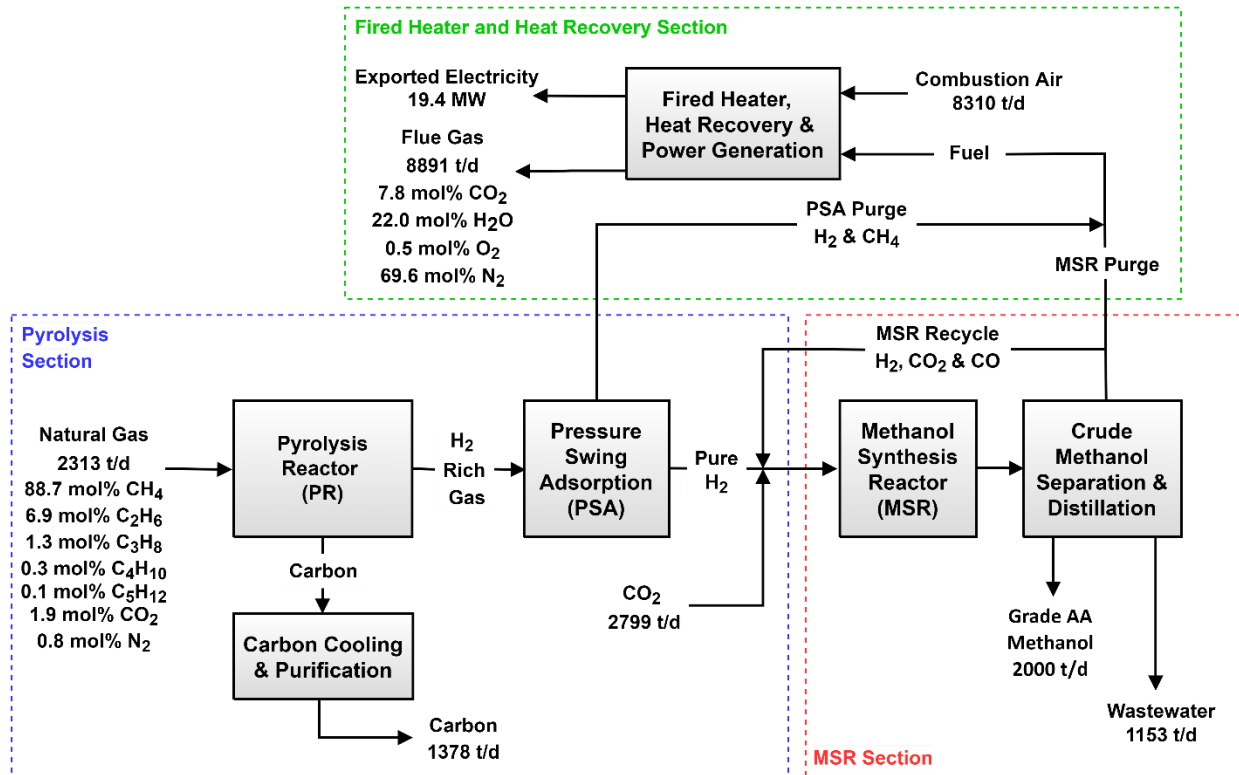


Figure 11. Process block flow diagram.

2.2 Process Flow Diagram

Figures 12, 13 & 14 show the process flow diagrams of the PR, MSR, and heat recovery sections, respectively. Stream information is provided in Tables 1 & 2 at the end of this section. In Figure 12, natural gas enters the process from the natural gas pipeline at 25°C and 10 MPa, which is within typical pipeline pressure ranges (*The Transportation of Natural Gas NaturalGas.Org*, n.d.). Its composition consists of 89% CH₄, 7% C₂H₆, 2% CO₂, 1% C₃H₈, 1% N₂ and traces of C₄H₁₀, C₅H₁₂, and C₆H₁₄, similar to Collodi et al (2017). The natural gas expands down to 1911 kPa in expander EX-101, which is combined with an electrical generator to produce electricity used to satisfy the electrical needs of the air-cooled heat exchangers, air blower & cooling water tower blower. The natural gas is subsequently preheated by the PR outlet gas in E-101 to a temperature of 800 °C. At this temperature, the pyrolysis of methane is extremely slow (Catalan & Rezaei, 2020) but some pyrolysis of higher hydrocarbons is possible and may require frequent cleaning of the tubes in E-101. The natural gas then enters the PR (R-100) which operates at a temperature of 1100 °C. In the PR, all the C₂+ hydrocarbons (ethane, propane,

etc.) fully decompose to hydrogen and carbon (Serban et al., 2003). The percent conversion of CH_4 depends on the size, design, and operating conditions of the PR (Catalan and Rezaei, 2022). In the present process, the methane conversion is set at 80%, as this conversion maintains the expensive liquid metal volume below 100 m^3 , while also minimizing the CO_2 emissions as is explained later in Section 3.1. The carbon exiting the PR exchanges heat with the MSR feed in the plate heat exchanger E-105 and is later cooled to $40 \text{ }^\circ\text{C}$ in the plate heat exchanger E-106. The PR product gas preheats the natural gas feed in E-101 and boiler feed water (BFW) in E-102 & E-103 and is compressed and cooled again to $35 \text{ }^\circ\text{C}$ and 3400 kPa in K-101 & E-104. Next, the product gas enters the PSA (PU-100) at 3400 kPa and $35 \text{ }^\circ\text{C}$. At these operating conditions, the PSA can recover 90% of the hydrogen at a purity $> 99.99\%$, as shown by Luberti (2015) using a nine-column configuration and a similar feed composition. The PSA produces a pure H_2 stream at 3400 kPa and a methane rich purge at atmospheric pressure which is used as fuel in the fired heater.

The pure hydrogen stream is compressed to 8025 kPa in K-102 and mixed with three other streams to form the feed to the MSR. The first stream is pure CO_2 at $10,000 \text{ kPa}$ and 25°C from a CO_2 pipeline. This high pressure is within the range of available CO_2 pipeline pressures (Morgan, 2019). The CO_2 feed is depressurized to 8025 kPa with a valve. The second stream is the recycle loop of the MSR and consists mostly of H_2 and CO_2 which are re-compressed to 8025 kPa by compressor K-103. The third stream originates as off-gas at 120 kPa from the distillation section and is composed predominantly of CO_2 . This stream is re-compressed to 8025 kPa in a train consisting of compressors K-104 to K-106 and intercoolers E-113 & E-114. The MSR feed is preheated to $255 \text{ }^\circ\text{C}$ by flowing successively in the plate heat exchanger E-106 and in the convective zone of the fired heater (E-107, Figure 14).

The MSR (R-101, Figure 13) operates at $255 \text{ }^\circ\text{C}$ and 8000 kPa . Because methanol synthesis is exothermic, the reactor tubes are cooled by vaporizing boiler feed water in the shell, thus producing saturated medium-pressure steam (MPS).

The crude methanol exiting the MSR is used as heating fluid in the reboilers E-109 and E-108 of the distillation towers T-101 & T-102, respectively. Further cooling of the crude methanol

occurs in E-110, E-111 & E-112 by exchanging heat with the MSR recycle loop, in an air-cooled heat exchanger, and cooling water, respectively. Next, the crude methanol now at 40°C enters the high-pressure flash separator V-101 where most of the unreacted CO₂, H₂ and CO report to the gas phase and are recycled to the MSR inlet. A small purge stream is necessary to prevent the accumulation of CO in the MSR recycle loop. The liquid outlet of V-101 is depressurized by a valve to 238 kPa and enters the low-pressure flash separator V-101 where more CO₂ is removed.

The liquid leaving V-101 is treated in the topping tower T-101 which removes nearly all the remaining CO₂, CO, and H₂ as off-gas which is combined with the gas from V-101, recompressed, and recycled to the MSR inlet as previously shown in Figure 12. The bottoms of T-101 consist of an equimolar mixture of methanol and water which is sent to the distillation tower T-102 to produce grade AA quality (99.85 wt%) methanol and wastewater.

The process flow diagram of the fired heater and heat recovery section is shown in Figure 14. The fired heater is fueled by the methane rich purge leaving the PSA and the MSR loop purge. The radiant (hottest) zone of the fired heater houses the PR vertical tubes filled with molten metal catalyst (Catalan and Rezaei, 2022). Hot flue gas leaving the radiant zone heats the saturated MPS from the MSR shell in the convective zone to generate superheated MPS at 500°C and 4019 kPa, as well as saturated BFW at 253°C and 4039 kPa for use as cooling fluid in the MSR, the MSR feed and combustion air that is preheated to 150 °C before entering the burners. The superheated steam leaving E-120 mixes with quench BFW to produce desuperheated steam and is again superheated in E-121 by the process flue gas to produce a larger quantity of superheated MPS at 500 °C & 3999 kPa. The resulting steam expands through two turbines in parallel, TU-101 & TU-102, to 10 kPa. In TU-101, the shaft power required by the process compressors is produced while TU-102 uses the remaining superheated steam to produce electricity that is sold as product. The turbine exhaust is condensed in surface condenser E-122 with cooling water. The condensate is then pumped to 170 kPa in P-101 and mixed with makeup BFW that is subsequently heated in E-103 to 103 °C and fed to the deaerator along with a portion of the saturated steam produced in the MSR shell. The boiler feed water exiting the deaerator is pumped to 4047 kPa in P-103 and fed to boiler feed water

consuming units in the process. Boiler feed water make-up is added via pump P-102 to compensate for the blowdown and other losses in the steam circuit.

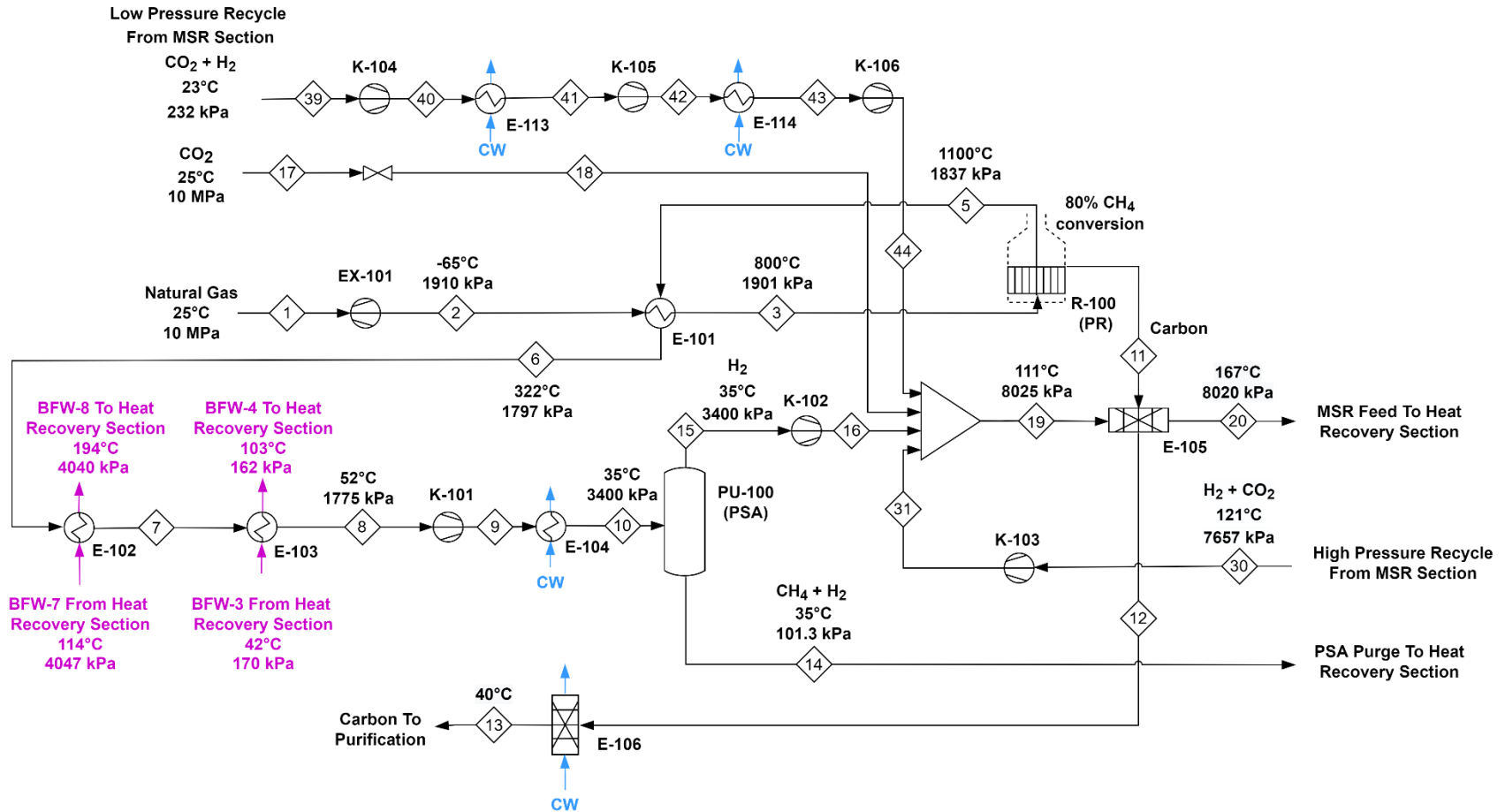


Figure 12. Process flow diagram of the pyrolysis section; E: heat exchanger EX: gas expander, K: compressor, PU: PSA unit, R: reactor.

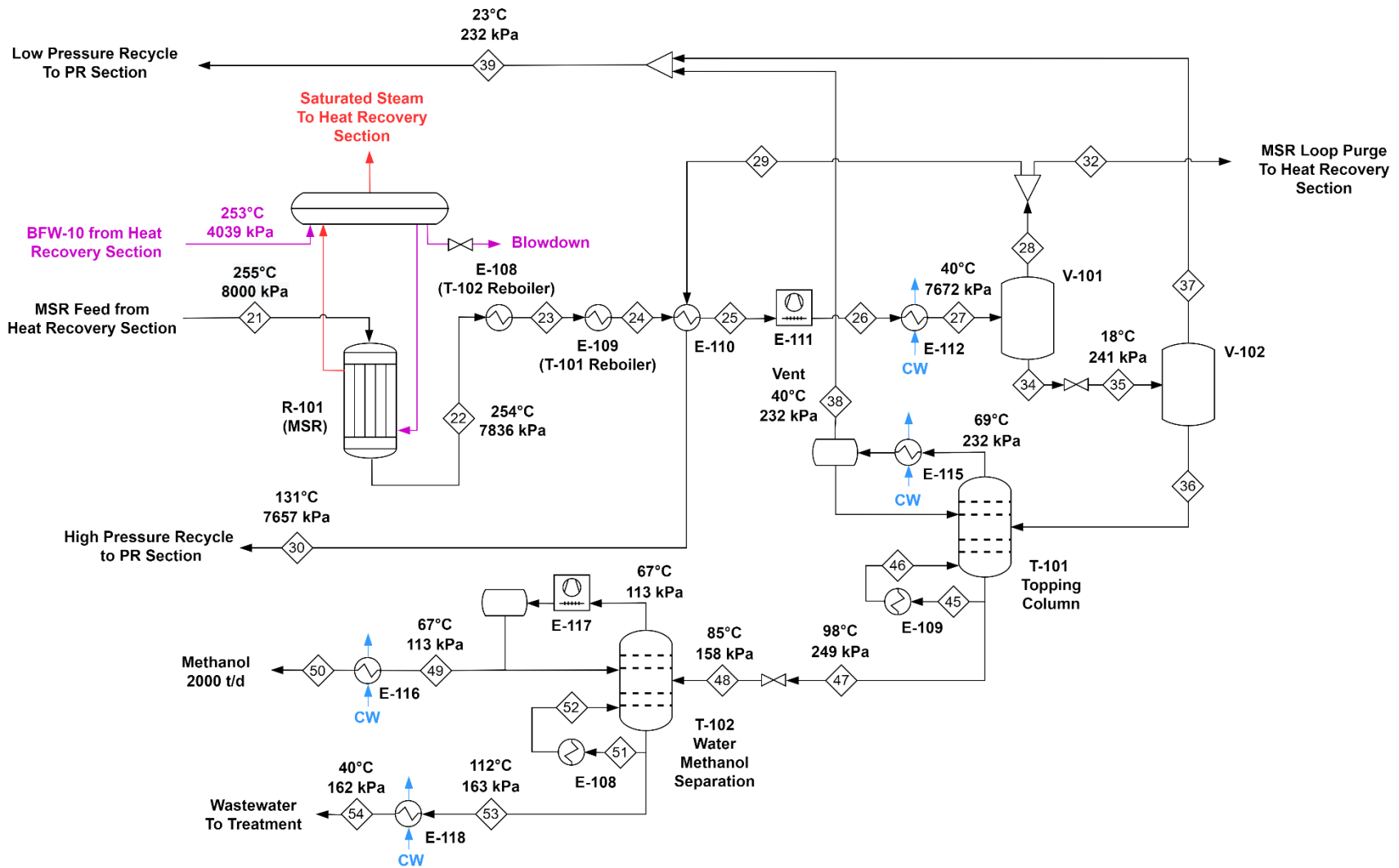


Figure 13. Process flow diagram of the MSR section; E: heat exchanger, R: reactor, T: tower, and V: vessel.

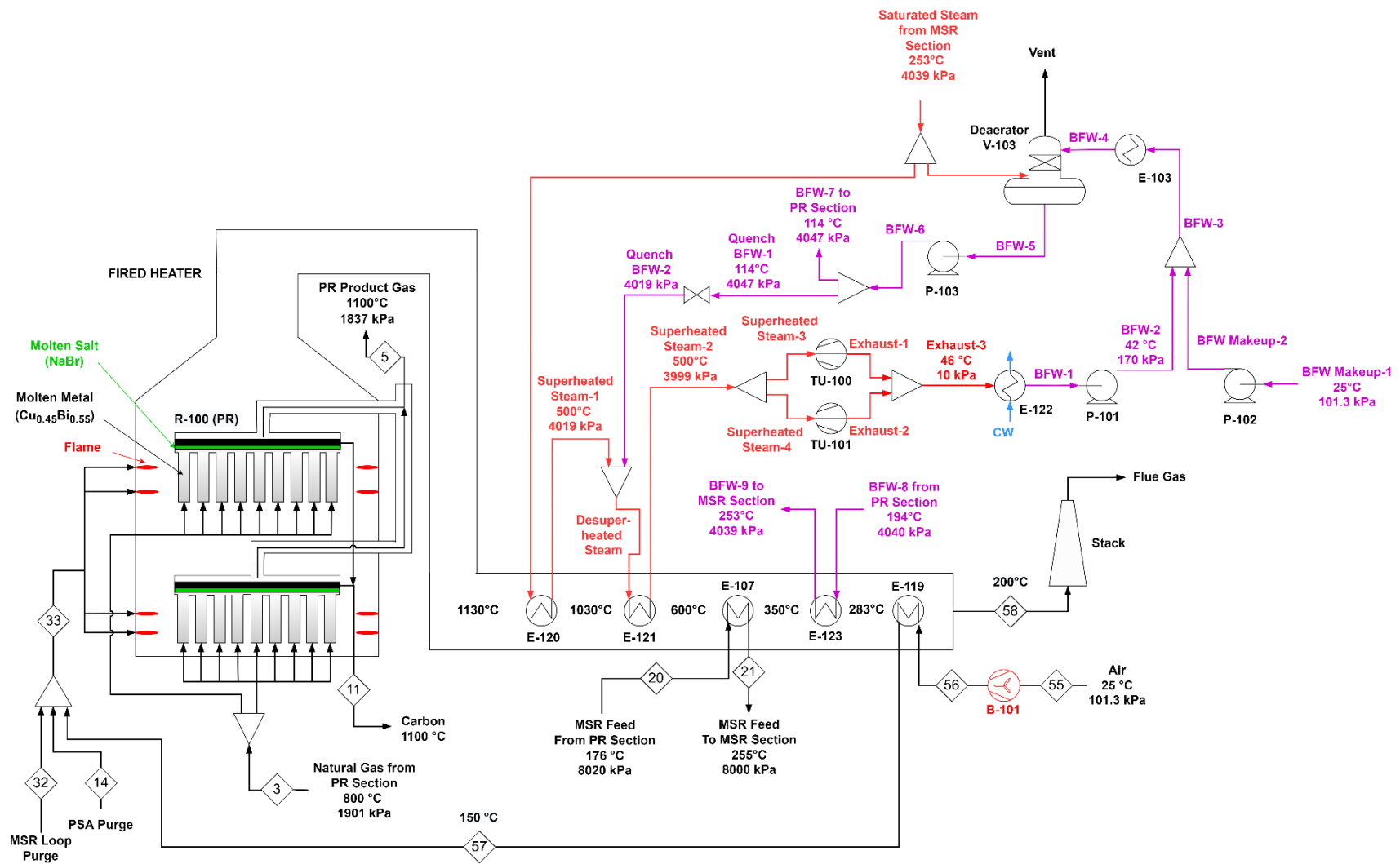


Figure 14. Process flow diagram of the fired heater and heat recovery section; B: blower, E: heat exchanger, P: pump, R: reactor, TU: steam turbine.

Table 1. Stream summary

Stream Number	1	2	3	4	5	6	7	8	9	10	11	12
Vapour Fraction	1	0.98	1	1	1	1	1	1	1	1	0	0
Temperature (°C)	25.0	-64.8	800	1100	1100	321.8	204.1	52.0	147.3	35	1100	121.1
Pressure (kPa)	10000	1910	1901	1901	1837	1797	1786	1775	3405	3400	1837	1832
Molar Flow (kmol/h)	5306	5306	5306	5306	10090	10090	10090	10090	10090	10090	4779	4779
Mass Flow (kg/h)	96390	96390	96390	96390	38990	38990	38990	38990	38990	38990	57400	57400
Mole Fraction												
CH ₄	0.8871	0.8871	0.8871	0.8871	0.0933	0.0933	0.0933	0.0933	0.0933	0.0933	0.0000	0.0000
C ₂ H ₆	0.0693	0.0693	0.0693	0.0693	0.0000	0.0000	0.0000	0.0000	0.0000	0.0000	0.0000	0.0000
C ₃ H ₈	0.0125	0.0125	0.0125	0.0125	0.0000	0.0000	0.0000	0.0000	0.0000	0.0000	0.0000	0.0000
n-C ₄ H ₁₀	0.0028	0.0028	0.0028	0.0028	0.0000	0.0000	0.0000	0.0000	0.0000	0.0000	0.0000	0.0000
n-C ₅ H ₁₂	0.0005	0.0005	0.0005	0.0005	0.0000	0.0000	0.0000	0.0000	0.0000	0.0000	0.0000	0.0000
n-C ₆ H ₁₄	0.0002	0.0002	0.0002	0.0002	0.0000	0.0000	0.0000	0.0000	0.0000	0.0000	0.0000	0.0000
N ₂	0.0082	0.0082	0.0082	0.0082	0.0043	0.0043	0.0043	0.0043	0.0043	0.0043	0.0000	0.0000
O ₂	0.0000	0.0000	0.0000	0.0000	0.0000	0.0000	0.0000	0.0000	0.0000	0.0000	0.0000	0.0000
H ₂ O	0.0000	0.0000	0.0000	0.0000	0.0000	0.0000	0.0000	0.0000	0.0000	0.0000	0.0000	0.0000
CO ₂	0.0194	0.0194	0.0194	0.0194	0.0102	0.0102	0.0102	0.0102	0.0102	0.0102	0.0000	0.0000
CO	0.0000	0.0000	0.0000	0.0000	0.0000	0.0000	0.0000	0.0000	0.0000	0.0000	0.0000	0.0000
CH ₃ OH	0.0000	0.0000	0.0000	0.0000	0.0000	0.0000	0.0000	0.0000	0.0000	0.0000	0.0000	0.0000
H ₂	0.0000	0.0000	0.0000	0.0000	0.8921	0.8921	0.8921	0.8921	0.8921	0.8921	0.0000	0.0000
C	0.0000	0.0000	0.0000	0.0000	0.0000	0.0000	0.0000	0.0000	0.0000	0.0000	1.0000	1.0000

Continued...

Stream Number	13	14	15	16	17	18	19	20	21	22	23	24
Vapour Fraction	0	1	1	1	0	0	1	1	1	1	0.98	0.96
Temperature (°C)	40.0	34.7	34.7	168.4	25.0	22.3	116.1	176.2	255	253.5	145	135.3
Pressure (kPa)	1827	101.3	3400	8025	10000	8025	8025	8020	8000	7836	7817	7799
Molar Flow (kmol/h)	4779	2139	7946	7946	2650	2650	45090	45090	45090	39840	39840	39840
Mass Flow (kg/h)	57400	22970	16020	16020	116600	116600	582000	582000	582000	582000	582000	582000
Mole Fraction												
CH ₄	0.0000	0.4389	0.0000	0.0000	0.0000	0.0000	0.0000	0.0000	0.0000	0.0000	0.0000	0.0000
C ₂ H ₆	0.0000	0.0000	0.0000	0.0000	0.0000	0.0000	0.0000	0.0000	0.0000	0.0000	0.0000	0.0000
C ₃ H ₈	0.0000	0.0000	0.0000	0.0000	0.0000	0.0000	0.0000	0.0000	0.0000	0.0000	0.0000	0.0000
n-C ₄ H ₁₀	0.0000	0.0000	0.0000	0.0000	0.0000	0.0000	0.0000	0.0000	0.0000	0.0000	0.0000	0.0000
n-C ₅ H ₁₂	0.0000	0.0000	0.0000	0.0000	0.0000	0.0000	0.0000	0.0000	0.0000	0.0000	0.0000	0.0000
n-C ₆ H ₁₄	0.0000	0.0000	0.0000	0.0000	0.0000	0.0000	0.0000	0.0000	0.0000	0.0000	0.0000	0.0000
N ₂	0.0000	0.0203	0.0000	0.0000	0.0000	0.0000	0.0000	0.0000	0.0000	0.0000	0.0000	0.0000
O ₂	0.0000	0.0000	0.0000	0.0000	0.0000	0.0000	0.0000	0.0000	0.0000	0.0000	0.0000	0.0000
H ₂ O	0.0000	0.0000	0.0000	0.0000	0.0000	0.0000	0.0006	0.0006	0.0006	0.0667	0.0667	0.0667
CO ₂	0.0000	0.0480	0.0000	0.0000	1.0000	1.0000	0.2434	0.2434	0.2434	0.2096	0.2096	0.2096
CO	0.0000	0.0000	0.0000	0.0000	0.0000	0.0000	0.0216	0.0216	0.0216	0.0246	0.0246	0.0246
CH ₃ OH	0.0000	0.0000	0.0000	0.0000	0.0000	0.0000	0.0032	0.0032	0.0032	0.0695	0.0695	0.0695
H ₂	0.0000	0.4929	1.0000	1.0000	0.0000	0.0000	0.7310	0.7310	0.7310	0.6297	0.6297	0.6297
C	1.0000	0.0000	0.0000	0.0000	0.0000	0.0000	0.0000	0.0000	0.0000	0.0000	0.0000	0.0000

Continued...

Stream Number	25	26	27	28	29	30	31	32	33	34	35	36
Vapour Fraction	0.91	0.87	0.86	1	1	1	1	1	1	0	0	0
Temperature (°C)	110.2	65.0	40.0	40.0	40.0	130.9	137.9	40.0	34.7	40.0	18.1	18.1
Pressure (kPa)	7785	7697	7672	7672	7672	7657	8025	7672	101.3	7672	241	241
Molar Flow (kmol/h)	39840	39840	39840	34090	33990	33990	33990	100	2239	5751	5751	5341
Mass Flow (kg/h)	582000	582000	582000	432400	431100	431100	431100	1268	24240	149700	149700	135100
Mole Fraction												
CH ₄	0.0000	0.0000	0.0000	0.0000	0.0000	0.0000	0.0000	0.0000	0.4205	0.0000	0.0000	0.0000
C ₂ H ₆	0.0000	0.0000	0.0000	0.0000	0.0000	0.0000	0.0000	0.0000	0.0000	0.0000	0.0000	0.0000
C ₃ H ₈	0.0000	0.0000	0.0000	0.0000	0.0000	0.0000	0.0000	0.0000	0.0000	0.0000	0.0000	0.0000
n-C ₄ H ₁₀	0.0000	0.0000	0.0000	0.0000	0.0000	0.0000	0.0000	0.0000	0.0000	0.0000	0.0000	0.0000
n-C ₅ H ₁₂	0.0000	0.0000	0.0000	0.0000	0.0000	0.0000	0.0000	0.0000	0.0000	0.0000	0.0000	0.0000
n-C ₆ H ₁₄	0.0000	0.0000	0.0000	0.0000	0.0000	0.0000	0.0000	0.0000	0.0000	0.0000	0.0000	0.0000
N ₂	0.0000	0.0000	0.0000	0.0000	0.0000	0.0000	0.0000	0.0000	0.0194	0.0000	0.0000	0.0000
O ₂	0.0000	0.0000	0.0000	0.0000	0.0000	0.0000	0.0000	0.0000	0.0000	0.0000	0.0000	0.0000
H ₂ O	0.0667	0.0667	0.0667	0.0008	0.0008	0.0008	0.0008	0.0008	0.0000	0.4571	0.4571	0.4918
CO ₂	0.2096	0.2096	0.2096	0.2341	0.2341	0.2341	0.2341	0.2341	0.0564	0.0639	0.0639	0.0128
CO	0.0246	0.0246	0.0246	0.0275	0.0275	0.0275	0.0275	0.0275	0.0012	0.0072	0.0072	0.0014
CH ₃ OH	0.0695	0.0695	0.0695	0.0036	0.0036	0.0036	0.0036	0.0036	0.0002	0.4605	0.4605	0.4938
H ₂	0.6297	0.6297	0.6297	0.7340	0.7340	0.7340	0.7340	0.7340	0.5022	0.0114	0.0114	0.0001
C	0.0000	0.0000	0.0000	0.0000	0.0000	0.0000	0.0000	0.0000	0.0000	0.0000	0.0000	0.0000

Continued...

Stream Number	37	38	39	40	41	42	43	44	45	46	47	48
Vapour Fraction	1	1	1	1	1	1	1	1	0	1	0	0.04
Temperature (°C)	18.1	40.0	22.7	185.0	49.5	190.0	73.3	205.9	91.9	94.0	98.1	85.2
Pressure (kPa)	241	232.3	232.3	948.9	933.1	2918	2908	8025	240.0	215.9	249.0	158.0
Molar Flow (kmol/h)	410.6	90.4	500.9	500.9	500.9	500.9	500.9	500.9	1274	1274	5250	5250
Mass Flow (kg/h)	14620	3673	18290	18290	18290	18290	18290	18290	36700	36700	131400	131400
Mole Fraction												
CH ₄	0.0000	0.0000	0.0000	0.0000	0.0000	0.0000	0.0000	0.0000	0.0000	0.0000	0.0000	0.0000
C ₂ H ₆	0.0000	0.0000	0.0000	0.0000	0.0000	0.0000	0.0000	0.0000	0.0000	0.0000	0.0000	0.0000
C ₃ H ₈	0.0000	0.0000	0.0000	0.0000	0.0000	0.0000	0.0000	0.0000	0.0000	0.0000	0.0000	0.0000
n-C ₄ H ₁₀	0.0000	0.0000	0.0000	0.0000	0.0000	0.0000	0.0000	0.0000	0.0000	0.0000	0.0000	0.0000
n-C ₅ H ₁₂	0.0000	0.0000	0.0000	0.0000	0.0000	0.0000	0.0000	0.0000	0.0000	0.0000	0.0000	0.0000
n-C ₆ H ₁₄	0.0000	0.0000	0.0000	0.0000	0.0000	0.0000	0.0000	0.0000	0.0000	0.0000	0.0000	0.0000
N ₂	0.0000	0.0000	0.0000	0.0000	0.0000	0.0000	0.0000	0.0000	0.0000	0.0000	0.0000	0.0000
O ₂	0.0000	0.0000	0.0000	0.0000	0.0000	0.0000	0.0000	0.0000	0.0000	0.0000	0.0000	0.0000
H ₂ O	0.0051	0.0008	0.0043	0.0043	0.0043	0.0043	0.0043	0.0043	0.2306	0.2306	0.5003	0.5003
CO ₂	0.7281	0.7586	0.7336	0.7336	0.7336	0.7336	0.7336	0.7336	0.0000	0.0000	0.0000	0.0000
CO	0.0821	0.0839	0.0825	0.0825	0.0825	0.0825	0.0825	0.0825	0.0000	0.0000	0.0000	0.0000
CH ₃ OH	0.0265	0.1523	0.0492	0.0492	0.0492	0.0492	0.0492	0.0492	0.7694	0.7694	0.4997	0.4997
H ₂	0.1582	0.0043	0.1304	0.1304	0.1304	0.1304	0.1304	0.1304	0.0000	0.0000	0.0000	0.0000
C	0.0000	0.0000	0.0000	0.0000	0.0000	0.0000	0.0000	0.0000	0.0000	0.0000	0.0000	0.0000

Continued...

Stream Number	49	50	51	52	53	54	55	56	57	58
Vapour Fraction	0	0	0	1	0	0	1	1	1	1
Temperature (°C)	67.5	40.0	97.8	102.2	112.2	40.0	25.0	45.5	150.0	200.0
Pressure (kPa)	113.3	103.3	140.0	116.5	163.0	162.4	101.3	121.3	101.3	101.3
Molar Flow (kmol/h)	2604	2604	4526	4526	2646	2646	12000	12000	12000	13680
Mass Flow (kg/h)	83350	83350	85610	85610	48040	48040	346200	346200	346200	370500
Mole Fraction										
CH ₄	0.0000	0.0000	0.0000	0.0000	0.0000	0.0000	0.0000	0.0000	0.0000	0.0000
C ₂ H ₆	0.0000	0.0000	0.0000	0.0000	0.0000	0.0000	0.0000	0.0000	0.0000	0.0000
C ₃ H ₈	0.0000	0.0000	0.0000	0.0000	0.0000	0.0000	0.0000	0.0000	0.0000	0.0000
n-C ₄ H ₁₀	0.0000	0.0000	0.0000	0.0000	0.0000	0.0000	0.0000	0.0000	0.0000	0.0000
n-C ₅ H ₁₂	0.0000	0.0000	0.0000	0.0000	0.0000	0.0000	0.0000	0.0000	0.0000	0.0000
n-C ₆ H ₁₄	0.0000	0.0000	0.0000	0.0000	0.0000	0.0000	0.0000	0.0000	0.0000	0.0000
N ₂	0.0000	0.0000	0.0000	0.0000	0.0000	0.0000	0.7900	0.7900	0.7900	0.6964
O ₂	0.0000	0.0000	0.0000	0.0000	0.0000	0.0000	0.2100	0.2100	0.2100	0.0054
H ₂ O	0.0027	0.0027	0.9358	0.9358	0.9901	0.9901	0.0000	0.0000	0.0000	0.2199
CO ₂	0.0000	0.0000	0.0000	0.0000	0.0000	0.0000	0.0000	0.0000	0.0000	0.0783
CO	0.0000	0.0000	0.0000	0.0000	0.0000	0.0000	0.0000	0.0000	0.0000	0.0000
CH ₃ OH	0.9973	0.9973	0.0642	0.0642	0.0099	0.0099	0.0000	0.0000	0.0000	0.0000
H ₂	0.0000	0.0000	0.0000	0.0000	0.0000	0.0000	0.0000	0.0000	0.0000	0.0000
C	0.0000	0.0000	0.0000	0.0000	0.0000	0.0000	0.0000	0.0000	0.0000	0.0000

Table 2. Utilities summary

Unit	E-102		E-103		E-104		E-106		E-111	
	In	Out	In	Out	In	Out	In	Out	In	Out
Utility	BFW-7	BFW-8	BFW-3	BFW-4	Cooling Water	Cooling Water	Cooling Water	Cooling Water	Cooling Air	Cooling Air
Vapour Fraction	0	0	0	0	0	0	0	0	0	0
Temperature (°C)	114.1	193.8	41.8	103.0	30.0	40.0	30.0	40.0	25.0	80.4
Pressure (kPa)	4047	4040	170.0	161.6	500	484	500	495	101.3	101.3
Molar Flow (kmol/h)	5505	5505	9355	9355	42350	42350	5513	5513	83189	83189
Mass Flow (kg/h)	99160	99160	168500	168500	763000	763000	99320	99320	2400330	2400330
Mole Fraction										
O ₂	0.0000	0.0000	0.0000	0.0000	0.0000	0.0000	0.0000	0.0000	0.2100	0.2100
N ₂	0.0000	0.0000	0.0000	0.0000	0.0000	0.0000	0.0000	0.0000	0.7900	0.7900
H ₂ O	1.0000	1.0000	1.0000	1.0000	1.0000	1.0000	1.0000	1.0000	0.0000	0.0000

Continued...

Unit	E-112		E-113		E-114		E-115		E-116	
	In	Out								
Utility	Cooling Water									
Vapour Fraction	0	0	0	0	0	0	1	1	0	0
Temperature (°C)	30.0	40.0	30.0	40.0	30.0	40.0	30.0	39.2	30.0	40.0
Pressure (kPa)	500	476	500	490	500	489	500	479.2	500	490
Molar Flow (kmol/h)	66560	66560	3399	3399	3078	3078	9465	9465	9182	9182
Mass Flow (kg/h)	1199000	1199000	61240	61240	55450	55450	170500	170500	165400	165400
Mole Fraction										
O ₂	0.0000	0.0000	0.0000	0.0000	0.0000	0.0000	0.0000	0.0000	0.0000	0.0000
N ₂	0.0000	0.0000	0.0000	0.0000	0.0000	0.0000	0.0000	0.0000	0.0000	0.0000
H ₂ O	1.0000	1.0000	1.0000	1.0000	1.0000	1.0000	1.0000	1.0000	1.0000	1.0000

Continued...

Unit	E-117		E-118		E-120		E-121		E-122	
	In	Out	In	Out	In	Out	In	Out	In	Out
Utility	Cooling Air	Cooling Air	Cooling Water	Cooling Water	Saturated Steam	Superheated Steam-1	Desuperheated Steam	Superheated Steam-2	Cooling Water	Cooling Water
Vapour Fraction	0	0	0	0	1	1	0.57	1	0	0
Temperature (°C)	25.0	53.9	30.0	40.0	253.0	500.0	252.7	500.0	30.0	40.0
Pressure (kPa)	101.3	101.3	500	498	4039	4019	4019	3999	500	458
Molar Flow (kmol/h)	251618	251618	18780	18780	5136	5136	9172	9172	487300	487300
Mass Flow (kg/h)	7171114	7171114	338300	338300	92520	92520	165200	165200	8778000	8778000
Mole Fraction										
O ₂	0.2100	0.2100	0.0000	0.0000	0.0000	0.0000	0.0000	0.0000	0.0000	0.0000
N ₂	0.7900	0.7900	0.0000	0.0000	0.0000	0.0000	0.0000	0.0000	0.0000	0.0000
H ₂ O	0.0000	0.0000	1.0000	1.0000	1.0000	1.0000	1.0000	1.0000	1.0000	1.0000

Continued...

Unit	E-123		P-101		P-102		P-103	
	In	Out	In	Out	In	Out	In	Out
Utility	BFW-8	BFW-9	BFW-1	BFW-2	BFW Makeup-1	BFW Makeup-2	BFW-5	BFW-6
Vapour Fraction	0	0	0	0	0	0	0	0
Temperature (°C)	193.8	253.0	42.1	42.1	25.0	25.0	113.6	114.1
Pressure (kPa)	4040	4039	8.1	170	101.3	170	161.6	4047
Molar Flow (kmol/h)	5505	5505	9172	9172	183.4	183.4	9541	9541
Mass Flow (kg/h)	99160	99160	165200	165200	3305	3305	171900	171900
Mole Fraction								
O ₂	0.0000	0.0000	0.0000	0.0000	0.0000	0.0000	0.0000	0.0000
N ₂	0.0000	0.0000	0.0000	0.0000	0.0000	0.0000	0.0000	0.0000
H ₂ O	1.0000	1.0000	1.0000	1.0000	1.0000	1.0000	1.0000	1.0000

Continued...

Unit	Steam System		MSR Shell		TU-100		TU-101	
	In	Out	In	Out	In	Out	In	Out
Utility	BFW Makeup-2	Blowdown	BFW-10	Saturated Steam	Superheated Steam-3	Exhaust-1	Superheated Steam-4	Exhaust-2
Vapour Fraction	0	0	0	1	1	0.96	1	0.97
Temperature (°C)	25.0	253	253	253	500.0	46.1	500	46.1
Pressure (kPa)	170	4039	4039	4039	3999	10	3999	10
Molar Flow (kmol/h)	183.4	183.4	5321	5321	4885	4885	4287	4287
Mass Flow (kg/h)	3305	3305	95860	95860	88000	88000	77230	77230
Mole Fraction								
O ₂	0.0000	0.0000	0.0000	0.0000	0.0000	0.0000	0.0000	0.0000
N ₂	0.0000	0.0000	0.0000	0.0000	0.0000	0.0000	0.0000	0.0000
H ₂ O	1.0000	1.0000	1.0000	1.0000	1.0000	1.0000	1.0000	1.0000

Chapter 3. Process Modelling and Simulation

3.1 Pyrolysis Reactor (PR)

The PR consists of several vertical tubes filled with molten $\text{Cu}_{0.45}\text{Bi}_{0.55}$ alloy and externally heated by burners in the radiant zone of the fired heater as shown in Figure 14. Pre-heated natural gas is injected at the bottom of the tubes and is progressively converted to hydrogen and carbon as it rises in the form of bubbles through the molten metal. The produced carbon floats to the surface of the melt. The molten metal is covered by a layer of molten salt (e.g., NaBr), whose purpose is to reduce metal losses and carbon contamination by the metal (Rahimi et al, 2019). To facilitate carbon removal, the tops of the tubes connect to a production manifold where the carbon layer is continuously removed by mechanical skimming or other practical means (Catalan and Rezaei, 2021). The mixture of hydrogen and unreacted natural gas exits the upper part of the production manifold and is routed out of the fired heater toward the rest of the process.

The hydrodynamics and kinetics of natural gas pyrolysis in molten $\text{Cu}_{0.45}\text{Bi}_{0.55}$ were modelled using the methods described in detail in Catalan and Rezaei (2022). The model consists of a system of coupled differential equations, and is numerically implemented in MATLAB™. The coupled differential equations relate the material balance (Equation 21) and the pressure change (Equation 22):

$$\dot{n}_{CH_4,b} dX_{CH_4} = (R_c + R_n) \alpha \frac{\pi D^2}{4} dL \quad (21)$$

Where:

$\dot{n}_{CH_4,b}$ - Molar flow of methane at the tube inlet (mol/s)

R_c – Catalytic reaction rate (mol $\text{CH}_4/\text{m}^3_{\text{gas}}\cdot\text{s}$)

R_n – Non-catalytic reaction rate (mol $\text{CH}_4/\text{m}^3_{\text{gas}}\cdot\text{s}$)

L – Reactor length (m)

$$dP = -[\rho_l(1 - \alpha) + \rho_g\alpha]gdL \quad (22)$$

Where:

P – Pressure (Pa)

ρ_l – Density of the molten metal (kg/m³)

ρ_g – Density of the gas (kg/m³)

α – gas hold up

g – gravitational acceleration (m/s²)

R_c and R_n indicate that the model accounts for both the catalytic and non-catalytic methane pyrolysis reactions at the gas/liquid interface and inside the bubbles, respectively. These values are a function of the specific interfacial area of the gas bubbles and the reactor gas hold up, which are determined based on the feed superficial gas velocity, tube diameter and physical properties of the melt using correlations available in the literature (Akita & Yoshida, 1974; Hibiki et al., 2000; Kataoka & Ishii, 1987)

The inputs to the model are the natural gas composition and molar flow rate, the reactor temperature (considered isothermal), the diameter of the tubes, and the desired methane conversion. The model determines the number of tubes, tube length, and inlet pressure that minimize the total volume of molten metal in the reactor and, therefore, its cost. The volume of the melt is given by Equation (23):

$$V_{melt} = \frac{N_t \pi D^2 L_t}{4} \quad (23)$$

Where:

V_{melt} – Volume of catalytic molten metal (m³)

N_t – Number of tubes

D – Tube diameter (m)

L_t – Tube length (m)

The total feed flow rate of methane is related to the total flowrate of product hydrogen by Equation (24) based on the fact that for each mole of methane that is pyrolyzed, 2 moles of hydrogen are produced.

$$\dot{n}_{CH_4(total)} = \frac{\dot{n}_{H_2(total)}}{2X_{CH_4,t}} \quad (24)$$

Where:

$\dot{n}_{CH_4(total)}$ - Total molar flow of methane (mol/s)

$\dot{n}_{H_2(total)}$ - Total molar flow of hydrogen (mol/s)

$X_{CH_4,t}$ - Methane conversion at the top of the reactor

The number of tubes N_t is a function of the total molar flow rate of methane and the molar flow of methane to each tube as shown in Equation (25):

$$N_t = \frac{\dot{n}_{CH_4(total)}}{\dot{n}_{CH_4,b}} \quad (25)$$

Combination of Equations (23)-(25) yields Equation (26) which is the objective function that MATLAB™ solves to minimize the volume of molten metal.

$$V_{melt} = \frac{\dot{n}_{H_2(total)}\pi D^2 L_t}{8\dot{n}_{CH_4,b}X_{CH_4,t}} \quad (26)$$

For the purpose of carrying out mass and energy balances on the entire process, the PR was simulated in Aspen Hysys™ as an isothermal conversion reactor with operating conditions (temperature, pressures, inlet flow rate, and conversion) equal to those of the MATLAB™ model used to size the reactor.

The fractional methane conversion in the PR is defined as:

$$X_{CH_4,PR} = \frac{\dot{n}_{CH_4,in} - \dot{n}_{CH_4,out}}{\dot{n}_{CH_4,in}} \quad (27)$$

where $\dot{n}_{CH_4,in}$ and $\dot{n}_{CH_4,out}$ are the molar flow rates of methane entering and leaving the PR, respectively. Because the process produces a constant methanol flowrate of 2000 t/d, the hydrogen flowrate exiting the PSA unit and entering the MSR section is constant and independent of $X_{CH_4,PR}$. Inside the radiant zone of the fired heater, heat must flow from the flue gas to the pyrolysis reactor tubes throughout the entire tube length. To this effect, the temperature of the flue gas exiting the radiant zone was set to 1130°C, which is significantly higher than the melt temperature of 1100°C. Because the PSA purge stream is the main source of fuel for the fired heater, both its flow rate and its composition affect the flue gas temperature exiting the radiant zone. Details on the selection of $X_{CH_4,PR}$ are provided in Section 4.2.

The PR design parameters are presented in Table 3. The reactor consists of 16,513 tubes having 10-cm internal diameter, 4-cm wall thickness, and 0.76-m length. This results in a total volume of liquid $Cu_{0.45}Bi_{0.55}$ alloy equal to 98 m³. The tube material of construction is a Ni-Cr alloy with the specifications of the Manaurite XMR. The inlet and outlet pressures are 1901 and 1837 kPa, respectively. The inlet mass flow rate of natural gas is 2315 t/d. Figure 15 shows the methane conversion and gas hold up profiles along the length of a single tube in the reactor.

Table 3. Design parameters of the pyrolysis reactor used in this study for a 2000 t/d methanol plant.

Parameter	Value
Methane conversion (%)	80
Temperature (°C)	1100
Tube inner diameter (m)	0.10
Tube material of construction	Heat resistant austenitic alloy (Manaurite XM)
Tube wall thickness (m)	0.043
Tube length (m) ^(a)	0.755
Number of tubes	16,513
Molten volume of Cu _{0.45} Bi _{0.55} catalyst (m ³) ^(b)	98.0
Inlet pressure (kPa)	1901
Outlet pressure (kPa) ^(c)	1837
Bottom gas holdup	0.121
Top gas holdup	0.133
Reactor duty (MW)	146.9
Average heat flux (kW/m ²) ^(d)	29.4
Molten salt (NaBr) layer thickness (m)	0.24

^(a) Molten metal length only. The bottom of the molten salt layer is assumed to be located at the junction between top end of the tubes and the production manifold (Figure 14).

^(b) Includes the gas holdup. The liquid Cu_{0.45}Bi_{0.55} volume excluding the gas holdup is 85.6 m³.

^(c) Does not account for the pressure drop in the molten salt layer (approx. 7 kPa).

^(d) Based on the inner tube surface area.

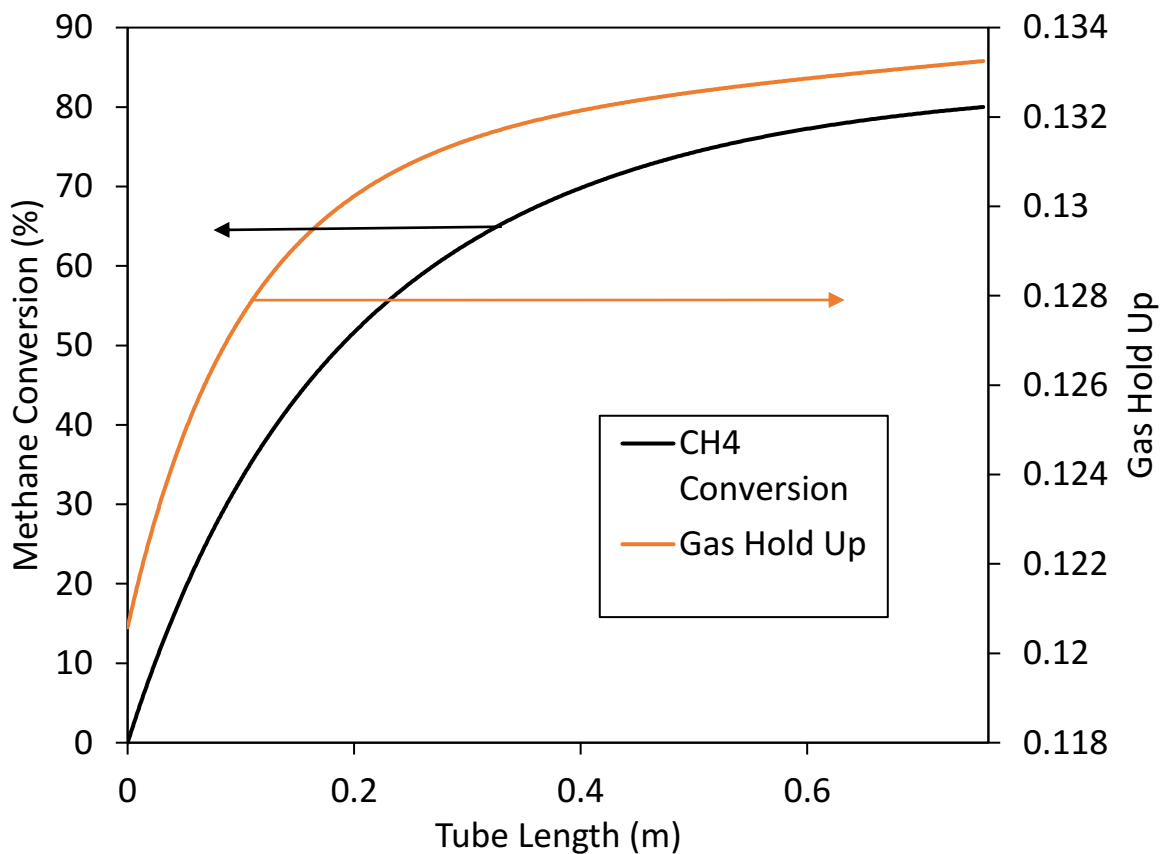


Figure 15. Pyrolysis reactor methane conversion and gas hold up profiles along the length of a single PR tube. Dimensions and operating conditions are those found in Table 1.

The Manaurite XM (*Manaurite XMR - Heat Resistant Alloys for Hydrocarbon Processing, 2012*) is selected as the tube material of construction because of the high operating temperature of the PR. Higher temperatures result in smaller reactor volumes due to faster methane pyrolysis kinetics. These high temperatures require special design considerations and as a result the tubes of the pyrolysis reactor should be made of heat-resistant alloys with very high creep strength at high temperature combined with good oxidation and carburization resistance. The Manaurite XM is an example of a commercial austenitic alloy used for tubes in the radiant section of reforming furnaces and contains approximately 35% Ni and 25% Cr. The required tube wall thickness is estimated from 100,000-hour creep rupture stress data versus temperature shown in Figure 16. The minimum stress, which represents the 95% confidence

level, provides a more conservative design than the average stress and is therefore used in the calculation.

The tube thickness, t (m), is related to the pressure both inside and outside the tubes, P_i (MPa) and P_o (MPa), as well as the tube internal diameter, D_i (m), and the hoop stress, σ_h (MPa), by:

$$t = \frac{(P_i - P_o)D_i}{2(\sigma_h - P_i + P_o)} \quad (28)$$

Figure 16 indicates that at 1100°C the minimum σ_h is 3.9 MPa. The maximum pressure inside the tubes occurs at the tube entrance and is equal to $P_i = 1.9$ MPa. The pressure outside the tubes is close to atmospheric ($P_o = 0.10$ MPa). For an internal tube diameter of $D_i = 0.10$ m, Equation (28) gives $t = 0.043$ m.

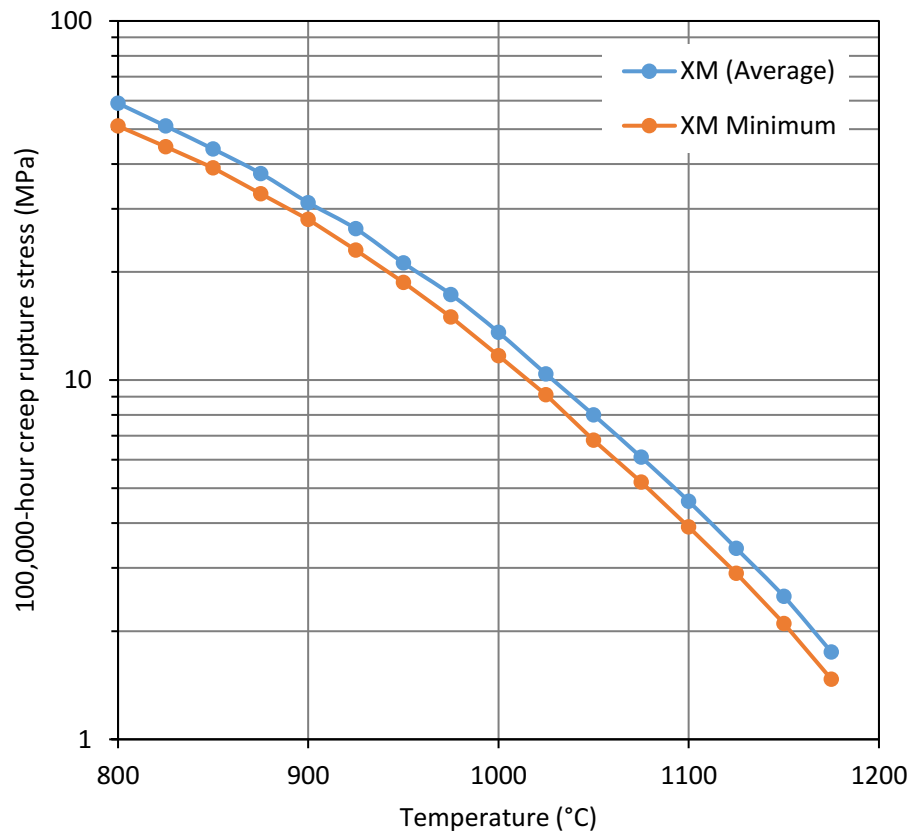


Figure 16. 100,000-h creep rupture stress versus temperature for Manaurite XM.

3.2 Methanol Synthesis Reactor (MSR)

3.2.1 Kinetics & Model Validation

The MSR is simulated as a multi-tubular plug flow reactor in Hysys™. The tubes are filled with commercial Cu/ZnO/Al₂O₃ catalyst, and the shell contains BFW that boils to produce saturated steam while removing the heat produced by the exothermic methanol synthesis reaction. The kinetics of the methanol synthesis and water gas shift reactions are validated and modelled with the equations of Vanden Bussche & Froment, (1996). The validation is shown in Figures 17 & 18 where the simulated results closely match the experimental ones.

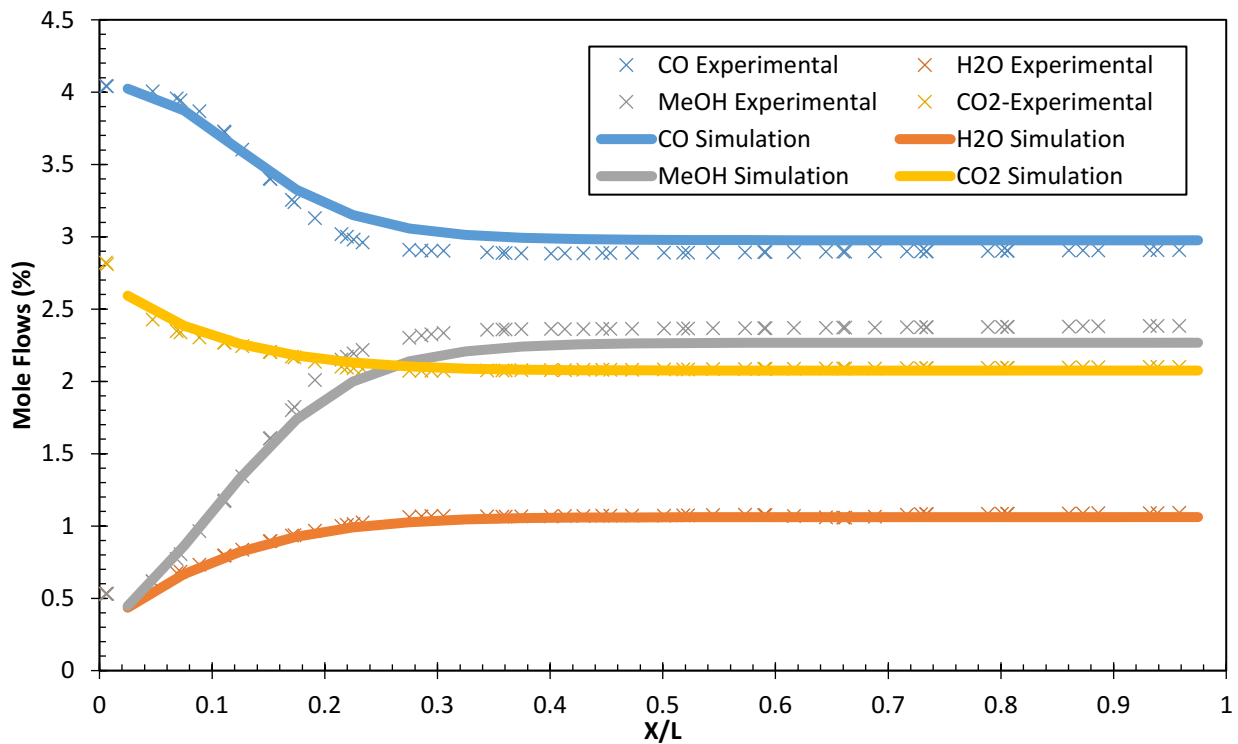


Figure 17. Experimental and Aspen Hysys™ simulated mole flows along MSR length using the Vanden Bussche & Froment (1996) kinetic model.

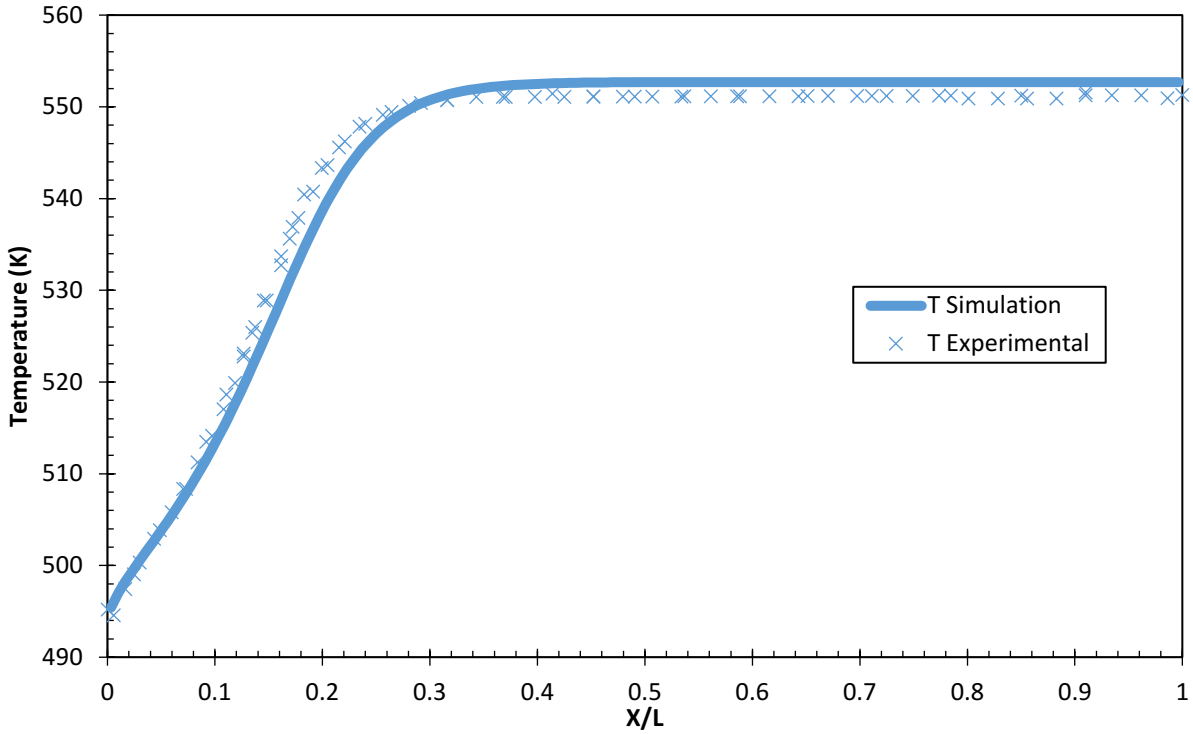


Figure 18. MSR reactor temperature profile simulated in Aspen HysysTM using the Vanden Bussche and Froment (1996) kinetic model.

3.2.2 Modelling and Optimal Operating Conditions Selection

The flowrate of captured CO₂ fed to the process is adjusted so that the H₂/CO₂ molar ratio in the MSR feed is 3.00 matching the stoichiometry of Equation (2) and which corresponds to a stoichiometric number $SN = (H_2 - CO_2)/(CO + CO_2)$ equal to 1.85. The 3:1 H₂:CO ratio is important to ensure the reactor does not become starved in either reactant. If this were to happen, there would be a large recycle flow rate of the other component in the loop, resulting in large compressor duties and unit sizes.

The reactor temperature, pressure and process fluid temperature are optimized to maximize the single pass carbon conversion to methanol defined as:

$$X_{C,MSR} = \frac{\dot{n}_{MeOH,out} - \dot{n}_{MeOH,in}}{\dot{n}_{CO_2,in} + \dot{n}_{CO,in}} \quad (29)$$

where $\dot{n}_{MeOH,out}$ is the outlet mole flow rate of methanol, while $\dot{n}_{CO_2,in}$, $\dot{n}_{CO,in}$ and $\dot{n}_{MeOH,in}$ are the inlet mole flow rates of carbon dioxide, carbon monoxide and methanol, respectively.

Figure 19 shows the results of the single pass carbon conversion in an isothermal, isobaric MSR with a reactor volume of 300 m³. The results indicate that the optimum inlet pressure and temperature are 8000 kPa and 255 °C, resulting in a single pass carbon conversion of 21.72%. The high inlet pressure is beneficial in this reaction because high pressures have a positive effect on the methanol synthesis reaction rate, and they shift the reaction equilibrium towards the product side since the reaction decreases the total number of gas moles (Equation 2). The figure also shows that at a reactor inlet temperature of 255°C, the benefit of increasing the inlet pressure on the single pass carbon conversion decreases as the pressures get higher. Higher operating pressures are accompanied by higher operating costs due to compression and process unit materials of construction, so there is no substantial benefit to increasing the inlet pressure beyond 8000 kPa.

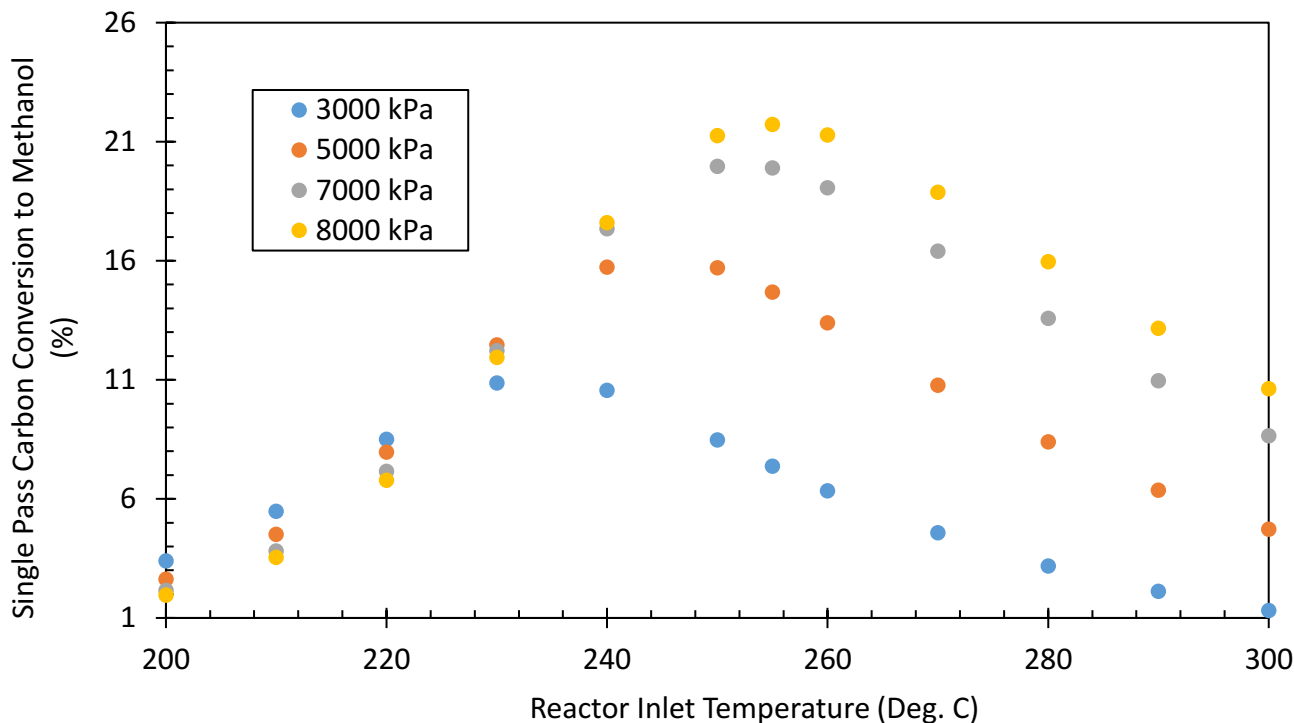


Figure 19. Methanol synthesis reactor inlet temperature and pressure selection with constant reactor volume (300 m³), inlet flow rate and feed composition under isothermal and isobaric conditions.

Figure 20 shows the methanol synthesis reactor volume selection under isothermal and isobaric conditions with constant reactor inlet flowrate, composition, temperature, and pressure. A volume of 300 m³ is selected as the single pass carbon conversion does not substantially increase beyond this point due to the reactor approaching equilibrium.

In practice, the temperature profile of the process fluid in the tubes varies along the reactor length due to heat transfer limitations (Figure 21), and the temperature of boiling water in the

shell is selected to minimize the variations of the process fluid temperature around its optimum value.

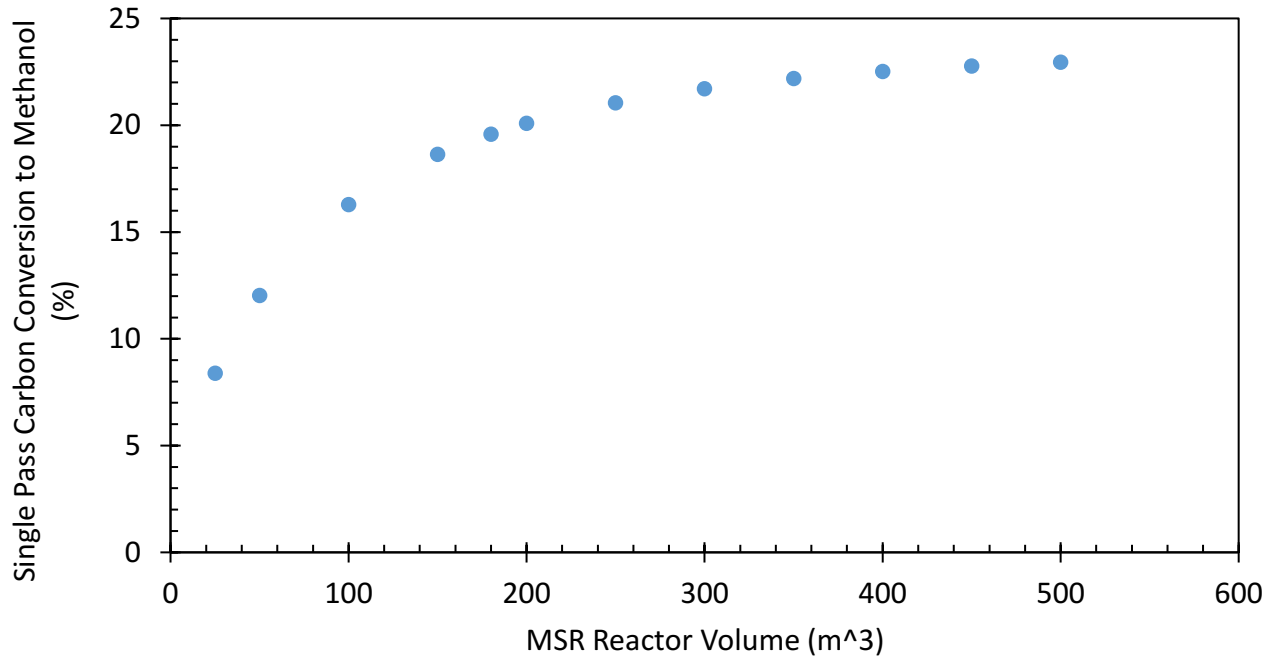


Figure 20. Methanol synthesis reactor volume selection under isothermal and isobaric conditions with constant reactor inlet flowrate, composition, temperature (255 °C) and pressure (8000 kPa).

3.2.3 Heat Transfer

Heat transfer between the shell and tube sides of the reactor was modelled in HysysTM. The heat transfer coefficient inside the tubes was determined to be 910.11 W/m²-K using the correlations of Peters et al (Peters et al., 1988a) who experimentally investigated radial heat transfer in reactors packed with alumina spheres, cylinders and rings.

From Peters et al., (1988) the effective thermal conductivity is estimated using Equation (30):

$$\frac{k_e}{k_f} = \frac{k_e^0}{k_f} + \frac{Re_p Pr_f}{Pe_m} \quad (30)$$

Where:

k_e – Effective thermal conductivity (W/m.K)

k_f – Fluid thermal conductivity (W/m.K)

k_e^0 – Effective thermal conductivity at zero fluid flow (W/m.K)

Re_p – Particle Reynolds number

Pr_f – Fluid Prandtl number

Pe_m – Peclet number for radial mass transfer

The Reynolds number and Prandtl numbers used in Equation (30) are estimated as follows:

$$Re_p = \frac{D_p G}{\mu} \quad (31)$$

$$Pr_f = \frac{Cp * \mu}{k_f} \quad (32)$$

Where:

D_p – Particle diameter (m)

G – Gas mass flux (kg/m².s)

μ – Dynamic viscosity (kg/m.s)

Cp – Fluid heat capacity (J/kg.K)

The gas mass flux is calculated by dividing the inlet gas mass flowrate to a single MSR shell by the total cross-sectional area of tubes in that shell.

$$A_C = \pi r_i^2 \frac{N_T}{N_S} = \pi * 0.0191^2 * \frac{19637}{3} = 7.46 \text{ m}^2 \quad (33)$$

Where:

r_i – Tube inner radius (m)

N_T – Total number of tubes

N_S – Number of MSR shells

$$G = \frac{53.9 \frac{\text{kg}}{\text{s}}}{7.46 \text{ m}^2} = 7.23 \frac{\text{kg}}{\text{m}^2 \cdot \text{s}} \quad (34)$$

Because the MSR catalyst pellets are cylindrical, the equivalent radius of a sphere that would have the same volume as the catalyst is calculated. The radius and length of the catalyst particles are taken from (*MK-121 | Catalysts | Products | Haldor Topsoe, n.d.*):

$$r_e = \left(\frac{3 * r_p^2 * L_p}{4} \right)^{\frac{1}{3}} \quad (35)$$

Where:

r_e – equivalent radius (m)

r_p – particle radius (m)

L_p – particle length (m)

$$r_e = \left(\frac{3 * \left(\frac{0.006}{2} \right)^2 * 0.004}{4} \right)^{\frac{1}{3}} = 3.00 \times 10^{-3} \text{ m}$$

Now the Reynolds number and Prandtl numbers are calculated using the equivalent particle diameter. Values for the fluid viscosity, thermal conductivity & heat capacity are taken from Aspen Hysys™.

$$Re_p = \frac{0.006 * 7.23}{1.832 \times 10^{-5}} = 2367$$

$$Pr_f = \frac{2602 * 1.832 \times 10^{-5}}{0.1537} = 0.310$$

The Peclet number is calculated using the correlation provided in Peters et al., (1988, pg. 226):

$$Pe_m = 6.3 + 34.7 \left(\frac{D_p}{D_i} \right) \quad (36)$$

$$Pe_m = 6.3 + 34.7 \left(\frac{0.006}{0.0381} \right) = 11.8$$

Where:

D_i – Tube inner diameter (m)

Peters et al., (1988, pg. 230) suggests that the value of k_e^0/k_f is in the range of 3-7 for typical porous catalysts at moderate temperature. They also state that the effective thermal conductivity k_e is not sensitive to the value of k_e^0/k_f at the high Reynolds number used in their experiment. Because the Reynolds number in this project is within the range of Reynolds numbers used in the experiment, it is taken to be “high” and a value of k_e^0/k_f of 5 is assumed. k_e is then calculated using Equation (30):

$$k_e = \left(5 + \frac{2367 * 0.310}{11.8} \right) * 0.1537 = 10.36 \text{ W/(m.K)}$$

The bed heat transfer coefficient is calculated according to Peters et al., (1988, pg. 227) where β is a dimensionless parameter accounting for the temperature dependence of the bed heat transfer coefficient. Assuming the reaction rate is approximately constant in the radial direction and the temperature is not a strong function of the axial position, the value of β is 4 (Peters et al., 1988, pg. 227).

$$h_{bed} = \beta \left(\frac{k_e}{r_i} \right) \quad (31)$$

Where:

h_{bed} – bed heat transfer coefficient (W/m².K)

β – Dimensionless parameter accounting for the temperature dependence of h_{bed}

$$h_{bed} = 4 \left(\frac{10.36}{0.0191} \right) = 2174.92 \frac{W}{m^2.K}$$

The wall heat transfer coefficient is calculated using the correlation provided by Peters et al., (1988, pg. 232) for a variable Pe_m approach:

$$\frac{h_w D_p}{k_f} = 3.8 \left(\frac{D_p}{D_t} \right)^{0.39} Re_p^{0.5} Pr_f^{0.33} \quad (32)$$

Where:

h_w – Wall heat transfer coefficient (W/m².K)

$$h_w = \frac{3.8 * \left(\frac{0.006}{0.0381} \right)^{0.39} * 2367^{0.5} * 0.310^{0.33} * 0.1537}{0.006} = 1564.98 \frac{W}{m^2.K}$$

The overall tube-side heat transfer coefficient is calculated by:

$$\frac{1}{h_0} = \frac{1}{h_{bed}} + \frac{1}{h_w} \quad (33)$$

Where:

h_0 – Overall tube- side heat transfer coefficient (W/m².K)

$$h_0 = \frac{1}{\frac{1}{2174.92} + \frac{1}{1564.98}} = 910.11 \frac{W}{m^2.K}$$

The shell side heat transfer coefficient is estimated as $1100 \text{ W/m}^2\cdot\text{K}$ due to the low resistance associated with the evaporation of saturated boiler feed water. When the shell temperature is constant at 253°C (due to the boiling of BFW), the process fluid temperature varies between 248.6°C and 261.7°C (Figure 21).

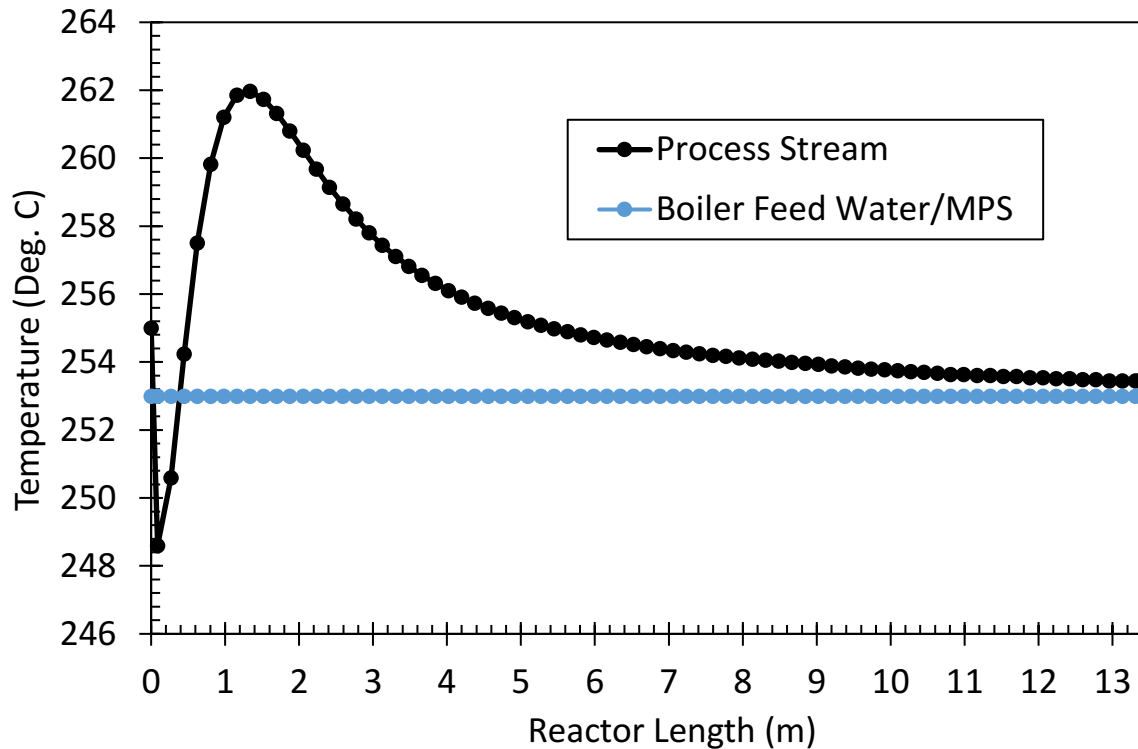


Figure 21. Temperature profiles of the process fluid (tubes) and the saturated steam (shell).

The molar flow profiles along the MSR tube length (Figure 22) provide insights on the causes of temperature variations of the process stream shown in Figure 21. In the first 0.09 m of reactor, CO and H₂O are produced by the endothermic reverse water gas shift reaction causing a sharp decrease in process fluid temperature from 255°C to 248.6°C near the reactor entrance. The kinetic model of Vanden Bussche & Froment assumes that methanol is exclusively produced by the hydrogenation of CO₂, whereas CO only reacts through the water gas shift reaction. Therefore, the decrease in CO after reaching a maximum at 0.63 m corresponds to its conversion back to CO₂ by water gas shift. Because the water gas shift and the CO₂

hydrogenation reactions are both exothermic, the process fluid temperature rises and reaches 262.0°C at 1.5 m. This occurs at the position where the rate of heat production by the reactions matches the rate of heat transfer to the shell. As the process fluid flows further along the tubes, its temperature decreases because the reactions slow down as they approach equilibrium.

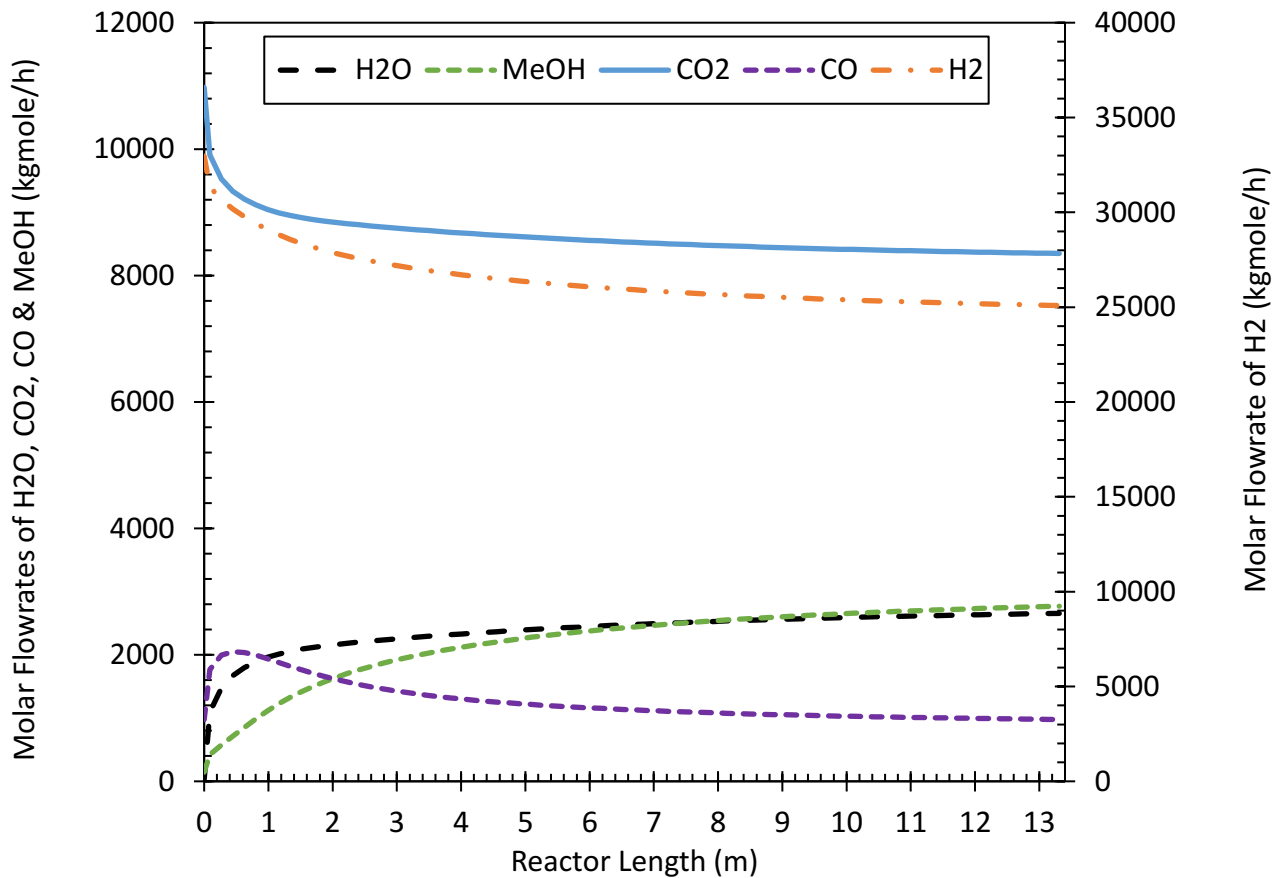


Figure 22. Molar flow profiles along the tubes of the MSR.

For a given carbon conversion and operating conditions, the use of CO₂ as the main carbon source in the MSR feed requires a catalyst volume several times larger than if CO was the main source of carbon, as in traditional processes based on steam methane reforming. This explains the large MSR dimensions and is due to the adsorption of water on the catalyst, which decreases catalyst activity (Vanden Bussche & Froment, 1996). Because the reaction of CO₂ with H₂ to produce methanol also generates one mole of H₂O per mole of reacted CO₂, the molar flow rate of water increases progressively along the reactor length (Figure 22). In

contrast, when the feed contains a large CO concentration, each molecule of CO must first be converted to CO₂ by water gas shift, which consumes one mole of H₂O. Hence, the concentration of water is kept at very low levels, which limits its adsorption on catalyst active sites.

3.2.4 Shell Diameter

The MSR shell diameter is estimated using the equation presented by Smith, (2016) for determining the shell diameter of a shell and tube heat exchanger:

$$D_S = \left(\frac{4 * F_{TC} F_{SC} P_C P_T^2 A}{\pi d_o L} \right)^{0.5} \quad (34)$$

Where:

D_S – Shell diameter (m)

F_{TC} – Tube count constant (1.08 for single tube pass configuration (Smith, 2016, pg. 293))

F_{SC} – Correction factor for shell construction (1.15 for floating head (Smith, 2016, pg. 293))

P_C – pitch configuration factor (0.866 for triangular pitch (Smith, 2016, pg. 293))

P_T – tube pitch (m)

A – Heat transfer area (m²)

d_o – Tube outside diameter (m)

L – Tube length (m)

When applied to the total number of tubes ($N_T = 19,638$), Equation (34) gives $D_S = 9.2$ m, which is very large. A more practical alternative is to distribute the tubes equally in several parallel shells. Using 4 shells decreases the value of D_S to 4.9 m, which is consistent with reports of typical shell diameters between 4.5 and 5.5 m for multitubular methanol synthesis reactors (Rahmatmand et al., 2018).

The final reactor design contains 19,637 tubes measuring 13.4 m in length, 3.81 cm (1.5 inch) in internal diameter, and 0.5 cm in wall thickness for a total catalyst volume of 300 m³. The

catalyst void fraction (void volume / total volume) is calculated to be 0.325. The pressure drop is estimated to be 164 kPa by the Ergun equation:

$$\frac{\Delta P \rho_f}{G_o^2} * \frac{D_p}{L} * \frac{\varepsilon^3}{1 - \varepsilon} = 150 * \frac{1 - \varepsilon}{D_p * \frac{G_o}{\mu}} + 1.75 \quad (35)$$

Where:

ΔP – Pressure drop (kPa)

G_o – Gas mass velocity (m/s)

ε – Bed void fraction

3.3 Fireside of the Fired Heater

The burners on the walls of the radiant zone of the fired heater are modelled in Aspen Hysys™ as an adiabatic conversion reactor where all the methane, hydrogen, carbon monoxide, and methanol contained in the incoming fuel are combusted with air. Excess air is fixed at 3% to ensure complete combustion. The hot combustion products enter a one-sided heat exchanger simulating the radiant zone of the fired heater where the pyrolysis reactor tubes are located. The duty of this exchanger (151.4 MW) accounts for the heating of the natural gas feed from 800 to 1100°C in the PR, the endothermic heats of the methane and C₂₊ pyrolysis reactions, and an estimated 3% heat loss through the walls of the radiant zone. The flue gas leaves the radiant zone at a temperature of 1130°C, which allows for heat flow from the flue gas to the molten metal at 1100°C inside the tubes.

The flue gas exiting the radiant zone enters the convection zone simulated in Aspen Hysys™ by five heat exchangers in series (Figure 14). The first heat exchanger (E-120) generates superheated steam from saturated steam supplied by the MSR steam drum. To produce more superheated steam, the superheated steam leaving E-120 is first desuperheated by mixing with quench BFW and then superheated again in E-121. The superheated steam temperature of

500°C is suitable for entering the turbines TU-100 and TU-101 (Smith, 2016). The third heat exchanger (E-107) preheats the MSR feed to 255°C. The fourth heat exchanger (E-123) preheats BFW to 253°C prior to entering the MSR boiler. Finally, the fifth heat exchanger (E-119) preheats the combustion air to 150°C. The flow rate of the quench BFW, which controls the amount of superheated steam generated in E-121, is adjusted so that the flue gas exiting the last heat exchanger in the convective zone (E-119) is at a temperature of 200°C. The flue gas outlet temperature (FGOT) should be maintained at least 20°C above the acid dewpoint to prevent corrosion of heat exchange surfaces (American Petroleum Institute, 2016). The simplified natural gas composition assumed in this study is free of sulphur compounds but actual natural gases often contain sulphur concentrations of approximately 5 ppm to 5000 ppm, and their sulphuric acid dewpoint temperatures range from 90 °C to 150 °C at typical excess air concentrations (American Petroleum Institute, 2016). Consequently, the FGOT is set conservatively at 200°C in this study by adjusting the quench BFW flow rate and the amount of superheated steam produced.

3.4 Plate and Shell-and-Tube Heat Exchangers

The plate heat exchangers for cooling the solid carbon produced in the PR (E-105 and E-106 in Figure 12) are based on a design by Solex Thermal Science (Calgary, Canada)(*Cooling Heat Exchanger - Cool Bulk Solids Without Air | Solex - Solex*, n.d.). These heat exchangers are capable of cooling up to 100 000 kg/h of bulk solids from temperatures as high as 2000 °C. The bulk solids flow by gravity between multiple vertical plates. The gas or liquid to be heated flows inside the vertical plates. A schematic of the plate heat exchanger is shown in Figure 23 and was taken directly from the Solex website.

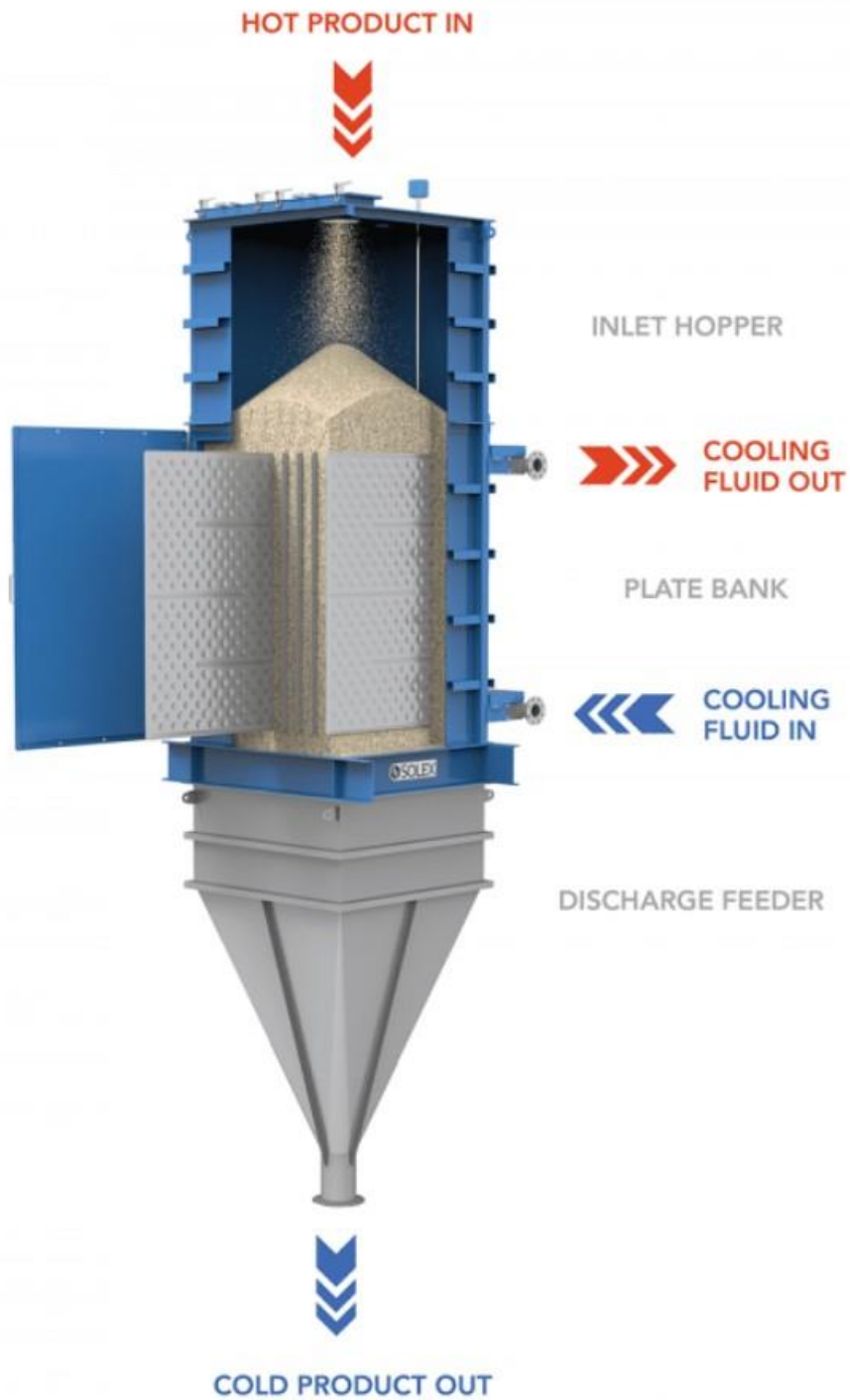


Figure 23. Schematic of Solex plate heat exchanger for cooling solid particles (*Cooling Heat Exchanger - Cool Bulk Solids Without Air | Solex - Solex, n.d.*).

The temperature and flow rate of solid carbon in the CP-LMBR process (1100 °C and 57,400 kg/h) are well within the operating range of the Solex heat exchangers. The plate heat exchangers are simulated in Aspen Hysys™ with a simple endpoint model to calculate their heat balance.

The condenser of the distillation tower T-102 (E-117) and the partial condenser (E-111) upstream of the high-pressure flash tank V-101 are designed as air cooled heat exchangers using Aspen Exchanger Design and Rating (EDR) to determine their heat balance, geometry, pressure drops, heat exchange area, number of fans, and fan power.

The other heat exchangers (excluding the fired heater) are designed as shell-and-tube exchangers with Aspen Exchanger Design and Rating (EDR) to calculate their heat balance, geometry, pressure drops, and tube surface area. Specific data on heat exchanger type, shell pressure, tube pressure, material of construction, and heat exchanger area for each heat exchanger are shown in Table 11 at the end of Section 5.1.

3.5 Flash Tanks and Distillation Columns

Liquid-vapour equilibrium calculations for flash tanks and distillation towers rely on the NRTL activity model for liquids and on the Redlich-Kwong equation of state for vapours. The interaction parameters for the pairs methanol/CO₂, methanol/H₂O, methanol/H₂, H₂O/CO₂, and H₂O/H₂ were regressed using experimental data from the ThermoData Engine of Aspen Plus and imported into Aspen Hysys™.

Liquid vapour separators V-101 and V-102 are designed as vertical cylindrical vessels with mesh de-entrainers using the following constraints (Couper, J.R., Penney, W.R., Fair, J.R., Walas, 2012): 1) the gas velocity in the upper part of the vessel, v_g , should be less than the maximum gas velocity given by Equation (36), where ρ_L and ρ_V are the liquid and vapour densities, respectively; 2) the liquid holdup time in a half full vessel should be between 5 and 10 minutes; and 3) the length to diameter ratio should be in the range 2.5 – 5.0. Specific heights, diameters, materials of construction, and pressures of V-101 and V-102 are shown in Table 11 at the end of Section 5.1.

$$v_{g,max} = 0.080 \sqrt{\frac{\rho_L}{\rho_V} - 1} \quad (36)$$

For the case where the calculated L/D ratio for the minimum required diameter is less than 2.5, the length is set to 2.5 times the diameter. For the case where the L/D ratio is greater than 5, the L/D is set to 3 by adjusting the vessel length. The vessel diameter is set to ensure a liquid holdup time of 5 minutes for a half full vessel.

Distillation towers are designed as rigorous columns in Aspen Hysys™ to determine their number of plates, reflux ratio, and diameter to meet purity requirements and avoid flooding or weeping. Tray efficiencies are estimated using the Lockhart and Leggett version of the O'Connell correlation (Seader, J.D., Henley, E.J., Roper, 2016):

$$E^0 = 0.492 \left(\alpha_{LK/HK,average} * \mu_{L,average} \right)^{-0.245} * 100 \quad (37)$$

Where:

E^0 – Tray efficiency (%)

$\alpha_{LK/HK, average}$ – The average partitioning coefficient ratio between the light and heavy keys on the top and bottom trays

$\mu_{L, average}$ – The average liquid viscosity between the top and bottom trays (cP)

$$\alpha_{LK/HK} = \frac{K_{LK}}{K_{HK}} \quad (38)$$

Where:

$\alpha_{LK/HK}$ – Ratio of partitioning coefficients

K_{LK} – Light key partitioning coefficient

K_{HK} – Heavy key partitioning coefficient

The average of $\alpha_{LK/HK}$ and μ_L used are the geometric averages, calculated by the following equation with $\alpha_{LK/HK}$ used as an example:

$$\alpha_{LK/HK}^{average} = \left(\alpha_{LK/HK}^{Top\ Tray} * \alpha_{LK/HK}^{Bottom\ Tray} \right)^{0.5} \quad (39)$$

The K and μ values are taken from the Aspen Hysys™ simulation where the light key is methanol and the heavy key is water. Table 4 provides the data for tower T-102.

Table 4. Distillation tower T-102 sizing information.

	K_{MeOH}	K_{H2O}	$\alpha_{MeOH/H2O}$	Geometric Average α	Liquid Viscosity (cP)	Geometric average liquid viscosity (cP)	Efficiency (%)
Top Tray	1.002	0.4244	1.580	3.984	0.3356	0.2873	47.60
Bottom Tray	6.361	0.9463	6.722		0.2460		

With a diameter of 5.0 m, the H/D for the column is less than 30 and the tower height is less than the maximum recommended height (53.34 m) from Walas, (1990).

Specific column dimensions as well as numbers and types of trays for the towers T-101 and T-102 are presented in Table 11 at the end of Section 5.1.

3.6 Pressure Swing Adsorber

The PSA is simulated as a component splitter in Aspen Hysys™ where 88.25% of the hydrogen in the PSA feed reports to the pure H₂ stream exiting the PSA. The rest of the feed leaves through the PSA purge stream consisting of 44.2 mol% CH₄, 49.1 mol% H₂, 4.8 mol% CO₂, and 2 mol% N₂. The PSA purge accounts for 95.5 mol% of the fuel used in the fired heater.

3.7 Compressors, Blowers, Turbines, and Expanders

All compressors are of centrifugal type and their polytropic efficiency, η_P , is estimated by (Smith, 2016):

$$\eta_P = 0.017 \ln F + 0.70 \quad (40)$$

where F is the volumetric flowrate (m^3/s) of the inlet gas. The overall compressor efficiency is the product of η_P with the mechanical efficiency, η_M . The mechanical efficiency is assumed to be 0.98 (Smith, 2016). The results for all compressors in the process are presented in Table 5.

Table 5. Compressor efficiencies.

Compressor	Adiabatic Efficiency (%)
K-101	71.03
K-102	69.48
K-103	71.01
K-104	69.23
K-105	67.03
K-106	65.18

The polytropic efficiency of the centrifugal blower for combustion air was estimated to be 77%, which is the midpoint of the range 69 – 85% provided by Guernsey et al (Guernsey, M., Chung & Goetzler, 2015). All centrifugal pumps were assumed to have 75% adiabatic efficiency.

The isentropic efficiency of steam turbines at maximum load is given by (Smith, 2016):

$$\eta_{A,max} = \frac{1}{a} \left(1 - \frac{b}{m_{max} \Delta H_{IS}} \right) \quad (41)$$

where m_{max} is the steam mass flowrate at maximum load (kg/s) and ΔH_{IS} is the enthalpy change of steam for an isentropic expansion (kJ/kg). The value of ΔH_{IS} is determined by simulating an isentropic turbine (100% isentropic efficiency) in Aspen Hysys™ using the same steam mass flow rate, inlet pressure, and outlet pressure. For condensing turbines, the parameters a and b are given by (Smith, 2016):

$$a = 1.3150 - 1.6347 \times 10^{-3} P_{in} - 0.36798 P_{out} \quad (42)$$

$$b = -437.77 + 29.007 P_{in} + 10.359 P_{out} \quad (43)$$

Where P_{in} and P_{out} are the turbine inlet and outlet pressures, respectively. The turbine overall efficiency, which accounts for both the isentropic and mechanical efficiencies, is the product $\eta_M \eta_{A,max}$ where $\eta_M = 0.98$ (Smith, 2016). The results are presented in Table 6.

Table 6. Turbine efficiencies.

Turbine	Turbine Efficiency (%)
TU-100	78.81
TU-101	78.53

The gas expander isentropic efficiency is assumed to be 80% based on the range of 70 – 90% efficiencies provided by Smith (Smith, 2016). The gas expander shaft is coupled to an electric generator having an efficiency of 97% (Smith, 2016). Furthermore, efficiencies of 90% are assumed for the electric drives of small compressors, fans, and pumps.

3.8 Utilities

Cooling water is supplied to heat exchangers at 30°C and returned at 40°C or less to limit mineral deposition on the walls of heat exchanger tubes. The returned water is cooled back to 30°C using mechanical draft cooling towers. Losses of circulating cooling water are caused by evaporation and windage from the mechanical draft towers, as well as purging needed to avoid salt accumulation. These losses represent approximately 2.2% of the circulating water flow rate (Turton et al., 2018) and are compensated by makeup cooling water.

Boiler feed water (BFW) is used to generate saturated steam in the MSR shell and to desuperheat the steam leaving E-120. The exhausts of turbines TU-100 and TU-101 are condensed with cooling water and recycled as circulating BFW. Blowdown losses of BFW are estimated to be 2.0% of the circulating flow rate and are replaced by makeup BFW.

Electricity is produced by electric generators coupled with the expander EX-101 and the turbine TU-101. Detailed accountings of all the utilities produced and consumed in the process are provided in Tables 7 & 8. The electricity generated in EX-101 & TU-101 is sufficient to satisfy the needs of the process, and the excess is exported as product.

Table 7. Breakdown of producers and consumers of electricity and steam.

ELECTRICITY	Duty (MW)	STEAM	Mass Flow (t/d)
<u>Electricity Producers</u>		<u>Steam Producers</u>	
EX-101	3.07	MSR	2,301
TU-101	19.44	Quench BFW	1,745
TOTAL PRODUCED	22.51	TOTAL PRODUCED	4,046
<u>Electricity Consumers</u>		<u>Steam Consumers</u>	
Cooling water loop pumps and fans	2.05	V-103 (BFW deaerator)	80
P-101	0.01	TU-100	2,112
P-102	<0.01	TU-101	1,854
P-103	0.26	TOTAL CONSUMED	4,046
E-111 (fans)	0.20		
E-117 (fans)	0.54	BALANCE	0
TOTAL CONSUMED	3.07		
BALANCE (EXPORTED ELECTRICITY)	19.44		

Table 8. Breakdown of producers and consumers of boiler feed water and cooling water.

BOILER FEED WATER (BFW)	Mass Flow (t/d)	COOLING WATER (CW)	Volume Flow (m³/d)
<u>BFW Producers</u>		<u>CW Producers</u>	
E-122 Condensate	3,966	Cooling towers	278,100
BFW make-up	79	Cooling water make-up	6,118
Deaerator steam condensate	80	TOTAL PRODUCED	284,218
TOTAL PRODUCED	4,125	<u>CW Consumers</u>	
<u>BFW Consumers</u>		E-104	18,240
MSR	2,301	E-106	2,375
Steam blowdown	79	E-113	1,464
Quench BFW	1,745	E-114	1,330
TOTAL CONSUMED	4,125	E-115	4,077
BALANCE		E-118	8,089
	0	E-122	209,900
		E-112	28,670
		E-116	3,955
		Evaporation, windage, purge (2.2% of cooling towers water)	6,118
		TOTAL CONSUMED	284,218
		BALANCE	0

Chapter 4. Process Performance

4.1 Energy Conversion from Natural Gas to Methanol

The energetic efficiency of converting natural gas to methanol can be quantified by the specific natural gas consumption of the process, NG_c (GJ LHV/t MeOH), defined as:

$$NG_c = \frac{\dot{m}_{NG} LHV_{NG}}{\dot{m}_{MeOH}} \quad (44)$$

where \dot{m}_{MeOH} and \dot{m}_{NG} are the mass flow rates of produced methanol and consumed natural gas, respectively, both in t/d. The lower heating value of natural gas, LHV_{NG} , depends on its composition and is equal to 46.60 GJ/t in this work.

In Tables 9 & 10, various parameters related to energy conversion and CO₂ emissions are reported for several methanol production processes. These processes differ in the methods used to produce the syngas, i.e., the mixture of H₂, CO₂ and CO needed for methanol synthesis. Processes 1 – 4 use natural gas pyrolysis to produce H₂, which is then combined with imported CO₂. In contrast, Processes 5 – 8 use methane reforming. All processes use similar methanol synthesis and distillation sections. Their capacities range from 2000 to 5000 tonnes per day of methanol.

Process 1 is the process designed in this research, as described in Sections 2 and 3 of this work. Hydrogen is generated in a catalytic liquid metal bubble reactor (CLMBR) by the pyrolysis of methane and other hydrocarbons present in natural gas.

Process 2 is the ideal Carnot process (Steinberg, 1995) where all the hydrocarbons in natural gas are fully converted to hydrogen and carbon by pyrolysis at 1100°C and 19.1 bar (same conditions as in this research). The heat of pyrolysis reactions is provided by the combustion of 17.7% of the produced hydrogen. The remaining H₂ is reacted in stoichiometric proportions with imported CO₂ in the MSR, where the reactants are fully converted to methanol and water. No pressure changes and no heat transfer other than the addition of heat to the pyrolysis reactor are considered.

Process 3 uses non-catalytic thermal pyrolysis (NCTP) of methane and other hydrocarbons to produce hydrogen, as described by Narine et al. (2021). The decomposition occurs in a fluidized bed reactor at 1500°C and 30 bar with a methane conversion of 95%. The produced H₂ is purified to >99 mol% by PSA. Combustion of natural gas and the PSA purge in a fired heater provides the heat requirements for the decomposition reactions and for utility steam production. Heat integration and compression duties are accounted for.

Process 4 is based on the NCTP process of Narine et al. (2021) but also includes an alkaline CO₂ capture (CC) system. It uses methyl-diethanolamine (MDEA) to capture 90% of the CO₂ in the flue gas exiting the fired heater. All the captured CO₂ is recycled to the inlet of the MSR where it reacts with H₂ to form methanol. Nonetheless, the captured CO₂ is not sufficient to meet the CO₂ needs of the process, and additional CO₂ needs to be imported.

Process 5 is the traditional steam methane reforming (SMR) process, which produces syngas composed of H₂, CO and CO₂. The data reported in Tables 9 & 10 pertain to a recent methanol project in the USA (Ingham, 2017). When ranges are shown, the left and right numbers correspond to minimum and maximum electricity imports, respectively. For minimum electricity import, all compressors and large pumps are actuated with steam driven turbines, and imported electricity is only used to power air cooler fans and smaller pumps. Maximum electricity import is achieved by maximizing the number of motor-driven compressors.

Process 6 incorporates a gas heated reformer (GHR) in series with an autothermal reformer (ATR) and is described in detail by Ingham (2017). This process can achieve a very high thermal efficiency when designed for maximum electricity import.

Process 7 is combined reforming (CR), which combines SMR and ATR. Tables 9 & 10 provide CR performance data taken from Collodi et al (2017). Although Ingham (2017) also reported data for CR, they are not included in Tables 9 & 10 because they are very similar to those of Collodi et al (2017).

Process 8 adds a CO₂ capture (CC) system to CR. 90% of the CO₂ contained in the SMR flue gas is removed using monoethanolamine solvent (Collodi et al, 2017)

Table 9. Comparison of energy conversion to methanol for different methane pyrolysis and methane reforming processes.

Process	Natural gas pyrolysis				Natural gas reforming			
	1	2	3	4	5	6	7	8
	CP-LMBR (This work)	Ideal Carnot (M. Steinberg, 1997a, 1997b; Meyer Steinberg, 1995, 1996b)	NCTP (Narine et al., 2021)	NCTP + CC (Narine et al., 2021)	SMR ^(a) (Ingham, 2017)	GHR + ATR ^(a) (Ingham, 2017)	CR (Collodi et al., 2017; IEAGHG, 2017)	CR + CC (Collodi et al., 2017; IEAGHG, 2017)
Natural gas consumption (GJ LHV/t MeOH)	53.9	46.8	54.1	56.6	32.6 – 32.4	31.0 – 25.5	30.4	30.4
Electricity import (GJ /t MeOH)	0	0	0	0	0.086 – 0.232	0.078 – 1.564	0.319	0.628
Electricity export (GJ /t MeOH)	0.840	0	0	0	0	0	0	0
Carbon production (mol C/mol MeOH)	1.84	1.90	1.68	1.68	0	0	0	0

^(a) The first and second values of ranges correspond to minimum and maximum electricity imports, respectively.

Table 9 shows that the natural gas consumption for pyrolysis based processes is significantly higher than that of reforming based processes (46.8-56.6 vs. 25.5-32.6 GJ LHV / t MeOH). This is in part due to the overall stoichiometry of the 2 processes. The pyrolysis based methanol synthesis stoichiometrically consumes 1.5 mols of CH₄ per mol of methanol produced (Equation 8) whereas a reforming based process only requires 1 mole of CH₄ per mol of methanol produced (Equations 1 & 6).

The larger natural gas requirement that a pyrolysis-based process has is partially offset by the ability to produce all electricity requirements in house as shown in Table 9. All investigated pyrolysis-based processes do not import electricity and, in the case of the CP-LMBR process designed in this work, electricity is exported. The same cannot be said of the natural gas reforming-based processes, all of which require the import of some amount of electricity. The CP-LMBR process designed in this work actually exports enough electricity to satisfy the needs of all the reforming-based processes individually.

Of the reforming-based processes the natural gas consumption is relatively the same for all processes except the GHR + ATR process designed for maximum electricity import. This design reduces the amount of natural gas required for steam production to run the compressors, pumps and air coolers because these units are now run by imported electricity. Similarly, by comparing CR to CR + CC, the addition of CC does not result in more natural gas consumption because these energy requirements are accounted for by an increase in electricity import.

The final row in Table 9 shows the carbon of methanol, which is unique to pyrolysis-based processes. The stoichiometry of Equation (8) shows that if all the hydrogen produced from the pyrolysis of methane reacted to form methanol, the ratio of carbon to methanol would be $3/2 = 1.5$. Similarly, if all the hydrogen produced from the pyrolysis of ethane reacted to form methanol, the ratio of carbon to methanol would be $2/1 = 2$ and so on for hydrocarbons of longer carbon chain length. Because this work considers a realistic natural gas mixture, the ideal ratio is 1.54 if all the produced H₂ reacted to form methanol. In all pyrolysis-based processes however, some of the produced hydrogen is lost in the PSA purge stream, as 100% hydrogen recovery is impossible. This hydrogen is thus used as fuel in the fired heater and does not react

to form methanol, meaning that the actual carbon to methanol ratio is higher than the ideal ratio. This parameter is therefore an indicator of how much hydrogen is being used as fuel in the fired heater of a pyrolysis-based process rather than being used to produce methanol.

It is therefore easy to understand why the Ideal Carnot process of Steinberg has the highest value, being that the combustion of hydrogen that is produced in the pyrolysis reaction satisfies all the heating requirements of his simplified process.

Interestingly, the NCTP process has the lowest value despite the high methane conversion in the pyrolysis reactor (95%). Figure 24 shows the trend that as methane conversion in the PR increases, the H₂ mol% in fuel also increases. This effect is accompanied by a decrease in H₂ recovery in the PSA and is due to the process being designed for a constant H₂ flow rate entering the MSR in this work. In the NCTP process, the PSA H₂ recovery is 80% with no reasoning provided for as to why that is the case. Nevertheless, the low carbon to methanol ratio indicates that natural gas is the primary source of fuel in the fired heater for the NCTP process which ultimately results in more natural gas consumption (54.1 GJ LHV/ t MeOH for NCTP vs. 53.9 GJ LHV/ t MeOH for CP-LMBR).

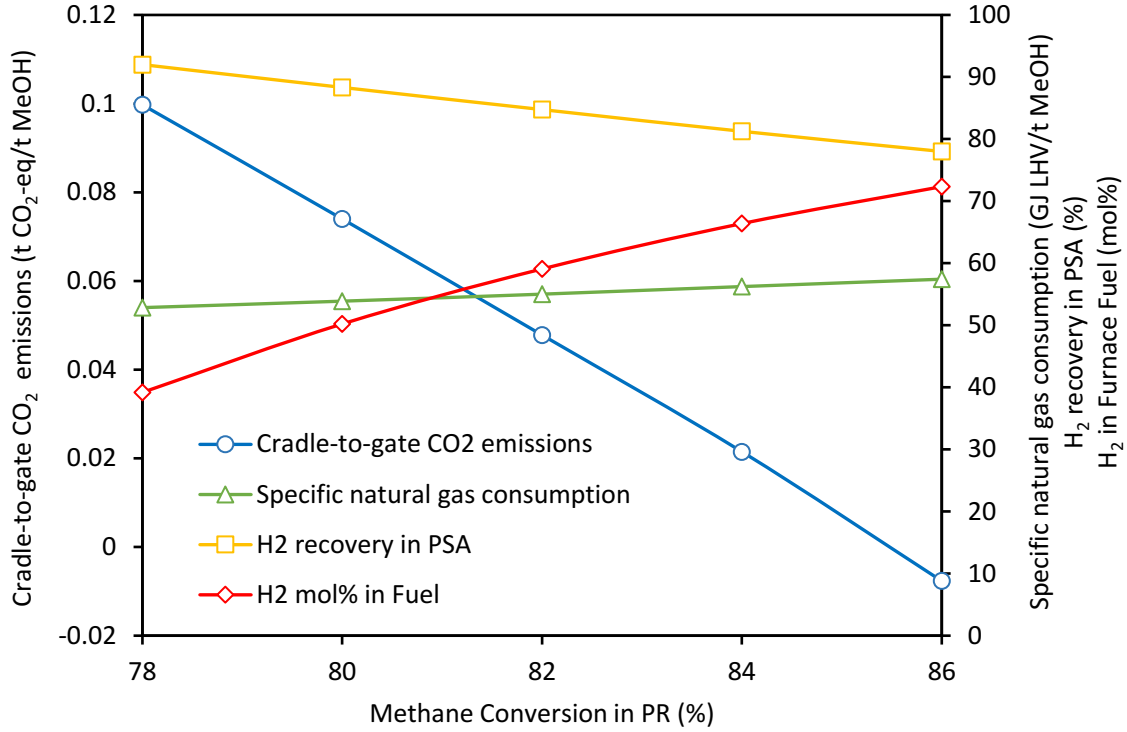


Figure 24. Effect of pyrolysis reactor methane conversion on cradle-to-gate emissions, natural gas consumption, PSA H₂ recovery and fuel H₂ mol%.

4.2 CO₂ accounting

The carbon footprint of methanol was first assessed by a cradle-to-gate analysis that considers the equivalent CO₂ emissions associated with the supply chains and the methanol production process until the methanol is ready for use. The cradle-to-gate emissions on the basis of 1 t of methanol, $m_{CO_2,cradle-to-gate}$ (t CO₂-eq/t MeOH), are given by:

$$\begin{aligned}
 m_{CO_2,cradle-to-gate} &= \frac{1}{\dot{m}_{MeOH}} \left(\dot{m}_{NG} (HHV_{NG}) F_{ng-supply} - \dot{m}_{CO_2,pipeline} \right. \\
 &\quad \left. + \dot{m}_{CO_2,pipeline} F_{CO_2-supply} + W_{el} F_{elect.-supply} + \dot{m}_{FG} y_{CO_2,FG} \right) \quad (45)
 \end{aligned}$$

where $\dot{m}_{CO_2,pipeline}$ is the incoming CO₂ mass flow rate (t/d) (assumed to be captured from another process and delivered by pipeline), \dot{m}_{FG} is the mass flow rate (t/d) of flue gas emitted by the methanol plant, $y_{CO_2,FG}$ is the mass fraction of CO₂ in the flue gas, and W_{el} is the

electricity imported by the plant (GJ/d). The emissions factors $F_{ng-supply}$ (t CO₂-eq/GJ HHV), $F_{CO_2-supply}$ (t CO₂-eq/t CO₂), and $F_{elect.-supply}$ (t CO₂-eq/GJ) account for the equivalent CO₂ emissions associated with the total supply chain of natural gas, the capture and transport of CO₂ to the methanol plant, and the production and delivery of electricity imported by the plant, respectively.

The numerical values of the emissions factors are set to reasonable intermediate values within the ranges of published values. The factor $F_{ng-supply}$ is set to 0.0106 t CO₂-eq/GJ HHV, which corresponds to the median of North American estimates from the comprehensive review of Balcombe et al., (2017). The factor $F_{CO_2-supply}$ is set to 0.20 t CO₂-eq/t CO₂ based on CO₂ capture at a natural gas combined cycle (NGCC) power plant (Assen et al., 2016). Transport of CO₂ by pipeline would result in additional emissions of 0.001 – 0.002 t CO₂-eq/t CO₂ per 100 km (Assen et al., 2016). Hence, for reasonable transport distances (a few hundred km or less), the additional emissions from CO₂ transport are relatively small compared with the emissions from CO₂ capture, and they are neglected in the present analysis. The factor $F_{elect.-supply}$ is set to 0.1203 t CO₂-eq/GJ (0.433 t CO₂-eq/MWh), which represents the average value for electricity imported from the US grid in 2019 (EPA, 2019) (EPA (United States Environmental Protection Agency), n.d.). The CP-LMBR process generates enough electricity internally to satisfy its own needs and even export excess electricity. As a result, the process does not import electricity and, therefore, $W_{el} = 0$. Nevertheless, the factor $F_{elect.-supply}$ is important when comparing the CO₂ emissions of the CP-LMBR process to those of other methanol production processes that import electricity from the grid.

Note that all the CO₂ contained in the natural gas (1.9 mol%) is eventually emitted in the flue gas since it is recovered in the purge of the PSA which is burned as fuel. As a result, it is implicitly included in the last term of Equation (45). Although the CO₂ content of natural gas is a CO₂ input to the plant, it is not captured from another process, and therefore it does not avoid an emission that would otherwise have occurred. Hence, the CO₂ content of natural gas is not taken as a credit in the calculation of cradle-to-gate emissions (Hamelink, C., Bunse, 2022).

Since a significant fraction of the global methanol production is used as a fuel or gasoline additive, a cradle-to-grave analysis was also done to account for end-of-life emissions due to methanol combustion. The cradle-to-grave (also called well-to-wheel) emissions on the basis of 1 t of methanol, $m_{CO_2,cradle-to-grave}$ (t CO₂-eq/t MeOH), are given by:

$$m_{CO_2,cradle-to-grave} = m_{CO_2,cradle-to-gate} + 1.374 \quad (46)$$

The 1.374 t CO₂-eq/t MeOH accounts for the emissions due to methanol combustion and is determined based on the stoichiometry of the methanol combustion reaction. Emissions associated with the distribution of methanol are neglected, since this would require making arbitrary assumptions about shipping distances and modes of transportation.

One of the process design variables is the methane conversion in the PR, which effects many key process parameters. Figures 24 and 25a-b show the effect that the conversion has on all the parameters that were taken into consideration when selecting the final operating conversion.

Figure 24 shows that as $X_{CH_4,PR}$ varies from 78% to 86%, the specific natural gas consumption increases from 52.9 to 57.4 GJ LHV/t MeOH, the hydrogen recovery in the PSA decreases from 92% to 78%, and the cradle-to-gate CO₂ emissions decrease from 0.100 to -0.008 t CO₂-eq/t MeOH. These trends relate to the PSA purge and the amount of fuel required by the fired heater to meet the process energy requirements.

As methane conversion in the PR increases, the amount of PSA purge, which contains the unreacted methane, would decrease if the amount of natural gas fed to the process was kept constant. This would result in less fuel to the fired heater and an inadequate amount of energy production. Therefore, higher methane conversion must be accompanied by an increase in the amount of natural gas feed in order to provide heat for the pyrolysis reactions and to maintain the temperature of the flue gas exiting the radiant zone at around 1130°C. Meanwhile, because more hydrogen is produced in the PR, the hydrogen recovery in the PSA must decrease to keep a constant flow rate of H₂ to the MSR, which is another design variable. As a result, the hydrogen mole fraction in the PSA purge gas increases accompanied by a decrease in the methane mole fraction, as shown in Figure 24. This results in a decrease in CO₂ emissions due

to the fact that the combustion of H_2 generates no CO_2 and the amount H_2 being combusted is increasing and the amount of CH_4 being combusted is decreasing. As a result, negative cradle-to-gate CO_2 emissions are possible at a PR CH_4 conversion of 86% because the process imports captured CO_2 .

Figure 25a shows that the TU-100 shaft power increases with increasing methane conversion. This occurs because as methane conversion increases, the PR outlet pressure decreases (Figure 25b), and therefore more power is consumed in compressor K-101 to compress the PR product upstream of the PSA. As more superheated steam is consumed in TU-100 to satisfy the shaft duty increase in K-101, less flows to TU-101. Hence, the amount of exported electricity decreases from 875 to 650 MJ/t MeOH as $X_{CH_4,PR}$ increases from 78% to 86%.

From an operational and economical point of view, the most significant challenge for achieving large methane conversions in the PR is the exponential relationship between the required volume of molten metal alloy and the methane conversion (Figure 25b). Increasing $X_{CH_4,PR}$ from 78% to 86% requires more than doubling the molten metal volume for a relatively modest reduction in the cradle-to-gate CO_2 emissions (Figure 24). As a result, the methane conversion is set to 80% as this keeps the molten metal alloy volume slightly under 100 m^3 and results in cradle-to-gate CO_2 emissions of $0.074\text{ t }CO_2\text{-eq/t MeOH}$.

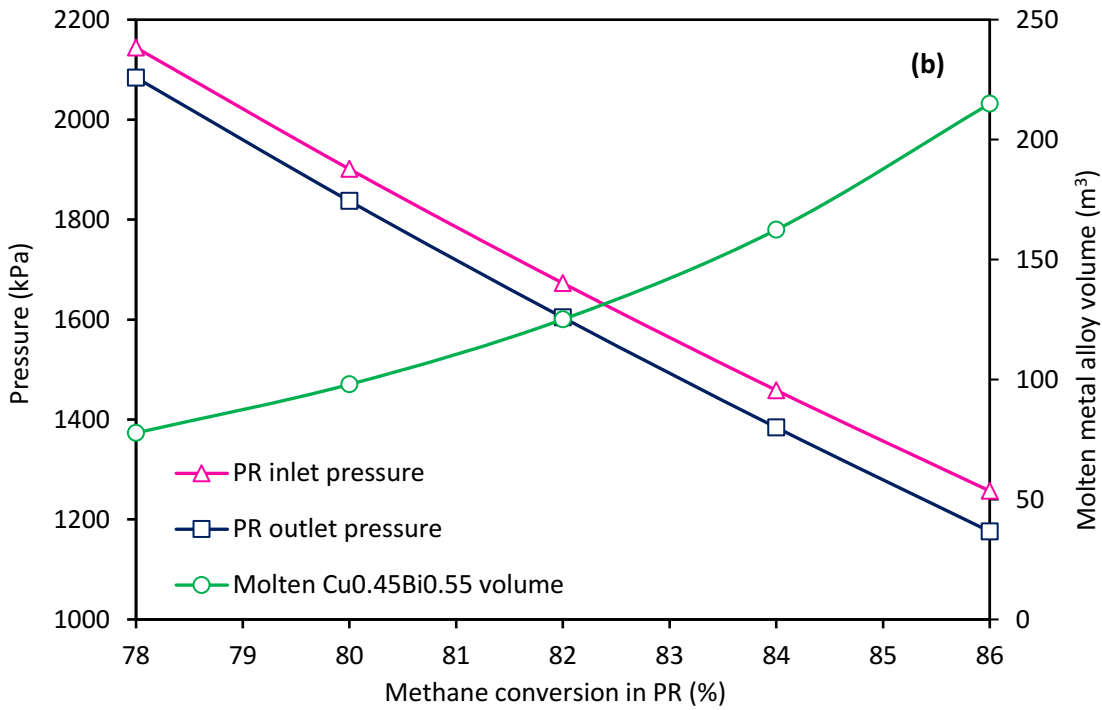
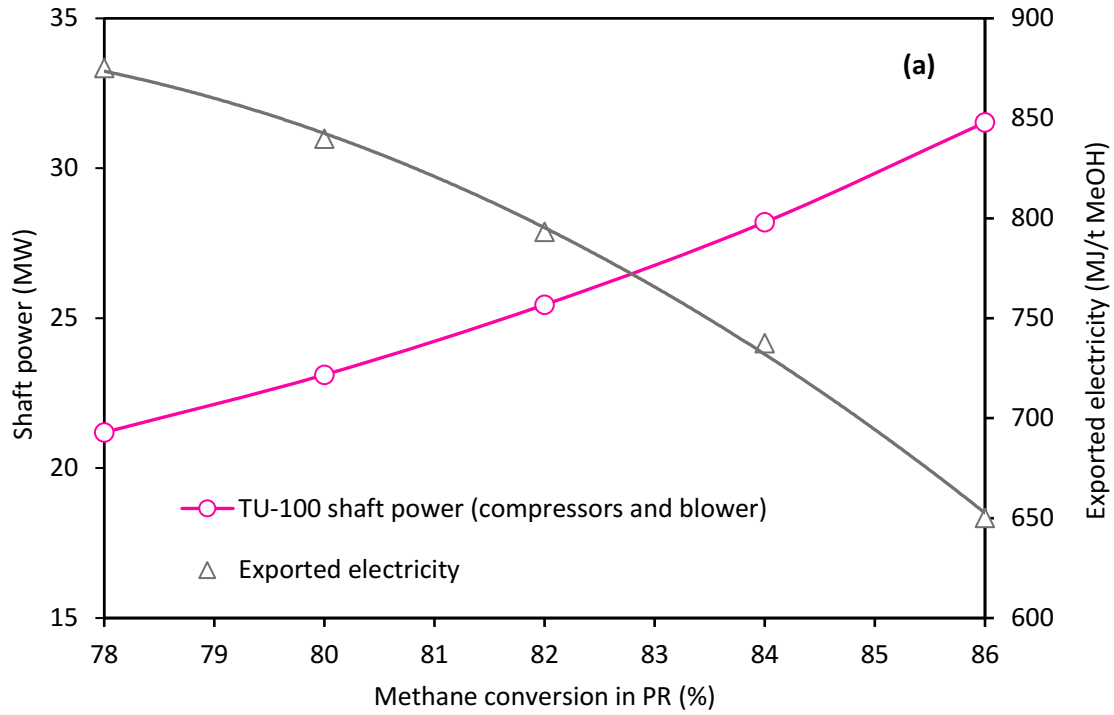


Figure 25. Effect of methane conversion in the PR on TU-100 shaft power, exported electricity, molten metal alloy and inlet and outlet pressures.

Table 10. Comparison of CO₂ accounting for different methane decomposition and methane reforming processes.

Process	Natural gas pyrolysis				Natural gas reforming			
	1	2	3	4	5	6	7	8
	CP-LMBR (This work)	Ideal Carnot (M. Steinberg, 1997a, 1997b; Meyer Steinberg, 1995, 1996b)	NCTP (Narine et al., 2021)	NCTP + CC (Narine et al., 2021)	SMR ^(a) (Ingham, 2017)	GHR + ATR ^(a) (Ingham, 2017)	CR (Collodi et al., 2017; IEAGHG, 2017)	CR + CC (Collodi et al., 2017; IEAGHG, 2017)
A. CO₂ feed from CO₂ pipeline (t CO₂-eq/t MeOH)	1.399	1.333	1.47	0.76	0	0	0	0
B. CO₂ emissions (t CO₂-eq/t MeOH)								
B1. Natural gas supply chain	0.628	0.548	0.631	0.659	0.380 – 0.378	0.361 – 0.297	0.354	0.354
B2. CO ₂ feed to plant	0.280	0.267	0.294	0.152	0	0	0	0
B3. Methanol plant	0.565	0.009	0.77	0.22	0.445 – 0.434	0.371 – 0.067	0.353	0.035
B4. Imported electricity (US mix)	0	0	0	0	0.010 – 0.028	0.009 – 0.188	0.038	0.075
Total CO ₂ emissions (B = B1 + B2 +B3 +B4)	1.473	0.823	1.695	1.031	0.836 – 0.839	0.742 – 0.552	0.746	0.465
Cradle-to-gate CO₂ emissions (B - A) (t CO₂-eq/t MeOH)	0.074	-0.510	0.225	0.271	0.836 – 0.839	0.742 – 0.552	0.746	0.465
C. End of life emissions if methanol is combusted (t CO₂-eq/t MeOH)	1.374	1.374	1.374	1.374	1.374	1.374	1.374	1.374
Cradle-to-grave CO₂ emissions (B – A + C) (t CO₂-eq/t MeOH)	1.448	0.864	1.599	1.645	2.210 – 2.213	2.116 – 1.926	2.120	1.839

^(a) The first and second values of ranges correspond to minimum and maximum electricity imports, respectively.

Table 10 shows the CO₂ accounting of the various pyrolysis and reforming-based methanol synthesis processes investigated in this work. Overall, the results indicate that pyrolysis-based processes have lower cradle-to-gate and cradle-to-grave emissions than reforming based processes.

Comparing the pyrolysis-based processes, the ideal Carnot process presents an absolute minimum which is unachievable in reality due to the fact that in the ideal process no heat losses in the process are accounted for. These losses would need to be made up for by the combustion of more fuel which would result in an increase in methanol plant emissions if natural gas were used (Table 10 Row 3). Currently these emissions are nearly negligible.

Comparing the CP-LMBR process to the NCTP process shows that the methanol plant emissions are less in the CP-LMBR process. Because the only plant CO₂ emissions in both processes are in the flue gas. This confirms the findings in Table 9 where despite the higher PR CH₄ conversion, the NCTP process uses primarily natural gas as fuel in the fired heater and has a larger natural gas consumption whereas the CP-LMBR process uses a fair amount of hydrogen (50.2 mol% H₂) in the fuel to the fired heater and lower natural gas consumption. This is the main contributor to the lower cradle-to-gate and cradle-to-grave emissions in the CP-LMBR process compared to the NCTP processes.

Comparing the four reforming based processes reveals that they all have relatively similar cradle-to-gate and cradle-to-grave emissions except for the GHR + ATR process designed for maximum electricity import and the addition of CC to the CR process, which result in large reductions in the emissions. Even with these reductions however, both processes have larger emissions values than the pyrolysis-based processes.

Table 10 shows that pyrolysis-based processes emit much more CO₂ in the natural gas supply chain than reforming-based processes, which is confirmed by analysis of Table 9, which indicates the higher natural gas consumption per ton of methanol produced by pyrolysis-based processes compared to reforming-based ones. This effect is also reflected in the methanol plant direct emissions. The higher plant direct emissions for the pyrolysis-based processes are a by product of the process being more energy intensive resulting in a larger requirement of natural

gas combustion for heating purposes. This must be the case as the only direct CO₂ emissions in the methane pyrolysis process are in the flue gas.

The CO₂ emissions due to electricity import are very small however, the requirement for electricity import that reforming-based processes have contribute to the larger cradle-to-gate and cradle-to-grave emissions compared to the pyrolysis-based ones.

Where the methane pyrolysis processes excel compared to the reforming processes is in the fact that they use CO₂ as a raw material, which is shown in Table 10 Row A. Reforming processes produce their required CO₂ in the reforming stage of the process whereas methanol production using methane pyrolysis imports CO₂ from the pipeline resulting in more effective CO₂ utilization. This import is one of the main contributors to the fact that methanol production using methane pyrolysis emits less CO₂ per tonne of methanol produced compared to combined reforming processes. With this fact in mind, it is important to consider the CO₂ emissions associated with CO₂ capture (Table 10 row B2) to ensure that the biggest advantage that a methanol synthesis plant based on methane pyrolysis has compared to a reforming based one is accurately assessed.

The benefit of CO₂ import as a raw material in a pyrolysis-based process is best exemplified in comparing the cradle-to-gate and cradle-to-grave emissions of the CP-LMBR and NCTP process with those of the CR + CC and NCTP + CC process. Comparing the NCTP process to the NCTP + CC process reveals that the addition of CC to a pyrolysis-based process actually increases both the cradle-to-gate and cradle-to-grave emissions. This is explained by the fact that the reduction in methanol plant emissions associated with CC (Table 10 Row B3, $0.77 - 0.22 = 0.55$ t CO_{2-eq} / t MeOH) is less than the decrease in CO₂ imported to the plant (Table 3 Row A, $1.47 - 0.76 = 0.71$ t CO_{2-eq} / t MeOH). The conclusion can therefore be drawn that adding CC to a pyrolysis-based process is not beneficial and in fact increases the plant overall emissions. Comparing the CP-LMBR and NCTP processes to the CR + CC process reveals that both pyrolysis-based processes outperform the CR + CC process, which in Table 10 is the best performing reforming-based process from an emissions perspective.

4.3 CO₂ Emissions Sensitivity Analysis

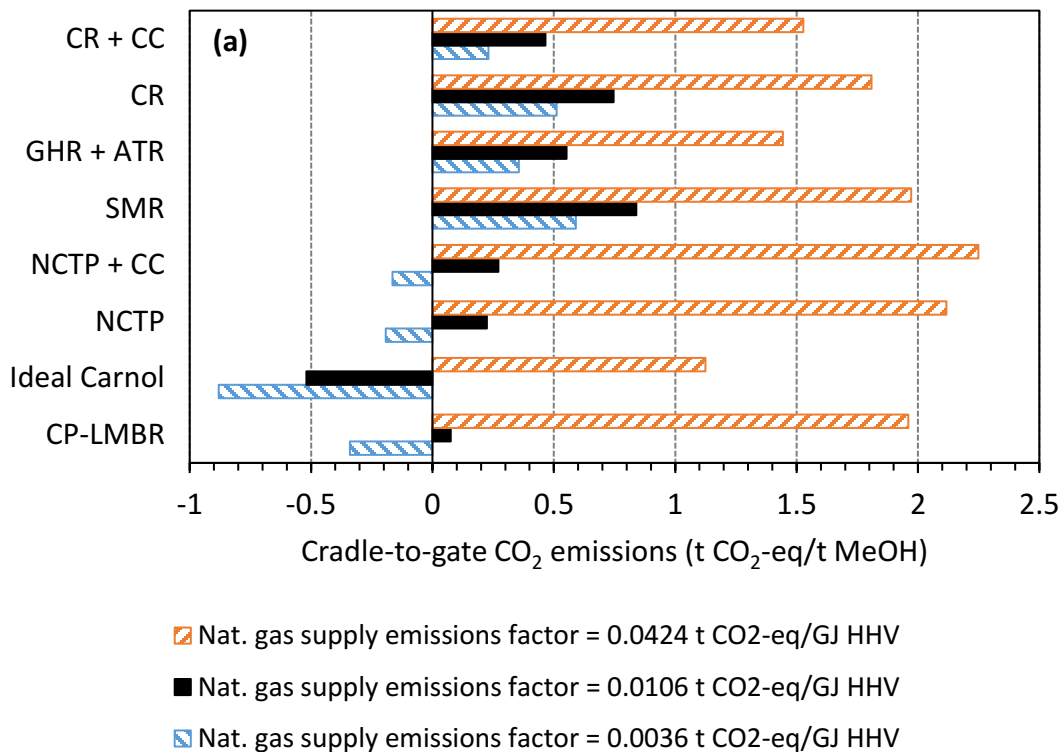
Figure 26a-c assesses the sensitivity of the cradle-to-gate CO₂ emissions from the various methanol production processes to variations in emissions factors for a) the natural gas supply chain, b) the CO₂ capture, and c) the imported electricity. The emissions factors are varied one at a time. For the natural gas total supply chain in North America, $F_{ng-supply}$ varies between 0.0036 and 0.0424 t CO₂-eq/GJ HHV (Paul Balcombe et al., 2017). For CO₂ capture, $F_{CO_2-supply}$ ranges from 0.06 t CO₂-eq/t CO₂ when CO₂ is supplied by chemical plants to 0.44 t CO₂-eq/t CO₂ when CO₂ is directly captured from air (Assen et al., 2016). For imported electricity, $F_{elect.-supply}$ varies between nearly 0 for renewable electricity sources and 0.273 t CO₂-eq/GJ (0.982 t CO₂-eq/MWh) for the average of coal-fired power stations in the US in 2019 (EPA (U.S. Environmental Protection Agency), n.d.). Data for SMR and GHR + ATR assume maximum electricity imports to emphasize the potential effect of $F_{elect.-supply}$ on these processes.

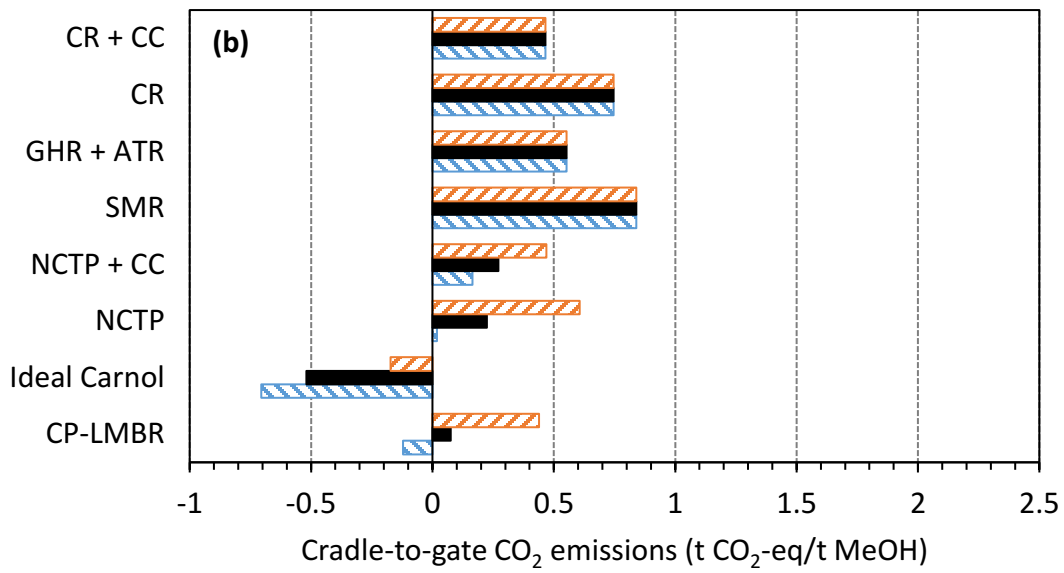
Figure 26a shows that all processes are highly sensitive to $F_{ng-supply}$ but the pyrolysis processes are even more sensitive than the reforming processes, as shown by the differences in CO₂ emissions between the high-end and low-end values of $F_{ng-supply}$. This is because pyrolysis processes consume more natural gas per tonne of methanol production than reforming processes, as was previously mentioned in Section 4.1 and shown in Table 9. Low-end $F_{ng-supply}$ results in negative cradle-to-gate CO₂ emissions for all pyrolysis processes, reaching -0.341 t CO₂-eq/t MeOH for the CP-LMBR process. In contrast, high-end $F_{ng-supply}$ causes the CO₂ emissions of the CP-LMBR process to exceed those of the GHR + ATR, CR, and CR + CC processes. In fact, this is the only scenario shown in Figures 26a-c where the CP-LMBR process does not outperform all other realistic methanol production processes. Therefore, the availability of natural gas supply chains with low $F_{ng-supply}$ is key for justifying the pyrolysis processes.

Figure 26b shows that the pyrolysis-based processes are relatively less sensitive to $F_{CO_2-supply}$ than to $F_{CO_2,ng-supply}$ while reforming processes are completely insensitive to $F_{CO_2-supply}$ since they do not import CO₂. Of the realistic processes, the CP-LMBR process is the only one that achieves negative cradle-to-gate emissions, reaching -0.122 t CO₂-eq/t MeOH. Even at the

high end of 0.439 t CO_{2-eq}/t MeOH, the CP-LMBR process still outperforms all reforming based processes, which are insensitive to this parameter. Even though this is the case, accessing sources of CO₂ with low $F_{CO_2-supply}$ is essential for maximizing the environmental benefit of the CP-LMBR process. The NCTP and NCTP+CC processes also benefit from low $F_{CO_2-supply}$ values but their cradle-to-gate emissions remain positive at the low-end of $F_{CO_2-supply}$ values.

The natural gas pyrolysis processes are insensitive to $F_{elect.-supply}$ since they import no electricity. Among reforming processes, the GHR+ATR process is the most sensitive to $F_{elect.-supply}$ because it uses electrical drives to meet nearly all the shaft power requirements of the plant, which results in a much higher electricity consumption than other processes (Ingham, 2017). The CR + CC process is also sensitive to $F_{elect.-supply}$ as the regeneration of the CO₂ sorbent consumes a significant amount of steam, which requires importing a larger amount of electricity to meet the power needs of the plant. Nonetheless, the cradle-to-gate CO₂ emissions of the GHR + ATR and CR + CC processes are well above those of the CP-LMBR process even when renewable electricity is used.





▨ CO₂ supply emissions factor = 0.46 t CO₂-eq/t CO₂

■ CO₂ supply emissions factor = 0.20 t CO₂-eq/t CO₂

▨ CO₂ supply emissions factor = 0.06 t CO₂-eq/t CO₂

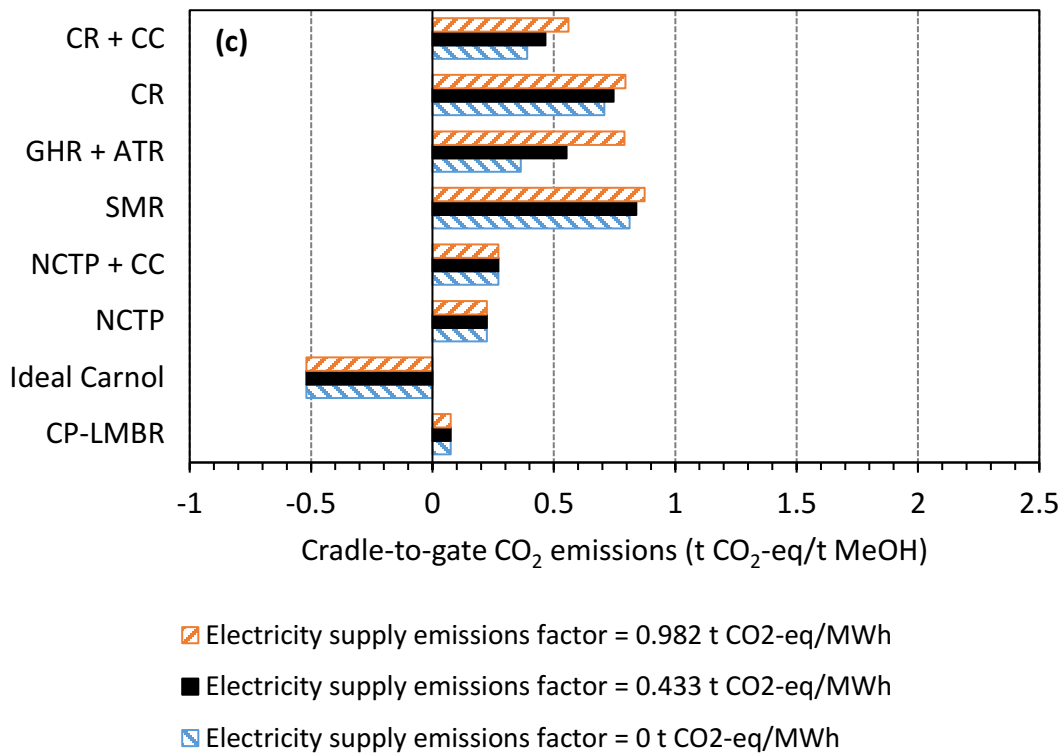


Figure 26. Effect of the CO₂ emissions factors for (a) natural gas supply, (b) CO₂ supply, and (c) electricity supply on the cradle-to-gate CO₂ emissions of several natural gas pyrolysis and reforming processes. Data for SMR and GHR + ATR assume maximum electricity imports to emphasize the effect of $F_{elect.-supply}$ on the emissions of these processes.

In the best case scenario for the CP-LMBR process, where $F_{ng-supply}$ and $F_{CO_2-supply}$ are both at their low-end values of 0.0036 t CO₂-eq/GJ HHV and 0.06 t CO₂-eq/t CO₂, the cradle-to-gate and cradle-to-grave CO₂ emissions of CP-LMBR would be -0.537 and 0.837 t CO₂-eq/t MeOH, respectively. By comparison, the emissions of the GHR + ATR under the same conditions and operated with renewable electricity would be much higher at 0.168 and 1.542 t CO₂-eq/t MeOH. Hence, the CP-LMBR process could reduce cradle-to-grave emissions by up to 46% when compared to the best performing reforming process considered in this work.

Chapter 5. Economic Analysis of Methanol Production Plant

5.1 Estimation of Capital Costs

The capital cost of the plant was estimated using the module costing technique (Turton et al., 2018).

The base purchase cost of equipment at ambient operating pressure and using carbon steel construction, C_p^o , is estimated by (Turton et al., 2018):

$$\log_{10} C_p^o = K_1 + K_2 \log_{10}(A) + K_3 [\log_{10}(A)]^2 \quad (47)$$

where A is the capacity of the equipment whose definition depends on the type of equipment (e.g., heat exchange area for heat exchangers, fluid power for compressors, etc.). The values of the parameters K_1 , K_2 , and K_3 are specific to each type of equipment and are tabulated in Turton et al (Turton et al., 2018).

The base bare module cost, C_{BM}^o , is the sum of the direct and indirect costs associated with the equipment at ambient operating pressure and using carbon steel construction. Direct costs include the equipment cost, materials required for installation, and the installation labor. The indirect costs include freight, insurance, taxes, construction overhead, and contractor engineering expenses. The base bare module cost and the base purchase cost are related by:

$$C_{BM}^o = C_p^o F_{BM}^o \quad (48)$$

where F_{BM}^o is the base bare module factor, which is given in Turton (Turton et al., 2018) for many different types of equipment.

When the equipment operates at a pressure different from atmospheric, and/or the material of construction (MOC) is different from carbon steel, the bare module cost, C_{BM} , is given by:

$$C_{BM} = C_p^o F_{BM} \quad (49)$$

where the bare module factor, F_{BM} , includes correction factors related to pressure and MOC, as detailed in Turton (Turton et al., 2018).

The total module cost, C_{TM} , includes a contingency factor as a protection against oversights and incorrect information in the cost data. The contingency and fees are assumed to be 15% and 3% of the bare module cost, respectively (Turton et al., 2018). The C_{TM} for the entire plant is calculated as follows:

$$C_{TM} = 1.18 \sum_{i=1}^n C_{BM,i} \quad (50)$$

Where n represents the total number of pieces of equipment.

Because the proposed methanol plant is a completely new facility, the construction will likely take place on undeveloped land. As a result, there will be additional costs for site development, auxiliary buildings, and utilities such as wastewater treatment and cooling water facilities. These additional costs, which are usually not affected by the operating pressures and the materials of construction of the process, are assumed to be equal to 50% of the sum of the base bare module costs. The grassroots cost of the entire plant, C_{GR} , includes the additional costs for constructing the plant on undeveloped land and is evaluated as:

$$C_{GR} = C_{TM} + 0.50 \sum_{i=1}^n C_{BM,i}^o \quad (51)$$

Table 11 provides estimates of C_p^o , C_{BM} , C_{BM}^o for all pieces of equipment of the CP-LMBR plant. Given the limited options available for materials of construction in CAPCOST, the following criteria are used: Carbon steel (CS) is chosen for equipment operating below 400°C such as the water pumps, the combustion air fan, and the shell or tube sides of heat exchangers not containing hydrogen or methanol. Stainless steel (SS) is used for equipment operating at temperatures in the range of 400-600°C and/or in contact with hydrogen or methanol. All the compressors are made of SS because of the presence of hydrogen at high temperature and pressure. The tubes of the methanol synthesis reactor, as well as the distillation towers and their internals, are made of SS because of the presence of methanol. Similarly, the interior of the flash vessels are clad with SS. Nickel-based alloys are chosen for equipment operating at

temperatures higher than 600°C, such as the feed-effluent heat exchanger E-101 (maximum of 1100°C) and the PR tubes (maximum above 1100°C).

The bare module cost of each piece of equipment, $C_{BM,i}$, which represents the sum of direct and indirect costs (purchase, shipping, installation, etc.), was estimated with CAPCOST (2017) (*CAPCOST 2017*, n.d.) or from literature data.

The cost of equipment items not available in the CAPCOST database are estimated as shown below.

5.1.1 Cost of Copper-Bismuth Alloy

The cost of molten copper-bismuth alloy contained in the PR tubes is estimated separately and added to the capital cost of the pyrolysis furnace. The average price of copper in 2019 was \$2.72/lb or \$6.00/kg (*Copper Prices - 45 Year Historical Chart*, n.d.). Over the past decade, the price of bismuth (99.99% Bi ingots) has fluctuated between \$3 and \$14 per pound (*Bismuth Price*, n.d.). Current prices from Alibaba.com range between US\$12 and US\$100 per kg, depending on suppliers and order size. Since a very large order of bismuth will be required for the PR, a bismuth price of \$12/kg is assumed.

The $\text{Cu}_{0.45}\text{Bi}_{0.55}$ alloy has the following mass composition:

$$\text{Cu mass \%} = 0.45 M_{\text{Cu}} / (0.45 M_{\text{Cu}} + 0.55 M_{\text{Bi}}) = 0.45 \times 63.55 / (0.45 \times 63.55 + 0.55 \times 208.98) = 19.92\%$$

$$\text{Bi mass\%} = 0.55 M_{\text{Bi}} / (0.45 M_{\text{Cu}} + 0.55 M_{\text{Bi}}) = 0.55 \times 208.98 / (0.45 \times 63.55 + 0.55 \times 208.98) = 80.08\%$$

Hence, the cost of the $\text{Cu}_{0.45}\text{Bi}_{0.55}$ alloy is estimated to be equal to $6.00 \times 0.1992 + 12 \times 0.8008 = \$10.8/\text{kg}$. The PR reactor contains 85.6 m^3 of molten alloy excluding the gas holdup (Table 3), and its density at 1100°C is estimated to be 8810 kg/m^3 (Catalan & Rezaei, 2022). Therefore, the total cost of the alloy is $10.8 \times 8810 \times 85.6 = \8.145 million.

5.1.2 Cost of Sodium Bromide Salt

The cost of sodium bromide from Alibaba.com varies between \$1 and more than \$30/kg. A cost of \$1/kg is selected since the PR requires large amounts of NaBr. The initial load of NaBr is added to the capital cost of the pyrolysis furnace and corresponds to a molten salt thickness of 0.24 m in the production manifolds connected to the top of the PR tubes. The cross-sectional area of the manifolds is assumed to be roughly twice that of the tubes. PR tubes have an internal diameter of 0.1 m corresponding to a cross-sectional area of 0.007854 m². Since there are 16,513 tubes (Table 3), the volume of molten NaBr is estimated to be $(2)(16,513)(0.007854)(0.24) = 62.3 \text{ m}^3$. Since the density of NaBr is 3210 kg/m³, the cost of the initial load is $(3210)(62.3)(1) = \$199,831$.

5.1.3 Cost of Pressure Swing Adsorption (PSA)

Turton (Turton et al., 2018) gives the following for the total module cost of PSA for hydrogen recovery:

$$C_{TM}(2016) = 0.817 \left(\frac{F}{944} \right)^{0.55} \quad (52)$$

where F is the flow rate (Nm³/h) of pure H₂ produced by the PSA. For our plant, $F = 1.879 \times 10^5$ Nm³/h, which results in $C_{TM}(2016) = \$15.02$ million. Adjusting for inflation and the relationship between C_{TM} and C_{BM} :

$$\begin{aligned} C_{BM}(2019) &= \frac{1}{1.18} \left(\frac{CEPCI 2019}{CEPCI 2016} \right) C_{TM}(2016) = \frac{1}{1.18} \left(\frac{608}{542} \right) (15.02) \\ &= \$14.3 \text{ million} \end{aligned} \quad (53)$$

Luberti (Luberti, 2015) estimated a C_{BM} of 20.297 million (in 2014 US dollars) for a PSA unit treating 1,745 mol/s of gas with an inlet H₂ concentration of 88.75 mol% and producing ultrapure H₂ (99.99+ mol%) with a hydrogen recovery of 91.26%. The PSA unit configuration consisted of two parallel trains, each including 9 columns. The number of columns was

optimized to minimize cost. These operating conditions are comparable to those in our CP-LMBR process, where the inlet gas flow rate is 2,801 mol/s, the inlet H₂ concentration is 89.2 mol%, and the H₂ recovery is 88.25%. Using the power law factor of 0.55 from Turton (Turton et al., 2018) to account for differences in inlet flow rates, and adjusting for inflation, gives:

$$C_{BM}(2019) = \left(\frac{CEPCI\ 2019}{CEPCI\ 2014}\right) C_{BM}(2014) = \left(\frac{608}{576}\right) \left(\frac{2801}{1745}\right)^{0.55} (20.297) \quad (54)$$

$$= \$27.8\ million$$

For conservativeness, the estimate of \$27.8 million is used in the present analysis.

5.1.4 Cost of Methanol Synthesis Reactor (MSR) and Catalyst

The cost of the MSR reactor was evaluated as that of a shell-and-tube heat exchanger having the same heat exchange area and operating at the same pressures and temperatures. The cost of the Cu/Zn/Al₂O₃ methanol synthesis catalyst from Alibaba.com ranges from \$20 to \$99/kg, depending on supplier and order size. Since the plant will order large quantities of catalyst, a price of \$20/kg is assumed. The catalyst has a typical loading density of 1200-1300 kg/m³ (Topsoe, n.d.). Since the reactor contains 300 m³ of catalyst, the cost of the initial load is (1250)(300)(20) = \$7.50 million. This cost is added to the capital cost of the reactor.

5.1.5 Cost of Plate Heat Exchanger for Solid Carbon

Sjostrom et al (Sjostrom, S., Denney, J., Morris, 2016) report a bare module cost of \$10.295 million for a Solex plate heat exchanger designed for a solid flow rate of 1195 t/h in the year 2015. Using a typical power law factor of 0.6, and a carbon flowrate of $F = 57.5$ t/h for the CP-LMBR process, gives:

$$C_{BM}(2019) = 10.295 \left(\frac{F}{1195}\right)^{0.6} \left(\frac{CEPCI\ 2019}{CEPCI\ 2015}\right) = 10.295 \left(\frac{57.5}{1195}\right)^{0.6} \left(\frac{608}{557}\right) \quad (55)$$

$$= \$1.82\ million$$

This cost applies to each one of the two plate heat exchangers (E-105 and E-106).

5.1.6 Total Plant Module Cost

The total module cost of the plant, C_{TM} , was obtained by multiplying the sum of bare module costs by a contingency and fee factor of 1.18 to account for uncertainties in the cost data:

$$C_{TM} = 1.18 \sum_{i=1}^n C_{BM,i} \quad (56)$$

where n represents the total number of equipment items. Because the plant is assumed to be constructed on undeveloped land, costs for site development and auxiliary facilities were added to the sum of the total module costs to obtain the grassroots cost, C_{GR} , of the plant:

$$C_{GR} = 1.18 \sum_{i=1}^n C_{BM,i} + 0.50 \sum_{i=1}^n C_{BM,i}^o \quad (57)$$

The second term on the right-hand side of Equation (57) shows that the additional costs were estimated as 50% of the sum of the base bare module costs, $C_{BM,i}^o$. The base bare module is defined as the sum of the direct and indirect costs of the equipment designed to operate at ambient pressure and constructed of carbon steel. All costs are reported in US\$ for the year 2019 using the Chemical Engineering Plant Cost Index (CEPCI) to account for inflation (Turton et al., 2018).

Table 11 shows the breakdown of C_{GR} (\$340.0 million) by equipment type. The most expensive unit is the fired heater containing the pyrolysis reactor. This unit is costed as the sum of a pyrolysis furnace, the molten $\text{Cu}_{0.45} \text{Bi}_{0.55}$ alloy in the PR tubes, and the molten salt in the production manifolds. In CAPCOST, the estimated cost of a pyrolysis furnace depends on its heating duty, pressure in the tubes, and material of construction. The furnace duty is calculated as product of the fuel flowrate and the fuel LHV. The molten $\text{Cu}_{0.45} \text{Bi}_{0.55}$ alloy and molten NaBr salt are estimated to cost \$8.1 million and \$0.2 million, respectively. The total fired heater cost is \$90.0 million and accounts for 26.5% of C_{GR} . The next two most expensive items are the auxiliary facilities (19.7% of C_{GR}) and the compressors (14.2 % of C_{GR}). The most expensive

compressors are K-101, which compresses the gas leaving the PR before entering the PSA, and K-102, which compresses the hydrogen exiting the PSA before entering the MSR.

Since the CP-LMBR plant produces 2000 t MeOH/d and is assumed to operate 95% of the time, its grassroots cost is equivalent to \$490/(t MeOH/y). By comparison, Collodi et al. (Collodi et al., 2017) reported total plant costs of €480 and €560/(t MeOH/y) for their CR and CR + CC plants producing 5000 t MeOH/d, respectively. Narine et al. (Narine et al., 2021) estimated a fixed capital investment of \$804/(t MeOH/y) for their NCTP process producing 2800 t MeOH/d. Although the CP-LMBR process appears to have lower capital costs than these other processes when normalized by the methanol production rate, it should be kept in mind that all the capital cost estimates were obtained by primarily stochastic methods, and therefore the actual costs could be between -48% and +72% of the estimated values (AACE class 4 estimate) (Turton et al., 2018)

Table 11. Capacity, materials of construction, and cost information for plant equipment.

Compressors	Compressor Type	Power (kW)	# Spares	MOC ^(a)			Purchased Equipment Cost	Bare Module Cost	Base Bare Module Cost
K-101	Centrifugal	8024	0	SS			\$5,360,000	\$ 14,700,000	\$ 7,000,000
K-102	Centrifugal	8635	0	SS			\$5,630,000	\$ 15,400,000	\$ 7,350,000
K-103	Centrifugal	2166	0	SS			\$1,550,000	\$ 4,260,000	\$ 2,030,000
K-104	Centrifugal	867	0	SS			\$806,000	\$ 2,210,000	\$ 1,050,000
K-105	Centrifugal	746	0	SS			\$719,000	\$ 1,970,000	\$ 939,000
K-106	Centrifugal	692	0	SS			\$678,000	\$ 1,860,000	\$ 886,000
Drives	Drive Type	Power (kW)	# Spares				Purchased Equipment Cost	Bare Module Cost	Base Bare Module Cost
TU-100	Steam Turbine	23410	0				\$ 2,070,000	\$ 7,250,000	\$ 7,250,000
TU-101	Steam Turbine	18260	0				\$ 1,570,000	\$ 5,510,000	\$ 5,510,000
Electrical Generators ^(b)	Drive Type	Power (kW)	# Spares				Purchased Equipment Cost	Bare Module Cost	Base Bare Module Cost
EX-101 Generator	Electric - Explosion Proof	3170	0				\$ 443,000	\$ 665,000	\$ 665,000
TU-101 Generator	Electric - Explosion Proof	18260	0				\$ 1,970,000	\$ 2,960,000	\$ 2,960,000
Exchangers	Exchanger Type	Shell Pressure (barg)	Tube Pressure (barg)	MOC (Tube/Shell)		Area (m ²)	Purchased Equipment Cost	Bare Module Cost	Base Bare Module Cost
E-101	Fixed, Sheet, or U-Tube	18	19	Ni / Ni		709	\$ 375,000	\$ 776,000	\$ 310,000
E-102	Fixed, Sheet, or U-Tube	35	17	SS / CS		71.5	\$ 67,200	\$ 164,000	\$ 106,000
E-103	Fixed, Sheet, or U-Tube	0.7	17	SS / CS		338	\$ 114,000	\$ 289,000	\$ 202,000
E-104	Fixed, Sheet, or U-Tube	4	34	SS / CS		337	\$ 116,000	\$ 292,000	\$ 202,000
E-108	Fixed, Sheet, or U-Tube	0.4	79	SS / CS		265	\$ 106,000	\$ 264,000	\$ 179,000
E-109	Fixed, Sheet, or U-Tube	1.4	79	SS / CS		135	\$ 78,400	\$ 196,000	\$ 133,000
E-110	Fixed, Sheet, or U-Tube	77	77	SS/SS		737	\$ 345,000	\$ 730,000	\$ 318,000
E-113	Fixed, Sheet, or U-Tube	4	9	SS / CS		15.4	\$ 43,800	\$ 112,000	\$ 79,000

E-114	Fixed, Sheet, or U-Tube	4	29	SS / CS		6.8	\$ 44,000	\$ 111,000	\$ 77,200
E-115	Fixed, Sheet, or U-Tube	4	4	SS / CS		15.1	\$ 65,400	\$ 148,000	\$ 78,900
E-118	Fixed, Sheet, or U-Tube	0.4	4	CS/CS		196	\$ 47,200	\$ 155,000	\$ 155,000
E-122	Fixed, Sheet, or U-Tube	0.01	4	CS/CS		3560	\$ 109,000	\$ 1,440,000	\$ 359,000
E-111	Air Cooler		77	SS		1350	\$ 930,000	\$ 1,390,000	\$ 596,000
E-117	Air Cooler		0.24	SS		7000	\$ 2,090,000	\$ 3,220,000	\$ 1,550,000
E-112	Fixed, Sheet, or U-Tube	4	76	SS / CS		628	\$ 169,000	\$ 424,000	\$ 287,900
E-116	Fixed, Sheet, or U-Tube	4	0.2	SS/CS		127	\$ 71,300	\$ 183,000	\$ 130,000
R-101 (MSR)	Fixed, Sheet, or U-Tube	35	79	SS/CS		39700	\$ 280,000	\$ 26,200,000	\$ 386,000
Fans / Blowers	Type	Gas Flowrate (m ³ /s)	# Spares	MOC	Pressure Rise Across Fan (barg)		Purchased Equipment Cost	Bare Module Cost	Base Bare Module Cost
B-101	Centrifugal Radial	81.7	0	CS	0.16		\$ 78,000	\$ 213,000	\$ 133,000
Heater	Type	Heat Duty (MJ/h)	Steam Superheat (°C)	MOC	Pressure (barg)		Purchased Equipment Cost	Bare Module Cost	Base Bare Module Cost
Fired Heater	Pyrolysis Furnace	1030000		SS	19		\$ 23,900,000	\$ 67,900,000	\$ 50,900,000
Pump	Type	Power (kW)	# Spares		Discharge Pressure (barg)		Purchased Equipment Cost	Bare Module Cost	Base Bare Module Cost
P-101	Centrifugal	9.9	0	CS	0.7		\$ 9,340	\$ 24,000	\$ 19,500
P-102	Centrifugal	0.1	0	CS	0.7		\$ 5,820	\$ 14,900	\$ 12,200
P-102	Centrifugal	264	0	CS	40		\$ 107,000	\$ 221,000	\$ 131,000
Towers	Tower Description	Height (m)	Diameter (meters)	Tower MOC	Demister MOC	Pressure (barg)	Purchased Equipment Cost	Bare Module Cost	Base Bare Module Cost
T-101	20 SS Valve Trays	17.6	2.5	SS		1.4	\$ 659,000	\$ 1,090,000	\$ 573,000
T-102	58 SS Sieve Trays	67.7	5	SS		0.4	\$ 5,950,000	\$ 12,000,000	\$ 6,220,000

Turbines	Turbine Type	Power (kW)	# Spares	MOC			Purchased Equipment Cost	Bare Module Cost	Base Bare Module Cost
EX-101	Radial Gas Expander	3170	0	CS			\$ 903,000	\$ 3,160,000	\$ 3,160,000
Vessels	Orientation	Length/Height (m)	Diameter (m)	MOC	Demister MOC	Pressure (barg)	Purchased Equipment Cost	Bare Module Cost	Base Bare Module Cost
V-101	Vertical	8.35	3.3	SS Clad	SS	77	\$ 3,420,000	\$ 6,380,000	\$ 326,000
V-102	Vertical	6.7	2.23	SS Clad	SS	1.4	\$ 66,200	\$ 192,000	\$ 146,000
V-103 (BFW Deaerator)	Horizontal	6.85	2.28	CS		0.7	\$ 30,000	\$ 90,300	\$ 90,300
User Added Equipment	Description						Purchased Equipment Cost	Bare Module Cost	Base Bare Module Cost
E-105 & E-106	Solid Carbon HX						\$ 3,640,000	\$ 3,640,000	\$ 3,640,000
PU-100	PSA						\$ 27,800,000	\$ 27,800,000	\$ 27,800,000
Molten Metal	Cu _{0.45} Bi _{0.55}						\$ 8,145,000	\$ 8,145,000	
MSR Catalyst	MSR catalyst						\$ 7,500,000	\$ 7,500,000	
Molten Salt	NaBr						\$ 199,831	\$ 199,831	

^(a)MOC refers to material of construction. CS = carbon steel, SS = stainless steel, Ni = nickel.

^(b)Since CAPCOST does not include electrical generators, their costs are estimated as that of electrical drives of the same power.

Table 12. Breakdown of the grassroots cost of the CP-LMBR plant by equipment type.

Equipment type	Contribution to C_{GR}	Percent of C_{GR}
Compressors, blowers, and pumps	\$ 48,230,022	14.2
Expanders, turbines, and electrical generators	\$ 23,039,500	6.8
Heat exchangers	\$ 15,968,940	4.7
Fired heater + Pyrolysis reactor (PR)	\$ 89,968,901	26.5
Methanol synthesis reactor (MSR)	\$ 39,766,000	11.7
PSA	\$ 32,804,000	9.6
Flash vessels, demisters, and BFW deaerator	\$ 7,861,514	2.3
Distillation towers and trays	\$ 15,446,200	4.5
Auxiliary facilities	\$ 67,020,650	19.7
TOTAL	\$ 340,047,907	100

5.2 Estimation of Manufacturing Costs

Table 13 shows the data used for the estimation of manufacturing costs. The assumed unit prices of raw materials, methanol product, and exported electricity are justified below.

Table 13. Data for estimation of manufacturing costs.

Plant operating hours	8322 h/yr
Natural gas	\$0.1246 /kg
Captured CO ₂	\$0.073 /kg
Methanol	\$0.390 /kg
NaBr salt make-up	\$1 /kg
Methanol synthesis catalyst replacement	\$20 /kg
Electricity	\$0.0681 /kWh (\$18.92 /GJ)
Makeup boiler feed water at 25°C	\$0.333 /1000 kg
Makeup cooling water	\$0.212 /1000 kg
Operating labour	\$30.15 /h
Wastewater treatment	\$56 /1000 m ³

5.2.1 Natural Gas

The Henry Hub natural gas spot price was \$2.566/MMBtu (\$0.0024321/MJ) on average in 2019 (EIA (U.S. Energy Information Administration), n.d.-b). Since the natural gas used in this work has an HHV of 51.23 MJ/kg, its estimated price on a mass basis is $(0.0024321)(51.23) = \$0.1246/\text{kg}$.

5.2.2 Carbon Dioxide

Rubin et al (Rubin et al., 2015) found that costs of CO₂ post-combustion capture at new NGCC power plants varied between \$48 and \$111/t CO₂, with a representative value of \$74/t CO₂ in 2013 US dollars. Since the US average retail price of electricity for the industrial sector was \$0.0689/kWh in 2013 and \$0.0681 /kWh in 2019 (EIA (U.S. Energy Information Administration), n.d.-a), the representative value in 2019 US dollars is estimated to be $74 (0.0681)/(0.0689) = \$73/\text{t CO}_2$. The cost of transporting CO₂ by onshore pipelines ranged from \$1.3 to \$7.4/tCO₂/250 km in 2018 US dollars depending on pipeline capacity (Schmelz, W.J., Hochman, G., Miller, 2020). The cost of CO₂ transportation was not considered in the economic analysis to avoid adding an assumption about the distance between the CO₂ supplier and the methanol plant.

5.2.3 Methanol

The average methanol price in the US was \$0.390 /kg in 2019 (Methanex, n.d.).

5.2.4 Electricity

The average retail price of electricity for the industrial sector in the United States was \$0.0681 /kWh (\$18.92 /GJ) in 2019 (EIA (U.S. Energy Information Administration), n.d.-a).

5.2.5 Makeup NaBr Salt and Replacement of Methanol Synthesis Catalyst

The amount of makeup salt needed per hour of operation was estimated as the product of the carbon production rate (57,442 kg/h) and the mass fraction of NaBr in the washed carbon

(0.0266) (Rahimi et al., 2019). Assuming that NaBr costs \$1/kg, the corresponding cost of makeup salt is \$1528/h or \$12.72 million/y for 8322 plant operating hours per year. This represents approximately 4.7% of the revenue from methanol sales. The loss of NaBr cost could be reduced if the carbon was thermally treated after washing to recover NaBr as proposed in Pruvost et al (Pruvost et al., 2022). Nevertheless, this additional step would generate additional costs and was not considered in the present work.

The Cu/Zn/Al₂O₃ methanol synthesis catalyst has a lifetime of approximately two years for typical MSR operating conditions (220 – 300°C and 5 – 8 MPa) (Kung, 1992)(Kung, 1992). Although the catalyst is replaced once every two years, an equivalent rate of catalyst replacement can be calculated by dividing the total mass of catalyst in the MSR (375,000 kg) by the number of hours in a two-year period. This gives a catalyst replacement rate of 21.4 kg/h. For an assumed catalyst price of \$20/kg, the equivalent catalyst replacement cost is \$428/h or \$3.56 million/y.

5.2.6 Cost of Operating Labour

The number of operators per shift, N_{OL} , is estimated as follows (Turton et al., 2018):

$$N_{OL} = (6.29 + 31.7P^2 + 0.23N_{np})^{0.5} \quad (58)$$

where P is the number of particulate handling steps and N_{np} is the number of non- particulate equipment items in the process. The CP-LMBR process has 2 complex particulate steps (carbon removal from the PR and carbon washing). The calculation of N_{np} is shown in Table 14.

Table 14. Number of non-particulate equipment.

Equipment Type	Number of Equipment
Compressors	6
Exchangers	16
Heaters/Furnaces	1
Reactors	2
Towers	2
Total (N_{np})	29

Therefore, $N_{OL} = (6.29 + 31.7 \times (2)^2 + 0.23 \times (29))^{0.5} = 11.8$

The calculated value of N_{OL} is subsequently multiplied by a factor of 4.5 to find the total number of operators required to cover all the shifts. This gives a total of 53 operators on the payroll. The mean hourly wage for chemical plant and system operators in the US was \$30.15 /hr in 2019 (U.S. Bureau of Labor Statistics, n.d.). For 2080 working hours per year, this corresponds to a yearly wage of \$62,700. The cost of operating labour is therefore \$3,323,000/yr.

5.2.7 Cost of Utilities

The cost of utilities is the sum of the costs of cooling water makeup and BFW makeup, minus the revenue from exported electricity. The flow rate of cooling water makeup is 6,118 m³/d (Table 8). The cost of makeup cooling water is \$0.212 /1000 kg (Table 13), which is the sum of the costs of process water (\$0.177 /1000 kg) and chemicals for treatment (\$0.156 /1000 kg) (Turton et al., 2018). Hence, the total cost of makeup cooling water is \$449,700/yr (assuming 8322 operating hours per year).

The flow rate of BFW makeup is 79 m³/d (Table 8), and its cost is \$0.333/m³ (Table 13), which includes the costs of process water (\$0.177 /1000 kg) and chemicals for treatment (\$0.0347 /1000 kg) (Turton et al., 2018). Therefore, the cost of makeup BFW is only \$9,000/yr.

The plant exports 19.4 MW of electricity (Table 7), which is equivalent to $(0.0194 \text{ GJ/s})(3600 \text{ s/h})(8322 \text{ h/yr}) = 582,406 \text{ GJ/yr}$. Hence, the revenue from electricity sales is $(18.92 \text{ \$/GJ})(582,406 \text{ GJ/yr}) = \$11.019 \text{ million/yr}$.

Based on the above, the total cost of utilities is $0.450 + 0.009 - 11.019 = -\10.56 million/yr . The negative sign indicates that utilities account for a net revenue to the plant because of the electricity export.

5.2.8 Cost of Waste Treatment

The main waste produced by the plant is wastewater from the distillation column T-102, the blowdowns from the steam system, and the purge from the cooling water loop. The wastewater from the distillation column is the largest source of wastewater, accounting for $1160 \text{ m}^3/\text{d}$. The blowdown from the MSR reactor shell is $79 \text{ m}^3/\text{d}$ (Table 8). The purge of the cooling water system is estimated at 0.133% of the circulating cooling water flow rate (Turton et al., 2018), which corresponds to $370 \text{ m}^3/\text{d}$. Therefore, the total flow rate of wastewater is $1609 \text{ m}^3/\text{d}$. Assuming tertiary treatment (filtration, activated sludge, and chemical processing) at $\$0.056/\text{m}^3$ (Turton et al., 2018), the wastewater treatment cost is $\$3.75/\text{h}$ or $\$31,200/\text{yr}$ assuming 8322 operating hours per year.

Table 15 reports the flow rates and annual costs of the reactants (natural gas and captured CO_2), methanol, make-up salt, and methanol synthesis catalyst. The cost of carbon is not included in Table 15 because it is not an input to the economic evaluation. Instead, the sale price of carbon at which the net present value of the plant is equal to zero (defined as the levelized cost of carbon) will be determined by a discounted cash flow analysis in Section 5.3.

Table 15. Material flows and annual costs.

Material	Price (\$/kg)	Flow rate (kg/h)	Annual revenue (cost) (\$million)
Natural gas	0.1246	96,390	(99.9)
Captured CO ₂	0.073	116,582	(70.8)
Makeup NaBr salt	1	1,528	(12.7)
Methanol synthesis catalyst replacement	20	21.4	(3.6)
Methanol	0.390	83,341	270.4
Carbon	TBD ^(a)	57,417	TBD

^(a)To be determined as a levelized cost to make the net present value of the plant equal to zero.

The cost of manufacturing without depreciation, COM_d , is evaluated as a function of the fixed capital investment, FCI , the cost of labour, C_{OL} , the cost of utilities C_{UT} , the cost of waste treatment, C_{WT} , and the cost of raw materials, C_{RM} (Turton et al., 2018):

$$COM_d = 0.180 FCI + 2.76C_{OL} + 1.23(C_{UT} + C_{WT} + C_{RM}) \quad (59)$$

The numerical values of all the contributors to COM_d are given in Table 16. The FCI is equal to the grassroots cost, C_{GR} . Table 16 shows that the cost of manufacturing is mostly influenced by the cost of raw materials and the costs associated with the fixed capital investment (maintenance and repairs, operating supplies, plant overhead costs, administration costs, local taxes, and insurance) which are implicitly accounted for as 18% of FCI in Equation (59). The cost of utilities is negative because the CP-LMBR plant sells its electricity exports.

Table 16. Estimation of annual manufacturing cost by Equation (59).

FCI (Fixed capital investment = C_{GR})	\$340.1 million
C_{RM} (Cost of raw materials)	187.0 million/yr
C_{OL} (Cost of operating labour)	\$3.3 million/yr
C_{UT} (Cost of utilities)	-\$10.56 million/yr
C_{WT} (Cost of waste treatment)	0.03 million/yr
COM_d (Cost of manufacturing)	287.5 million/yr

5.3 Cash Flow Analysis

Table 17 shows the assumptions made for the cash flow analysis. The discount rate of 20% is consistent with a medium level of risk (Peters, M., Timmerhaus, K., West, 2002) since the plant uses a new process technology (natural gas pyrolysis in molten metal) to produce methanol and carbon entering established markets. This discount rate is much higher than those assumed by Narine et al (Narine et al., 2021) (7%), Pruvost et al (Pruvost et al., 2022) (8%), Riley et al (Riley et al., 2021) (8%), and Parkinson et al (Parkinson et al., 2018) (10%) for processes involving natural gas pyrolysis. The low discount rates used by these authors would be appropriate for lower risk investments and appear to be inconsistent with the technological challenges of implementing natural gas pyrolysis at industrial scale. The effect of discount rate on the cash flow analysis will be investigated in the sensitivity analysis later in this section.

Table 17. Cash flow analysis assumptions.

Discount rate	20%
Corporate tax rate ^(a)	23%
Construction period	2 years
Distribution of fixed capital investment	60% at the end of Year 1 40% at the end of Year 2
Working capital	15% of <i>FCI</i>
Cost of land	\$10 million
Project life	15 years including construction period
Depreciation	MACRS (5-year recovery period)
Plant salvage value	10% of <i>FCI</i>

^(a)The US corporate tax rate was 21% in 2019 (the base year for this study), increased to 25% in 2021, and is expected to fall to 23% in 2022. An average tax rate of 23% was chosen for the project.

The economic performance of the plant is assessed by the levelized cost of carbon (*LCOC*), which is defined as the carbon sale price required to make the net present value (*NPV*) of the project be zero. The *NPV* is the cumulative discounted cash flow at the end of the project lifetime, which is set arbitrarily to 15 years:

$$NPV = - \sum_{j=0}^{s-1} \frac{CI_j}{(1+i)^t} + \sum_{j=s}^n \frac{ATCF_j}{(1+i)^t} \quad (60)$$

Where $ATCF_j$ is the after-tax cash flow in year j , CI_j is the capital investment in year j , n is the project lifetime ($n = 15$), s is the year of start-up ($s = 3$), and i is the discount rate. Equation (60) assumes that the land is bought at year $j = 0$ and that capital investments are only done during the first $s - 1$ years of the project. The $ATCF_j$ is calculated for every year of the project after start-up as follows:

$$ATCF_j = (R - COM_d - d)(1 - t) + d \quad (61)$$

where t is the tax rate, d is the depreciation, and R is the revenue from sales of methanol and carbon. Figure 27 shows the non-discounted and discounted $ATCF$, as well as the cumulative discounted cash flow, throughout the project lifetime. The cash flow increases in the final year because the working capital, the cost of land, and the salvage value of the plant are refunded in that year. The $LCOC$ was adjusted by trial and error to make the NPV reach zero after 15 years. This resulted in a $LCOC$ of \$0.270/kg. The $LCOC$ can also be viewed as the production cost of carbon when the rate of return (RoR) on the plant investment is equal to the discount rate. By comparison, the price of carbon black for use in rubber tires, which accounts for the majority of the carbon black usage (Dagle et al., 2017a), was around \$2.6/kg in the United States in the first quarter of 2022 after having ranged from approximately \$1.4 to \$2.5/kg in 2021 (Chemanalyst, n.d.). If the carbon were sold at a price higher than the $LCOC$, then the RoR would exceed the assumed discount rate of 20%. The CP-LMBR process has therefore considerable potential for economic profitability if the produced carbon can be sold in the carbon black market.

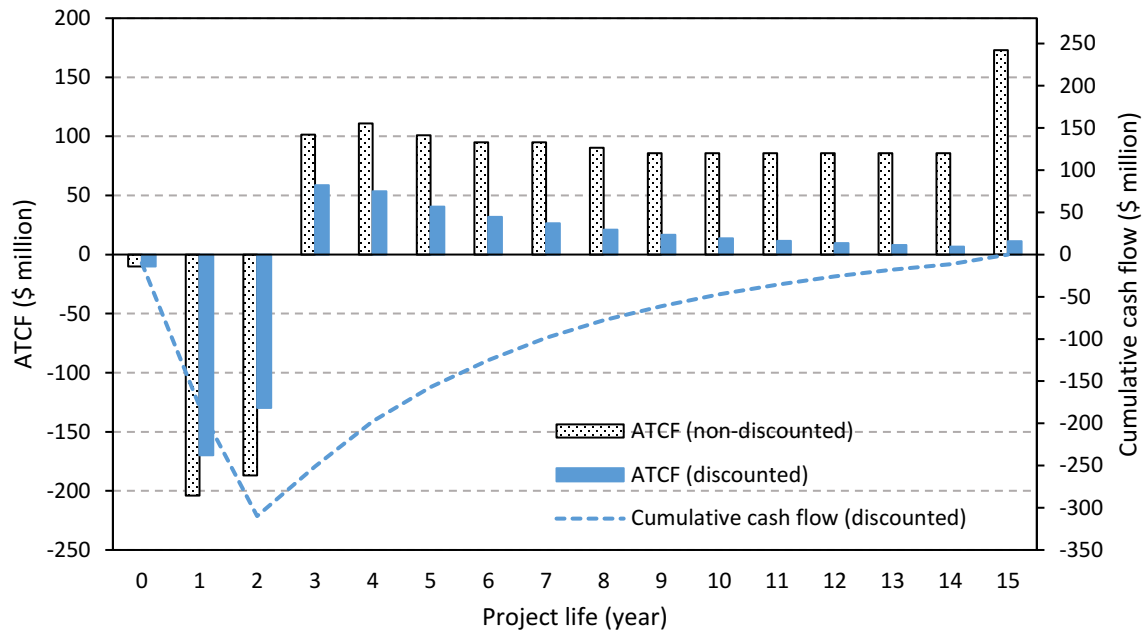


Figure 27. Discounted and non-discounted cash flow diagram when the cost of carbon is set to its levelized value of \$0.270/kg.

5.4 Levelized Cost of Carbon Sensitivity Analysis

Figure 29 shows the effects of variations in several economic parameters on the *LCOC*. The *FCI* varies between -48% and +72% of its base value found in Table 14 because capital costs were estimated by primarily stochastic methods and therefore correspond to Class 4 estimates according to the classification of Turton et al (Turton et al., 2018). The CO₂ cost varies from \$10 to \$116/t CO₂, where the low end of this range corresponds to the lowest capture costs from industrial waste streams having relatively high CO₂ concentrations (Edwards & Celia, 2018), and the high end reflects the highest capture costs from modern NGCC plants (Rubin et al., 2015), adjusted to 2019 dollars.

The yearly average market prices of natural gas and methanol have been highly correlated during the past ten years (2012 – 2021) with a coefficient of determination $R^2 = 0.76$ (Figure 28). This is not surprising as most of the industrially produced methanol is made from natural gas. Moreover, when the yearly average prices are normalized by their overall average over the 2012-2021 period, the best-fit line has a slope of unity. This means that, on average, natural gas and methanol prices increase or decrease by the same proportion. Therefore, both prices were

increased together by 45% or decreased together by 15% from their base values in Table 13 to cover the range of yearly average prices during the past ten years.

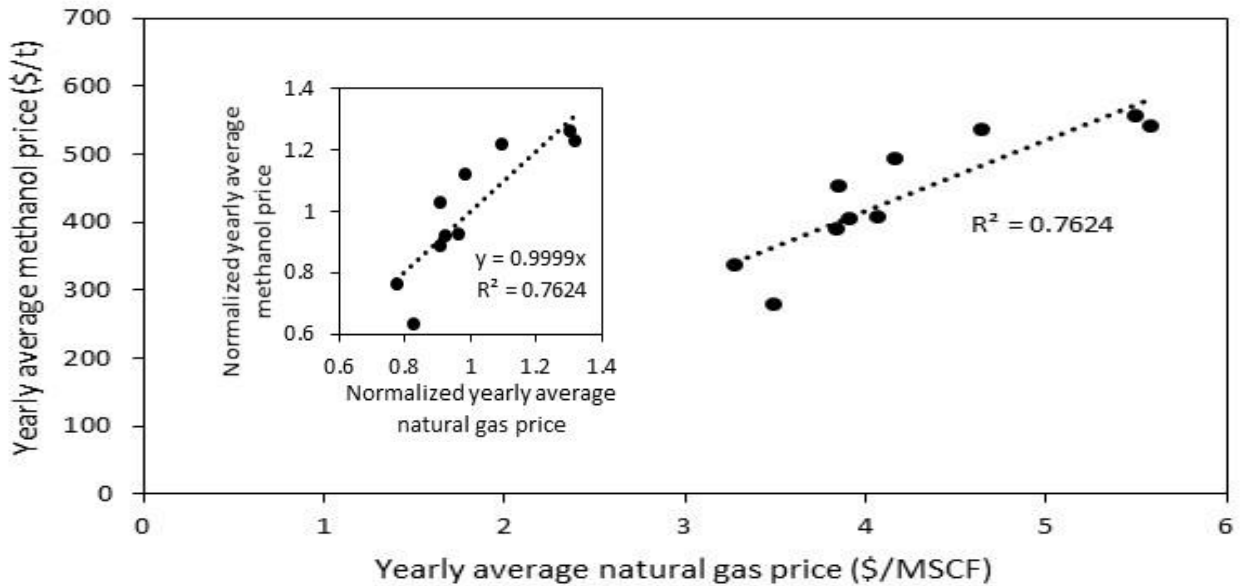


Figure 28. Correlation between yearly average methanol and industrial natural gas prices between 2012 and 2021. Historical natural gas prices are from EIA (U.S. Energy Information Administration) (EIA (U.S. Energy Information Administration), n.d.-c). Historical methanol prices are from Methanex (Methanex, n.d.). Normalized yearly average prices in the figure insert are calculated as ratios of yearly average prices to the overall average over the 2012-2021 period.

The electricity price ranges from \$0.0667 to \$0.0726 /kWh, which are to the minimum and maximum average yearly industrial prices for electricity in the United States during the past ten years (EIA (U.S. Energy Information Administration), n.d.-a). The discount rate varies between 7%, which is the lowest literature value assumed for pyrolysis processes (Narine et al., 2021), and 24%, which corresponds to the high end suggested by Peters et al (Peters, M., Timmerhaus, K., West, 2002) for a new process technology. The NaBr cost varies from the lowest estimate found on the web (\$1/kg) to \$3/kg. The tax rate varies arbitrarily from 0% to 40%, and the project life varies from 10 years to 20 years.

The parameters that most affect the *LCOC* are, in decreasing order of importance, the *FCI*, the captured CO₂ cost, the natural gas (NG) & methanol costs, and the discount rate. Figure 29 shows that the *LCOC* can decrease to values of \$0.10/kg or \$0.11/kg when the *FCI* or the CO₂ cost are at their lower bounds, respectively. Interestingly, the *LCOC* is inversely related to the costs of natural gas and methanol: an *LCOC* as low as \$0.13/kg can be achieved when the market prices of these commodities are together at their upper bounds. This is because the price differential between methanol and natural gas increases as their prices increase. By comparison, the NaBr cost, the tax rate, the project life, and the cost of electricity have low to negligible effects on the *LCOC*.

In summary, the sensitivity analysis reveals that the profitability of the plant is critically dependent on minimizing the capital cost investment and the purchase cost of CO₂. It is important to remember that the purchase cost of CO₂ depends on its source which is also directly related to the CO₂ emissions associated with CO₂ capture as was reviewed in Sections 4.3 & 5.2.2. This makes the CO₂ source one of the most important variables in the process. The plant is expected to become more profitable as the cost of natural gas increases if the correlation between methanol prices and gas prices continues to hold in the future.

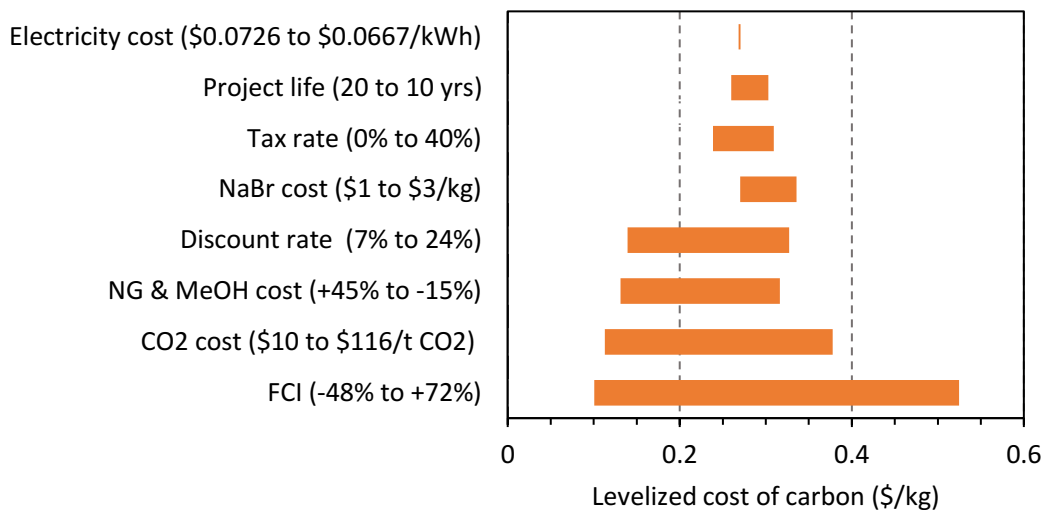


Figure 29. Sensitivity of the levelized cost of carbon to variations in economic parameters.

Chapter 6. Conclusion & Future Recommendations

This research presents the design of a novel methanol synthesis process with a capacity of 2000 t/d grade AA methanol that is based on natural gas pyrolysis where the pyrolysis reactor operating conditions and reactor design specifications are accurately modelled and incorporated into the process simulation. The total process CO₂ emissions account for the indirect emissions in the natural gas supply chain, the indirect emissions associated with CO₂ capture, the indirect emissions associated with electricity import when applicable and the direct emissions in the process flue gas.

At base operating conditions and a PR CH₄ conversion of 80%, the process cradle-to-gate and cradle-to-grave emissions are 0.074 and 1.448 t CO_{2-eq}/t MeOH, respectively. The process CO₂ emissions are most sensitive to the indirect emissions in the natural gas supply chain, the cradle-to-gate emissions range from as low as -0.340 t CO₂/t MeOH to as high as 1.961 t CO₂/t MeOH when emissions factors of 0.0036 and 0.0424 t CO_{2-eq} / GJ HHV are used, respectively. A natural gas supply chain emissions factor of 0.0424 t CO_{2-eq} / GJ HHV is the only instance where the processes designed in this work does not outperform all other reviewed methanol production processes. The developed process is less sensitive to the CO₂ emissions associated with CO₂ capture (cradle-to-gate emissions are -0.121 t CO_{2-eq}/t MeOH at the low end and 0.439 t CO_{2-eq}/t MeOH at the high end). The process is insensitive to the CO₂ emissions associated with electricity import as the required electricity is produced in house. The proposed process outperforms the pyrolysis-based NCTD & NCTD + CC process at all emissions factors for all indirect emissions sources.

The LCOC is determined to be \$270/t at base operating conditions and is most sensitive to the FCI of the plant, reaching a maximum of \$525/t when the FCI increased by 72% and reaching its minimum of \$101/t when the FCI is decreased by 48%. The CO₂ cost, natural gas & methanol costs and discount rate all effect the LCOC, with the CO₂ cost having the larges effect, but to a lesser extent than the FCI. The lowest LCOC (\$113/t) for these parameters occurs at a CO₂ cost of \$10/t and the highest (\$378/t) occurs at a CO₂ cost of \$116/t. By pairing this effect with the knowledge that the purchase price of CO₂ as well as the emissions associated with its capture

are both related to the CO₂ source, it can be concluded that the CO₂ source is one of the most important variables for both the process performance and economics. The LCOC is relatively insensitive to the cost of NaBr, tax rate, project life and electricity cost.

The process designed in this research offers an alternative methanol production route that emits less CO₂ than traditional pathways largely based on the fact that it utilizes CO₂ as a raw material. The process is economically viable as the LCOC is much lower than the US market price of carbon black for use in rubber tires, which accounts for the majority of carbon black usage. However, it remains to be seen whether or not the solid carbon produced by natural gas pyrolysis in CLMBR is of suitable quality and purity for application in this field.

Future research in this field should be focused on the product solid carbon as it is the key economic variable of the process. Lab scale experiments should be performed to determine the carbon quality and purity that is produced from a 45 mol% Cu – 55 mol% Bi CLMBR with an NaBr salt cap. Part of these experiments should include investigation of the effectiveness of the proposed carbon cleaning methods in order to determine the best method for achieving the highest purity carbon product to ensure its sale in the carbon black market which requires a minimum 95 wt% carbon purity. Additionally, some cleaning methods may be accompanied by energy requirements, such as vacuum heating at 1000 °C for 12 hours, which may or may not result in further CO₂ emissions. As well, while the reaction mechanism for carbon production in fluidized bed methane pyrolysis reactors has been investigated, no such research has been performed on the mechanism for pyrolysis in CLMBRs. The possible interaction between hydrogen and carbon could defeat the purpose of hydrogen production by methane pyrolysis in CLMBRs depending on its extent.

In addition, there are some key assumptions that have been made in this research that could be improved upon by future work. One such assumption is that the PR is isothermal. Modelling the heat transfer in the PR would aid in validating the proposed reactor heating method (inside a fired heater) and configuration (tube bundles stacked on top of each other). Another assumption is that the hydrogen separated in the PSA is 100% pure. In reality it is likely that some nitrogen would be separated with the product hydrogen, resulting in an increased flow

rate and larger equipment sizes downstream of the PSA. The presence of nitrogen could also effect the purge rate from the MSR loop, as it is a non-reactive species and needs to be purged in order to prevent its accumulation.

References

- 95% Purity Carbon Black, For Rubber, Powder, Rs 90/kg S. M. Associates | ID: 25619457855. (n.d.). Retrieved June 17, 2022, from <https://www.indiamart.com/proddetail/95-purity-carbon-black-25619457855.html>
- 99.9% Purity Fine Graphite Powder For Lubricant Graphite Price Ton Carbon Graphite Carbon - Buy Carbon Graphite Carbon, Fine Graphite Powder For Lubricant, 99.9% Purity Nano Graphite Powder Price Fine Graphite Powder For Lubricant Product on Alibaba.com. (n.d.). Retrieved May 19, 2022, from https://www.alibaba.com/product-detail/99-9-purity-fine-graphite-powder_1600450647336.html?spm=a2700.7724857.normal_offer.d_title.21dc4f9ezT4ekn
- Abánades, A., Ruiz, E., Ferruelo, E. M., Hernández, F., Cabanillas, A., Martínez-Val, J. M., Rubio, J. A., López, C., Gavela, R., Barrera, G., Rubbia, C., Salmieri, D., Rodilla, E., & Gutiérrez, D. (2011). Experimental analysis of direct thermal methane cracking. *International Journal of Hydrogen Energy*, 36(20), 12877–12886. <https://doi.org/10.1016/J.IJHYDENE.2011.07.081>
- Acquarola, C., Ao, M., Bhatelia, T., Prakash, B., Faka, S., Pareek, V., & Shah, M. T. (2021). *Simulations and Optimization of a Reduced CO₂ Emission Process for Methanol Production Using Syngas from Bi-reforming*. 3. <https://doi.org/10.1021/acs.energyfuels.1c00227>
- Akita, K., & Yoshida, F. (1974). Bubble Size, Interfacial Area, and Liquid-Phase Mass Transfer Coefficient in Bubble Columns. *Industrial and Engineering Chemistry Process Design and Development*, 13(1), 84–91. <https://doi.org/10.1021/i260049a016>
- American Petroleum Institute. (2016). *Fired Heaters for General Refinery Service, API Standard 560*.
- applications-and-benefits-of-multi-walled-carbon*. (n.d.). Retrieved June 22, 2022, from <https://www.nanoshel.com/applications-and-benefits-of-multi-walled-carbon/>
- Assen, N. Von Der, Müller, L. J., Steingrube, A., Voll, P., & Bardow, A. (2016). Selecting CO₂ Sources for CO₂ Utilization by Environmental-Merit-Order Curves. *Environmental Science and Technology*, 50(3), 1093–1101. <https://doi.org/10.1021/acs.est.5b03474>
- Azzaro, G., Collodi, G., & Ferrari, N. (2017). *Techno-Economic Evaluation of HYCO Plant Integrated to Ammonia / Urea or Methanol Production with CCS, 2017/03. February*.
- Balcombe, P., Brandon, N. P., & Hawkes, A. D. (2018). Characterising the distribution of methane and carbon dioxide emissions from the natural gas supply chain. *Journal of Cleaner Production*, 172, 2019–2032. <https://doi.org/10.1016/j.jclepro.2017.11.223>
- Balcombe, Paul, Anderson, K., Speirs, J., Brandon, N., & Hawkes, A. (2017). The Natural Gas Supply Chain: The Importance of Methane and Carbon Dioxide Emissions. *ACS Sustainable Chemistry and Engineering*, 5(1), 3–20. <https://doi.org/10.1021/acssuschemeng.6b00144>
- Bell, D. A., & Towler, B. F. (2010). *Coal gasification and its applications*. William Andrew.

- Benzinger, W., Becker, A., & Hüttinger, K. J. (1996). Chemistry and kinetics of chemical vapour deposition of pyrocarbon: I. Fundamentals of kinetics and chemical reaction engineering. *Carbon*, 34(8), 957–966. [https://doi.org/10.1016/0008-6223\(96\)00010-3](https://doi.org/10.1016/0008-6223(96)00010-3)
- Bismuth Price*. (n.d.). Retrieved November 24, 2021, from <http://strategic-metal.com/products/bismuth/bismuth-price/>
- Bode, A., & Flick, D. (2021). *BASF Strategy : We create chemistry*.
- Bokobza, L., Bruneel, J.-L., & Couzi, M. (2015). Raman Spectra of Carbon-Based Materials (from Graphite to Carbon Black) and of Some Silicone Composites. *C*, 1(1), 77–94. <https://doi.org/10.3390/c1010077>
- CAPCOST 2017*. (n.d.).
- Carbon and Graphite - Global Market Trajectory & Analytics*. (n.d.). Retrieved May 18, 2022, from [https://www.researchandmarkets.com/reports/338573/carbon_and_graphite_global_market_trajectory?utm_source=BW&utm_medium=PressRelease&utm_code=s4sm8z&utm_campaign=1614688+-+Global+Carbon+and+Graphite+Market+\(2020+to+2027\)+-+Asia-Pacific+Continues+to+Dominate+Consumption&utm_exec=jamu273prd](https://www.researchandmarkets.com/reports/338573/carbon_and_graphite_global_market_trajectory?utm_source=BW&utm_medium=PressRelease&utm_code=s4sm8z&utm_campaign=1614688+-+Global+Carbon+and+Graphite+Market+(2020+to+2027)+-+Asia-Pacific+Continues+to+Dominate+Consumption&utm_exec=jamu273prd)
- Carbon Black - Himadri*. (n.d.). Retrieved June 15, 2022, from https://www.himadri.com/carbon_black
- Carbon Black Market Size, Share | Industry Growth & Forecast, 2026*. (n.d.). Retrieved June 15, 2022, from <https://www.alliedmarketresearch.com/carbon-black-market>
- Carbon Black Prices, News, Market & Analysis | ChemAnalyst*. (n.d.). Retrieved June 15, 2022, from <https://www.chemanalyst.com/Pricing-data/carbon-black-42>
- Catalan, L. J. J., & Rezaei, E. (2020). Coupled hydrodynamic and kinetic model of liquid metal bubble reactor for hydrogen production by noncatalytic thermal decomposition of methane. *International Journal of Hydrogen Energy*, 45(4), 2486–2503. <https://doi.org/10.1016/j.ijhydene.2019.11.143>
- Catalan, L. J. J., & Rezaei, E. (2022). Modelling the hydrodynamics and kinetics of methane decomposition in catalytic liquid metal bubble reactors for hydrogen production. *International Journal of Hydrogen Energy*, xxxx. <https://doi.org/10.1016/j.ijhydene.2021.12.089>
- Chemanalyst. (n.d.). *Carbon Black Price Trend and Forecast*.
- China Factory Expanded Graphite 99% Carbon Expanded Graphite Powder Price - Buy Expanded Graphite, Expanded Graphite Powder, High Carbon Graphite Powder For Sale Product on Alibaba.com*. (n.d.). Retrieved May 19, 2022, from https://www.alibaba.com/product-detail/China-factory-expanded-graphite-99-carbon_62300174650.html?spm=a2700.7724857.normal_offer.d_title.21dc4f9ezT4ekn
- Collodi, G., Azzaro, G., Ferrari, N., & Santos, S. (2017). Demonstrating Large Scale Industrial CCS

- through CCU - A Case Study for Methanol Production. *Energy Procedia*, 114(November 2016), 122–138. <https://doi.org/10.1016/j.egypro.2017.03.1155>
- Cooling Heat Exchanger - Cool Bulk Solids Without Air | Solex - Solex*. (n.d.). Retrieved September 15, 2021, from <https://www.solexthermal.com/our-technology/cooling>
- Copper Prices - 45 Year Historical Chart*. (n.d.).
- Couper, J.R., Penney, W.R., Fair, J.R., Walas, S. M. (2012). *Chemical Process Equipment: Selection and Design* (3rd ed.). Butterworth-Heinemann.
- Dagle, R., Dagle, V., Bearden, M., Holladay, J., Krause, T., & Ahmed, S. (2017a). *An Overview of Natural Gas Conversion Technologies for Co-Production of Hydrogen and Value-Added Solid Carbon Products*. Pacific Northwest National Laboratory (PNNL-26726), Argonne National Laboratory (ANL-17/11).
- Dagle, R., Dagle, V., Bearden, M., Holladay, J., Krause, T., & Ahmed, S. (2017b). *R&D opportunities for development of natural gas conversion technologies for co-production of hydrogen and value-added solid carbon products*. <https://www.congress.gov/114/crpt/srpt236/CRPT-114srpt236.pdf>. 65. <https://www.congress.gov/114/crpt/srpt236/CRPT-114srpt236.pdf>, p.
- Data Explorer | US EPA*. (n.d.). Retrieved May 19, 2022, from <https://www.epa.gov/egrid/data-explorer>
- Dennison, J., Holtz, M., & Swain, G. (1996). *Raman Spectroscopy of Carbon Materials*. 11(8), 38–45.
- Edwards, R. W. J., & Celia, M. A. (2018). Infrastructure to enable deployment of carbon capture, utilization, and storage in the United States. *Proceedings of the National Academy of Sciences of the United States of America*, 115(38), E8815–E8824. <https://doi.org/10.1073/pnas.1806504115>
- EIA (U.S. Energy Information Administration). (n.d.-a). *Average retail price of electricity, United States*.
- EIA (U.S. Energy Information Administration). (n.d.-b). *Henry Hub Natural Gas Spot Price*.
- EIA (U.S. Energy Information Administration). (n.d.-c). *United States Natural Gas Industrial Price*.
- EPA (U.S. Environmental Protection Agency). (n.d.). *eGRID Data Explorer*.
- EPA (United States Environmental Protection Agency). (n.d.). *Greenhouse Gases Equivalencies Calculator - Calculations and References*.
- Farmer, T. C., McFarland, E. W., & Doherty, M. F. (2019). Membrane bubble column reactor model for the production of hydrogen by methane pyrolysis. *International Journal of Hydrogen Energy*, 44(29), 14721–14731. <https://doi.org/10.1016/j.ijhydene.2019.03.023>
- Fau, G., Gascoin, N., & Steelant, J. (2014). Hydrocarbon pyrolysis with a methane focus: A

- review on the catalytic effect and the coke production. *Journal of Analytical and Applied Pyrolysis*, 108, 1–11. <https://doi.org/10.1016/j.jaap.2014.05.022>
- Fulcheri, L., Probst, N., Flamant, G., Fabry, F., Grivei, E., & Bourrat, X. (2002). Plasma processing: A step towards the production of new grades of carbon black. *Carbon*, 40(2), 169–176. [https://doi.org/10.1016/S0008-6223\(01\)00169-5](https://doi.org/10.1016/S0008-6223(01)00169-5)
- Geißler, T., Abánades, A., Heinzl, A., Mehravaran, K., Müller, G., Rathnam, R. K., & Rubbia, C. (2016). *Hydrogen production via methane pyrolysis in a liquid metal bubble column reactor with a packed bed*. 299, 192–200. <https://doi.org/10.1016/j.cej.2016.04.066>
- Global Carbon Nanotubes (CNT) Market by Type (Single Walled & Multi Walled), End-Use Industry (Electronics & Semiconductors, Chemical Materials & Polymers, Structural Composites, Energy & Storage, Medical), Method, and Region - Forecast to 2026*. (n.d.). Retrieved June 22, 2022, from https://www.researchandmarkets.com/reports/5328286/global-carbon-nanotubes-cnt-market-by-type?msclkid=2644935f667f143dac62f1ec404307f1&utm_source=bing&utm_medium=cpc&utm_campaign=RLSA_DSA Telecommunications and Computing&utm_term=Carbon Nanotube&utm_content=Carbon Nanotube
- Gonzalez-Diaz, A., Jiang, L., Roskilly, A. P., & Smallbone, A. J. (2020). The potential of decarbonising rice and wheat by incorporating carbon capture, utilisation and storage into fertiliser production. *Green Chemistry*, 22(3), 882–894. <https://doi.org/10.1039/C9GC03746B>
- Greenhouse Gases Equivalencies Calculator - Calculations and References | Energy and the Environment | US EPA*. (n.d.). Retrieved March 8, 2021, from <https://www.epa.gov/energy/greenhouse-gases-equivalencies-calculator-calculations-and-references>
- Guéret, C., Billaud, F., Fixari, B., & Le Perchec, P. (1995). Thermal coupling of methane, experimental investigations on coke deposits. *Carbon*, 33(2), 159–170. [https://doi.org/10.1016/0008-6223\(94\)00120-0](https://doi.org/10.1016/0008-6223(94)00120-0)
- Guernsey, M., Chung, G., & Goetzler, W. (2015). *Pump and Fan Technology Characterization and R & D Assessment*.
- Hamelink, C., Bunse, M. (2022). *Carbon Footprint of Methanol*.
- Hibiki, T., Saito, Y., Mishima, K., Tobita, Y., Konishi, K., & Matsubayashi, M. (2000). Study on flow characteristics in gas-molten metal mixture pool. *Nuclear Engineering and Design*, 196(2), 233–245. [https://doi.org/10.1016/S0029-5493\(99\)00293-9](https://doi.org/10.1016/S0029-5493(99)00293-9)
- High Pure High Carbon 300 Mash Artificial Nano Graphite Powder Price - Buy High Pure Graphite Powder, Graphite Granules, Amorphous Graphite Powder Product on Alibaba.com*. (n.d.). Retrieved May 19, 2022, from <https://www.alibaba.com/product-detail/High-Pure-High-Carbon-300->

mash_1600144687955.html?spm=a2700.7724857.normal_offer.d_title.21dc4f9ezT4ekn

High Quality Factory Price Graphite Powder Carbon - Buy Graphite Powder Carbon, Graphite Powder Malaysia, Nickel Graphite Powder Product on Alibaba.com. (n.d.). Retrieved May 19, 2022, from https://www.alibaba.com/product-detail/High-quality-factory-price-graphite-powder_1600233206658.html?spm=a2700.7724857.normal_offer.d_title.21dc4f9ezT4ekn

IEA, Levelised cost of CO₂ capture by sector and initial CO₂ concentration, 2019, IEA, Paris. (n.d.). Retrieved May 24, 2022, from <https://www.iea.org/data-and-statistics/charts/levelised-cost-of-co2-capture-by-sector-and-initial-co2-concentration-2019>

IEAGHG. (2017). Techno-Economic Evaluation of HYCO Plant Integrated to Ammonia / Urea or Methanol Production with CCS (Issue February).

Industrial Grade 95% Purity Powder Carbon Black N660 Price For Tyre - Buy Tyre Carbon Black, Pigment Carbon Black, Carbon Black For Tyre Product on Alibaba.com. (n.d.). Retrieved June 17, 2022, from https://www.alibaba.com/product-detail/Industrial-Grade-95-Purity-Powder-Carbon_60749683272.html

Industry Grade 95% Purity Carbon Black N220 N330 For Tire Manufacturer Supplier - Buy Carbon Black Supplier, Carbon Black N330, Carbon Black N220 N330 For Tire Product on Alibaba.com. (n.d.). Retrieved June 17, 2022, from https://www.alibaba.com/product-detail/Industry-grade-95-purity-carbon-black_1600469369804.html

Ingham, A. (2017). Reducing the carbon intensity of methanol for use as a transport fuel. *Johnson Matthey Technology Review*, 61(4), 297–307. <https://doi.org/10.1595/205651317X696216>

International Renewable Energy Agency (IRENA). (2021). *Innovation Outlook: Renewable Methanol*. <http://www.irena.org/>

Kajaste, R., Hurme, M., & Oinas, P. (2018). Methanol-Managing greenhouse gas emissions in the production chain by optimizing the resource base. *AIMS Energy*, 6(6), 1074–1102. <https://doi.org/10.3934/ENERGY.2018.6.1074>

Kamali, A. R., & Fray, D. J. (2013). Molten salt corrosion of graphite as a possible way to make carbon nanostructures. *Carbon*, 56, 121–131. <https://doi.org/10.1016/J.CARBON.2012.12.076>

Kataoka, I., & Ishii, M. (1987). Drift flux model for large diameter pipe and new correlation for pool void fraction. *International Journal of Heat and Mass Transfer*, 30(9), 1927–1939. [https://doi.org/10.1016/0017-9310\(87\)90251-1](https://doi.org/10.1016/0017-9310(87)90251-1)

Kim, K. S., Seo, J. H., Nam, J. S., Ju, W. T., & Hong, S. H. (2005). Production of hydrogen and carbon black by methane decomposition using DC-RF hybrid thermal plasmas. *IEEE Transactions on Plasma Science*, 33(2 II), 813–823. <https://doi.org/10.1109/TPS.2005.844526>

- Kojima, Y., Kawai, Y., Koiwai, A., Suzuki, N., Haga, T., Hioki, T., & Tange, K. (2006). Hydrogen adsorption and desorption by carbon materials. *Journal of Alloys and Compounds*, 421(1–2), 204–208. <https://doi.org/10.1016/j.jallcom.2005.09.077>
- Kung, H. H. (1992). Deactivation of methanol synthesis catalyst - A review. *Catalysis Today*, 11, 443–453.
- Longmier, B. W., Gallimore, A. D., & Hershkowitz, N. (2012). Hydrogen production from methane using an RF plasma source in total nonambipolar flow. *Plasma Sources Science and Technology*, 21(1). <https://doi.org/10.1088/0963-0252/21/1/015007>
- Luberti, M. (2015). *Design of a H2 pressure swing adsorption process at an advanced IGCC plant for cogenerating hydrogen and power with CO2 capture*. 256. <https://www.era.lib.ed.ac.uk/handle/1842/19577>
- Lucas, P., & Marchand, A. (1990). Pyrolytic carbon deposition from methane: An analytical approach to the chemical process. *Carbon*, 28(1), 207–219. [https://doi.org/10.1016/0008-6223\(90\)90115-F](https://doi.org/10.1016/0008-6223(90)90115-F)
- Manaurite XMR - Heat resistant alloys for hydrocarbon processing*. (2012). Manoir Petrochem & Nuclear Business Unit.
- Methanex. (n.d.). *Historical Methanex Posted Price*.
- MK-121 | Catalysts | Products | Haldor Topsoe*. (n.d.). Retrieved April 7, 2022, from <https://www.topsoe.com/our-resources/knowledge/our-products/catalysts/mk-121>
- Monolith*. (n.d.). Retrieved June 30, 2022, from <https://monolith-corp.com/methane-pyrolysis>
- Monolith Carbon Black*. (n.d.). Retrieved June 30, 2022, from <https://monolith-carbonblack.com/methane-pyrolysis>
- Morgan, K. C. (2019). *CO2 Pipelines New Technologies & Economics for Carbon Capture / Sequestration*.
- Multi Walled Carbon Nanotubes Products*. (n.d.). Retrieved June 22, 2022, from <https://www.cheaptubes.com/product-category/multi-walled-carbon-nanotubes/>
- Muradov, N., Smith, F., Bockerman, G., & Scammon, K. (2009). Thermocatalytic decomposition of natural gas over plasma-generated carbon aerosols for sustainable production of hydrogen and carbon. *Applied Catalysis A: General*, 365(2), 292–300. <https://doi.org/10.1016/j.apcata.2009.06.031>
- Muradov, N., Smith, F., & T-raissi, A. (2005). *Catalytic activity of carbons for methane decomposition reaction*. 103, 225–233. <https://doi.org/10.1016/j.cattod.2005.02.018>
- Narine, K., Mahabir, J., Koylass, N., Samaroo, N., Singh-Gryzbon, S., Baboolal, A., Guo, M., & Ward, K. (2021). Climate smart process design for current and future methanol production. *Journal of CO2 Utilization*, 44(December 2020), 101399. <https://doi.org/10.1016/j.jcou.2020.101399>

- Palmer, C., Tarazkar, M., Gordon, M. J., Metiu, H., & McFarland, E. W. (2021). *Methane pyrolysis in low-cost, alkali-halide molten salts at high temperatures †*. <https://doi.org/10.1039/d1se01408k>
- Palmer, C., Tarazkar, M., Kristoffersen, H. H., Gelinas, J., Gordon, M. J., McFarland, E. W., & Metiu, H. (2019). Methane Pyrolysis with a Molten Cu-Bi Alloy Catalyst. *ACS Catalysis*, *9*(9), 8337–8345. <https://doi.org/10.1021/acscatal.9b01833>
- Palmer, H. B., & Cullis, C. F. (1965). *Chemistry and Physics of Carbon Vol.1* (p. 265). Marcel Dekker.
- Panella, B., Hirscher, M., & Roth, S. (2005). Hydrogen adsorption in different carbon nanostructures. *Carbon*, *43*(10), 2209–2214. <https://doi.org/10.1016/j.carbon.2005.03.037>
- Parkinson, B., Patzschke, C. F., Nikolis, D., Raman, S., Dankworth, D. C., & Hellgardt, K. (2021). Methane pyrolysis in monovalent alkali halide salts: Kinetics and pyrolytic carbon properties. *International Journal of Hydrogen Energy*, *46*(9), 6225–6238. <https://doi.org/10.1016/j.ijhydene.2020.11.150>
- Parkinson, B., Tabatabaei, M., Upham, D. C., Ballinger, B., Greig, C., Smart, S., & McFarland, E. (2018). Hydrogen production using methane: Techno-economics of decarbonizing fuels and chemicals. *International Journal of Hydrogen Energy*, *43*(5), 2540–2555. <https://doi.org/10.1016/j.ijhydene.2017.12.081>
- Peters, M., Timmerhaus, K., West, R. (2002). *Plant Design and Economics for Chemical Engineers* (5th Editio). McGraw Hill.
- Peters, P. E., Schifano, R. S., & Harriott, P. (1988a). *Heat Transfer in Packed-Tube Reactors*. 1978, 226–233.
- Peters, P. E., Schifano, R. S., & Harriott, P. (1988b). Heat Transfer in Packed-Tube Reactors. *Industrial and Engineering Chemistry Research*, *27*(2), 226–233. <https://doi.org/10.1021/ie00074a003>
- Pimenta, M. A., Dresselhaus, G., Dresselhaus, M. S., Cançado, L. G., Jorio, A., & Saito, R. (2007). Studying disorder in graphite-based systems by Raman spectroscopy. *Physical Chemistry Chemical Physics*, *9*(11), 1276–1290. <https://doi.org/10.1039/B613962K>
- Pruvost, F., Cloete, S., Hendrik Cloete, J., Dhoke, C., & Zaabout, A. (2022). Techno-Economic assessment of natural gas pyrolysis in molten salts. *Energy Conversion and Management*, *253*, 115187. <https://doi.org/10.1016/j.enconman.2021.115187>
- Rahimi, N., Kang, D., Gelinas, J., Menon, A., Gordon, M. J., Metiu, H., & McFarland, E. W. (2019). Solid carbon production and recovery from high temperature methane pyrolysis in bubble columns containing molten metals and molten salts. *Carbon*, *151*, 181–191. <https://doi.org/10.1016/j.carbon.2019.05.041>
- Rahmatmand, B., Rahimpour, M. R., & Keshavarz, P. (2018). Development of two novel processes for hydrogenation of CO₂ to methanol over Cu/ZnO/Al₂O₃ catalyst to improve

- the performance of conventional dual type methanol synthesis reactor. *Catalysts*, 8(7).
<https://doi.org/10.3390/catal8070255>
- Riley, J., Atallah, C., Siriwardane, R., & Stevens, R. (2021). Technoeconomic analysis for hydrogen and carbon Co-Production via catalytic pyrolysis of methane. *International Journal of Hydrogen Energy*, 46(39), 20338–20358.
<https://doi.org/10.1016/j.ijhydene.2021.03.151>
- Robertson, J. (1986). Advances in Physics Amorphous carbon. *Advances in Physics*, 35(4), 37–41.
- Rubin, E. S., Davison, J. E., & Herzog, H. J. (2015). International Journal of Greenhouse Gas Control The cost of CO₂ capture and storage. *International Journal of Greenhouse Gas Control*, 40, 378–400. <https://doi.org/10.1016/j.ijggc.2015.05.018>
- Schmelz, W.J., Hochman, G., Miller, K. G. (2020). Total cost of carbon capture and storage implemented at regional scale: northeastern and midwestern United States. *Interface Focus*, 10, 1–15.
- Schwob, Y., Fischer, F., Fulcheri, L., & Willemez, P. (2000). *Conversion of Carbon or Carbon-Containing Compounds In a Plasma* (Patent No. 6099696).
- Seader, J.D., Henley, E.J., Roper, D. K. (2016). *Separation Process Principles: With Applications Using Process Simulators* (4th ed.). Wiley.
- Senchenko, V. N., & Belikov, R. S. (2017). Experimental investigation of linear thermal expansion of pyrolytic graphite at high temperatures. *Journal of Physics: Conference Series*, 891(1), 012338. <https://doi.org/10.1088/1742-6596/891/1/012338>
- Serban, M., Lewis, M. A., Marshall, C. L., & Doctor, R. D. (2003). Hydrogen production by direct contact pyrolysis of natural gas. *Energy and Fuels*, 17(3), 705–713.
<https://doi.org/10.1021/ef020271q>
- Sjostrom, S., Denney, J., Morris, W. (2016). *Optimizing the Costs of Solid Sorbent-Based CO₂ Capture Process Through Heat Integration*.
<https://doi.org/10.2172/1337015>
- Smith, R. (2016). Chemical Process Design and Integration. In *Journal of Chemical Information and Modeling* (Vol. 53, Issue 9).
- Steinberg, M. (1997a). Methanol as an agent for CO₂ mitigation. *Energy Conversion and Management*, 38(Supplement), 423–430. [https://doi.org/10.1016/S0196-8904\(96\)00305-6](https://doi.org/10.1016/S0196-8904(96)00305-6)
- Steinberg, M. (1997b). The Carnol process system for CO₂ mitigation and methanol production. *Energy*, 22(2/3), 143–149. [https://doi.org/10.1016/S0360-5442\(96\)00138-7](https://doi.org/10.1016/S0360-5442(96)00138-7)
- Steinberg, Meyer. (1995). *The Carnol process for CO₂ mitigation from power plants and the transportation sector*. Brookhaven National Laboratory, BNL-62039.
[https://doi.org/10.1016/0196-8904\(95\)00266-9](https://doi.org/10.1016/0196-8904(95)00266-9)

- Steinberg, Meyer. (1996a). The Carnol process for CO₂ mitigation from power plants and the transportation sector. *Energy Conversion and Management*, 37(6–8), 843–848. [https://doi.org/10.1016/0196-8904\(95\)00266-9](https://doi.org/10.1016/0196-8904(95)00266-9)
- Steinberg, Meyer. (1996b). The Carnol process for CO₂ mitigation from power plants and the transportation sector. *Energy Conversion and Management*, 37(6–8), 843–848. [https://doi.org/10.1016/0196-8904\(95\)00266-9](https://doi.org/10.1016/0196-8904(95)00266-9)
- Ströbel, R., Jörissen, L., Schliermann, T., Trapp, V., Schütz, W., Bohmhammel, K., Wolf, G., & Garche, J. (1999). Hydrogen adsorption on carbon materials. *Journal of Power Sources*, 84(2), 221–224. [https://doi.org/10.1016/S0378-7753\(99\)00320-1](https://doi.org/10.1016/S0378-7753(99)00320-1)
- Tamor, M. A., & Vassell, W. C. (1994). Raman “fingerprinting” of amorphous carbon films. *Journal of Applied Physics*, 76(6), 3823–3830. <https://doi.org/10.1063/1.357385>
- The Transportation of Natural Gas* NaturalGas.org. (n.d.). Retrieved August 11, 2021, from <http://naturalgas.org/naturalgas/transport/>
- Topsoe. (n.d.). *MK-121 Methanol Synthesis Catalyst*.
- Tuinstra, F., & Koenig, J. L. (1970). Characterization of Graphite Fiber Surfaces with Raman Spectroscopy: <Http://Dx.Doi.Org/10.1177/002199837000400405>, 4(4), 492–499. <https://doi.org/10.1177/002199837000400405>
- Turton, R., Shaeiwitz, J. A., Bhattacharyya, D., & Whiting, W. B. (2018). *Analysis, synthesis, and design of chemical processes* (5th ed.). Prentice Hall.
- U.S. Breau of labor Statistics. (n.d.). *Occupational Employment and Wages, May 2019 51-8091 Chemical Plant and System Operators*.
- Upham, D. C., Agarwal, V., Khechfe, A., Snodgrass, Z. R., Gordon, M. J., Metiu, H., & McFarland, E. W. (2017). Catalytic molten metals for the direct conversion of methane to hydrogen and separable carbon. *Science*, 358(6365), 917–921. <https://doi.org/10.1126/science.aao5023>
- Vanden Bussche, K. M., & Froment, G. F. (1996). *A Steady-State Kinetic Model for Methanol Synthesis and the Water Gas Shift Reaction on a Commercial Cu / ZnO / Al₂O₃ Catalyst*. 10(0156), 1–10.
- Vinokurov, V. A., Sharafutdinov, R. G., & Tychkov, Y. I. (2005). Plasmochemical processing of natural gas. *Khimiya i Tekhnologiya Topliv i Masel*, 41(2), 25–26.
- Von Wald, G. A., Masnadi, M. S., Upham, D. C., & Brandt, A. R. (2020). Optimization-based technoeconomic analysis of molten-media methane pyrolysis for reducing industrial sector CO₂emissions. *Sustainable Energy and Fuels*, 4(9), 4598–4613. <https://doi.org/10.1039/d0se00427h>
- Walas, S. M. (1990). Heuristics in Chemical Engineering. *Chemical Process Equipment Selection and Design*.

Zaghloul, N., Kodama, S., & Sekiguchi, H. (2021). Hydrogen Production by Methane Pyrolysis in a Molten-Metal Bubble Column. *Chemical Engineering & Technology*, 44(11), 1986–1993.
<https://doi.org/10.1002/CEAT.202100210>